

Optimal Control of Reaction Wheels Disturbance Transients

by

Edoardo Coccì

to obtain the degree of Master of Science in Space Systems Engineering
at the Delft University of Technology,
to be defended publicly on Friday October 7th, 2016 at 09:30 AM.



Student number:	4418328
Project duration:	February 1, 2016 – August 31, 2016
Partner Company:	Airbus Defence and Space GmbH 88090 Immenstaad
University supervisor:	Dr. J. Guo, TU Delft
Company supervisors:	Ir. T. Ott, Airbus Defence and Space - TSOTO31 Ir. M. Vitelli, Airbus Defence and Space - TSOTO31
Thesis committee:	Prof. Dr. E.K.A. (Eberhard) Gill, TU Delft Space System Engineering Chairholder Dr. J. Guo, TU Delft department of Space Systems Engineering Dr. Q. P. Chu, TU Delft department of Control and Simulations

An electronic version of this thesis is available at <http://repository.tudelft.nl/>.

Abstract

Randomly occurring torque transients have been detected in the reaction wheels of the XMM-Newton, Venus Express, Cassini and other spacecraft. The causes of the transients are presumably cage instabilities and oil jogs occurring in the ball bearings of the wheels. Within high precision pointing missions these disturbances significantly impair pointing-stability performance, especially they are a great concern when occurring during steady-state observations. Thus, the control system should optimally counteract these disturbance transients.

Solutions to prevent the occurrence of these disturbances have been suggested at an hardware level. The goal of this thesis is to investigate how the impact of wheels' disturbance transients on the pointing performance parameters can be minimized through the implementation of dedicated control strategies. Eventually, the capabilities of the Precision Pointing Control Design tool developed by Airbus Defence and Space can be further extended and improved with respect to friction torque instabilities.

The torque profiles generated by friction instabilities have been characterized by the means of a pseudo-power spectral density formalism allowing to analytically perform accurate pointing error analysis and evaluations. Moreover, two different solutions have been investigated and implemented on a reference case study mission. The first one, consisting in the optimization of the controller's integral bandwidth with respect to the disturbance transients, leads to considerable pointing performance improvements but, on the other hand, the system stability is impaired and jeopardized. The second solution, that considers the design of a wheel speed control loop, provides even greater enhancements of the control system disturbance rejection capabilities.

The implementation of an inner control loop nested in the global attitude control loop turns out to be the most promising strategy for handling disturbance transients. However, the research shows that angular rate sensors are a crucial element for the pointing performance and stability of the whole control loop. Therefore, at the end of the thesis, guidelines to further optimize the in-house control design tool and to characterize the pointing error sources analytically are presented. Additionally, in order to pave the way for a practical implementation of the wheel speed loop strategy, the specific requirements regarding the rate sensor that should be provided to the wheels' manufacturer are discussed.

Contents

List of Figures	vii
List of Tables	xi
List of Symbols	xiii
List of Acronyms	xv
1 Introduction	1
1.1 Problem Context	2
1.1.1 Pointing Error Engineering Framework	2
1.1.2 Precision Pointing Control Design Tool	2
1.2 Thesis Objective	3
1.3 Methodology Overview	4
1.4 Thesis Outline	5
2 Theoretical Background	7
2.1 Spacecraft Attitude Dynamics Control	7
2.1.1 Reaction Wheel Assembly Overview	8
2.1.2 Reaction Wheel Disturbances	8
2.1.3 Origins of Disturbance Transients	9
2.2 Control Theory	10
2.2.1 Closed-Loop Stability	12
2.2.2 Closed-Loop Performance	12
2.3 Fourier Analysis	13
2.3.1 Aperiodic Signal Analysis	13
2.3.2 Periodic Signal Analysis	14
2.4 Pointing Error Indices	15
2.4.1 Stochastic Measures	15
2.4.2 Time Domain Description	16
2.4.3 Frequency Domain Description	17
2.4.4 Pointing Error Analysis	19
3 Parametric Pointing Performance Estimation	21
3.1 Frequency Domain Analysis of Disturbance Transients	22
3.1.1 Signal Characterization	22
3.1.2 Derivation of the Pseudo-Power Spectral Density Formalism	23
3.2 Analytical Pointing Performance Estimation	23
3.2.1 Plateaus and Spikes Torque Transfer Analysis	24
3.2.2 Pointing Error Evaluation	26
3.2.3 Verification	27
3.3 Discussion of Results	30
4 Optimization of the H_∞ Controller Integral Action	31
4.1 General	32
4.2 Integral Action Optimization	35
4.2.1 Controller Synthesis	35
4.2.2 Application to the Reference Case Study	36
4.3 Pointing Performance Evaluation	38
4.3.1 Plateaus Disturbance Case Study	38
4.3.2 Spike Disturbance Case Study	39
4.3.3 Stability Margins	41
4.3.4 Simulation Results	41

4.4 Discussion of Results	41
5 Design of a Wheel Speed Control Loop	43
5.1 General	44
5.2 Angular Rate Sensor Model	45
5.2.1 Fixed Delay Mode	47
5.2.2 Variable Delay Mode	49
5.2.3 Sensor Model Implementation.	51
5.3 Wheel Speed Loop Design	52
5.4 Pointing Performance Evaluation	56
5.4.1 Plateaus Disturbance Case Study	56
5.4.2 Spike Disturbance Case Study	58
5.4.3 Stability Margins	59
5.4.4 Simulation Results	59
5.5 Discussion of Results	60
6 Conclusions	63
6.1 Summary	63
6.2 Outlook	65
A Reference Case Study	69
B Mathematical Derivations	73
B.1 Pseudo-Power Spectral Density Derivations.	73
B.2 Plateaus ans Spikes Profiles Characterization	73
C Mitigation Methods	77
C.1 PID Controller Case Study.	77
C.2 Further Results for the Integral Action Optimization	78
C.3 Angular Rate Sensor Model	79
C.4 Wheel Speed Loop Controller Design	81
C.5 Further Results for the Wheel Speed Loop Implementation	82
Bibliography	83

List of Figures

1.1	Plateaus drag torque profile observed on the wheel telemetry of Cassini spacecraft, [20]	1
1.2	Spikes drag torque profile observed on the wheel telemetry of Cassini spacecraft, [20]	1
1.3	Systematic Precision Pointing Control Design approach developed by Airbus Defence and Space, [25]	2
1.4	Diagram of the thesis project context and objective	4
1.5	Methodology implemented to derive guidelines for optimal control of wheels disturbance transients	5
2.1	Standard spacecraft attitude control subsystem structure	7
2.2	Typical reaction wheel assembly design, courtesy of [2]	8
2.3	Standard notation, according to [32]: general control configuration (a) and one degree-of-freedom control configuration (b)	10
2.4	Attitude control problem described with the general control configuration	11
2.5	Attitude control problem described with the one degree-of-freedom control configuration	11
2.6	Propagation of the error sources' power spectral density through a linear time-invariant system	16
2.7	Time dependencies of the various pointing errors	17
2.8	Frequency-domain weighting filter definitions of the the various time-dependencies errors, according to [11]	18
2.9	Standard control design approach within the pointing error engineering framework, as provided by [11]	19
3.1	Overview of the third chapter's contents	21
3.2	Profile of periodic plateaus torque instabilities in the time domain	22
3.3	Profile of periodic spikes torque instabilities in the time domain	22
3.4	Pseudo-power spectral density (left plot) and cumulative sum of the latter (right plot) for plateaus and spikes torque profiles	24
3.5	Variation of the PEC's integral with respect to the plateau transient's duration T_d	25
3.6	ACS pointing error sources transfer analysis diagram	26
3.7	APE cumulative spectral variance (plateaus profile)	27
3.8	RPE cumulative spectral variance (plateaus profile)	27
3.9	MPE cumulative spectral variance (plateaus profile)	28
3.10	PDE cumulative spectral variance (plateaus profile)	28
3.11	APE cumulative spectral variance (spikes profile)	29
3.12	RPE cumulative spectral variance (spikes profile)	29
3.13	MPE cumulative spectral variance (spikes profile)	29
3.14	PDE cumulative spectral variance (spikes profile)	29
4.1	Overview of the fourth chapter's contents	31
4.2	Time-domain response of a PD controller (left figure) and of a PID controller (right figure) when a plateau transient is introduced as disturbance	33
4.3	Magnitude plots of disturbance and noise rejection characteristics of a PID-based attitude control system, transfer functions are evaluated for different values of integral bandwidth	33
4.4	Step responses of a PID-based attitude control system evaluated for different values of integral bandwidth	34
4.5	Closed-loop system's root locus for a PID-based attitude control system as the integral gain varies	34
4.6	Closed-loop system diagram (SISO) for integral action optimization	35
4.7	Integral gain optimization procedure diagram	36
4.8	RPE budget for optimal tuning of the controller integral gain (x axis)	36
4.9	Stability margins' evolution with respect to the value of integral coefficient (x axis)	37

4.10 Time-series of the plateaus disturbance contribution on APE	39
4.11 Time-series of the plateaus disturbance contribution on RPE	39
4.12 Time-series of the plateaus disturbance contribution on MPE	39
4.13 Time-series of the plateaus disturbance contribution on PDE	39
4.14 Time-series of the spikes disturbance contribution on APE	40
4.15 Time-series of the spikes disturbance contribution on RPE	40
4.16 Time-series of the spikes disturbance contribution on MPE	40
4.17 Time-series of the spikes disturbance contribution on PDE	40
4.18 Overall pointing performance comparison between $K_{\infty,\text{opt}}$ and K_{∞} control strategies, with respect to a plateaus disturbance	42
4.19 Overall pointing performance comparison between $K_{\infty,\text{opt}}$ and K_{∞} control strategies, with respect to a spikes disturbance	42
 5.1 Overview of the fifth chapter's contents	43
5.2 Block diagram of two different wheels control loop configurations: <i>speed loop</i> (b) and <i>torque loop</i> (a)	44
5.3 Comparison between the outer attitude control loop and the wheel speed loop bandwidths	45
5.4 Basic functional block diagram of a Hall-effect based rate sensor	46
5.5 Block diagram of the wheel speed loop in the <i>H-loop</i> configuration with the linear model of the tachometer	46
5.6 Sample & Holder effect and additional delay introduced by the angular rate sensor, according to RW Simulink block output	47
5.7 Graphical explanation of the resolution error for fixed delay mode algorithm. Case 1 represents the most favorable case scenario. Case 2 represents the worst case scenario	48
5.8 Simulation output of the RW Simulink block with <i>fixed delay mode</i>	48
5.9 Resolution error distribution with <i>fixed delay mode</i>	48
5.10 Variation of the rate sensor's sampling time with respect to an increasing wheel's rate profile	49
5.11 Comparison between the RW Simulink model output and the expected noise-free behavior of the rate sensor model	50
5.12 Delay and jitter noise generated within the wheel speed loop with a <i>variable delay mode</i> implemented in the rate sensor	51
5.13 Noise and delay performance with variable pulses-counter (VPC) scheduling approach implemented in the rate sensor	51
5.14 Angular rate sensor estimation algorithms comparison	52
5.15 Comparison of the tachometer linear model (dark dots) and the RW Simulink model output (light dots)	52
5.16 ACS block diagram with the wheel speed loop implemented (SISO)	53
5.17 RPE budget for different values of the derivative coefficient (<i>x</i> axis)	54
5.18 Stability margins for different values of the derivative coefficient (<i>x</i> axis)	54
5.19 ACS closed-loop transfer function comparison without wheel speed loop (dashed lines) and with wheel speed loop (solid line)	55
5.20 Noise and disturbance transmission comparison through the ACS loop (yellow lines) and the wheel speed loop (red lines)	55
5.21 Derivation of the maximum electrical jitter noise allowed to the angular rate sensor	56
5.22 Time-series of the plateaus disturbance contribution on APE	57
5.23 Time-series of the plateaus disturbance contribution on RPE	57
5.24 Time-series of the plateaus disturbance contribution on MPE	58
5.25 Time-series of the plateaus disturbance contribution on PDE	58
5.26 Time-series of the spikes disturbance contribution on APE	59
5.27 Time-series of the spikes disturbance contribution on RPE	59
5.28 Time-series of the spikes disturbance contribution on MPE	59
5.29 Time-series of the spikes disturbance contribution on PDE	59
5.30 Overall pointing performance comparison between $K_{\infty,\text{RW}}$ and K_{∞} control strategies, with respect to a plateaus disturbance	61
5.31 Overall pointing performance comparison between $K_{\infty,\text{RW}}$ and K_{∞} control strategies, with respect to a spikes disturbance	61

6.1 Overall pointing performances about the x axis with plateau profile disturbance transients occurring	64
6.2 Overall pointing performances about the x axis with spike profile disturbance transients occurring	64
6.3 Outlook of the precision pointing control design framework extended to disturbance transients	65
6.4 Outlook of the state-space control problem formulation including wheels speed loop	66
A.1 Solar pressure disturbance's weighting filter with respect to the x axis	70
A.2 Solar pressure disturbance's weighting filter with respect to the y axis	70
A.3 Solar pressure disturbance's weighting filter with respect to the z axis	70
A.4 Measurements noise's weighting filter with respect to the x axis	71
A.5 Measurements noise's weighting filter with respect to the y axis	71
A.6 Measurements noise's weighting filter with respect to the z axis	71
C.1 Constant wheel speed scenario with <i>fixed delay mode</i> implemented in the angular rate sensor	79
C.2 Graphical illustration of the numerical issue introduced by time domain discretized simulations	80
C.3 Numerical deviations in ARS Simulink model output due to the time discretization	80
C.4 Stability margins for different values of the inner loop controller's proportional gain (x axis)	81
C.5 RPE budget for different values of the inner loop controller's proportional gain (x axis)	81
C.6 RPE budget for different values of the inner loop controller's integral gain (x axis)	81

List of Tables

2.1	Stochastic measures definition for a stationary random noise process	15
2.2	Time-domain metrics definitions of the performance error indices, according to [11]	17
2.3	Frequency-domain metrics definitions of the performance error indices, according to [11]	18
3.1	Plateaus and spikes torque profiles' pseudo-power spectral density expressions	24
3.2	Parametric formulas for pointing error contributions' estimations with respect to a plateaus disturbance	26
3.3	Transfer function from the different input noise/disturbances (rows) to the absolute pointing error index	26
3.4	Pointing error contributions of plateaus disturbance calculated analytically and numerically	28
3.5	Global pointing performances with respect to plateaus disturbance calculated analytically and numerically	28
3.6	Pointing error contributions of spike disturbance calculated analytically and numerically	29
3.7	Global pointing performances with respect to spikes disturbance calculated analytically and numerically	30
4.1	Pointing error budget with respect to a plateaus disturbance, (x axis)	38
4.2	Relative increase/decrease in the different pointing error contributions after integral action optimization (plateaus disturbance)	38
4.3	Pointing error budget with respect to a spikes disturbance, (x axis)	39
4.4	Relative increase/decrease in the different pointing error contributions after integral action optimization (spikes disturbance)	40
4.5	Comparison of the stability margins obtained with the $K_{\infty,\text{opt}}$ and K_{∞} control strategies (x axis)	41
4.6	Results of the pointing error evaluation conducted by means of numerical simulations (x axis)	41
5.1	Transfer function from the different input noise/disturbances (rows) to the absolute pointing error index	53
5.2	Pointing error budget with respect to a plateaus disturbance, (x axis)	57
5.3	Relative increase/decrease in the different pointing error contributions after the implementation of a wheel speed loop (plateaus disturbance)	57
5.4	Pointing error budget with respect to a spikes disturbance, (x axis)	58
5.5	Relative increase/decrease in the different pointing error contributions after the implementation of a wheel speed loop (spikes disturbance)	58
5.6	Comparison of the stability margins obtained with the $K_{\infty,\text{RW}}$ and K_{∞} control strategies (x axis)	59
5.7	Results of the pointing error evaluation conducted by means of numerical simulations (x axis)	60
A.1	Control system characteristic parameters within the reference case study	69
A.2	Reference case study parameters of the windowed pointing error indices	70
A.3	Reference case study parameters of plateaus and spikes instability profiles	71
A.4	Stability margins requirements used within the H_{∞} synthesis	72
C.1	PID controller parameters used for preliminary investigation on the integral action	77
C.2	Pointing error budget with respect to the y axis	78
C.3	Comparison of the stability margins obtained with the $K_{\infty,\text{opt}}$ and K_{∞} control strategies (y axis)	78
C.4	Pointing error budget with respect to the z axis	78
C.5	Comparison of the stability margins obtained with the $K_{\infty,\text{opt}}$ and K_{∞} control strategies (z axis)	78
C.6	Pointing error budget with respect to the y axis	82
C.7	Comparison of the stability margins obtained with the $K_{\infty,\text{RW}}$ and K_{∞} control strategies (y axis)	82
C.8	Pointing error budget with respect to the z axis	82
C.9	Comparison of the stability margins obtained with the $K_{\infty,\text{RW}}$ and K_{∞} control strategies (z axis)	82

List of Symbols

In general, matrices are denoted by bold uppercase symbols (**A**), vectors are denoted by bold lowercase symbols (**a**), and scalars are denoted by normal-weight italic symbols (*A, a*).

Latin Symbols

h, h	Angular momentum
J, J	Moment of inertia
S_{xx}, S_{xx}	Double-sided power spectral density of the process $x(t)$
G_{xx}, G_{xx}	Single-sided power spectral density of the process $x(t)$
C_{r2b}	Direction cosine matrix from wheel-frame to body-frame
H, H	General input-output system transfer function
h, h	Angular momentum
<i>t</i>	Time
<i>w</i>	State-space exogenous disturbance input
<i>z</i>	State-space exogenous output
<i>v</i>	State-space control input
<i>u</i>	State-space control signal
<i>d</i>	SISO system disturbance input
<i>r</i>	SISO system reference
<i>n</i>	SISO system noise input
<i>y</i>	SISO system output
<i>s</i>	Complex variable
<i>j</i>	Imaginary unit
<i>f</i>	Frequency in [Hz]
<i>L(s)</i>	Open loop transfer function
<i>S(s)</i>	Sensitivity transfer function
<i>T(s)</i>	Complementary sensitivity transfer function
<i>G(s)</i>	Plant transfer function
<i>K(s)</i>	Controller transfer function
<i>k</i>	Controller coefficient
<i>F_{metric}(s)</i>	General input-output system transfer function
<i>f₀</i>	Fundamental harmonic in [Hz]
<i>x(t)</i>	Generic periodic/aperiodic signal
<i>X(ω)</i>	Fourier transform of a generic aperiodic signal
<i>E_x</i>	Aperiodic signal normalized energy
<i>P_x</i>	Periodic signal average power
<i>z_k</i>	Fourier series coefficient of a generic periodic signal
<i>T_d</i>	Disturbance transient's duration in [s]
<i>T_p</i>	Disturbance transient's period in [s]
<i>b₀(t), b(t)</i>	Single rectangular function, rectangular waveform
<i>p₀(t), p(t)</i>	Single triangular function, triangular waveform
<i>T_S</i>	Sampling time in [s]
Δt_{RW}	Reaction wheel delay
Δt_{ARS}	Angular rate sensor delay
<i>N_{ARS}</i>	Number of pulses counted by the angular rate sensor
<i>n_{ARS}</i>	Number of rate sensor's slits on the reaction wheel
<i>m_{ARS}</i>	Number of pulses counted by the angular rate sensor in variable delay mode

Greek Symbols

τ, τ	Torque in [Nm]
ϕ	Generic attitude angle
μ	Mean value
σ	Standard deviation
σ^2	Variance
ψ^2	Mean square value
ω	Angular frequency in [rad/s]
ω_0	Fundamental harmonic in [rad/s]

Mathematical Operators

$(\dots)^{-1}$	Inverse
$(\dots)^*$	Complex conjugate transpose
$(\dots)^T$	Transpose
$\ \dots\ _\infty$	Infinity norm
$E[\dots]$	Expected value
$\mathcal{F}\{\dots\}$	Fourier transform operator
\dot{f}	Time derivative of a function f
$\text{sinc}(\dots)$	Cardinal sine function

List of Acronyms

ESA	European Space Agency
MTG	Meteosat Third Generation
RW	Reaction Wheel
2PCD	Precision Pointing Control Design
PEI	Performance Error Index
HPP	High Precision Pointing
DS	Defence and Space
FTI	Friction Torque Instability
AOCS	Attitude and Orbit Control Subsystem
ACS	Attitude Control Subsystem
RW	Reaction Wheel
RWA	Reaction Wheel Assembly
WDE	Wheel Drive Electronics
EHD	Elasto-Hydro-Dynamic
ARS	Angular Rate Sensor
MIMO	Multi-Input/Multi-Output
SISO	Single-Input/Single-Output
PM	Phase Margin
GM	Gain Margin
DM	Delay Margin
PSD	Power Spectral Density
LTI	Linear Time Invariant
PES	Pointing Error Source
PEC	Pointing Error Contribution
AST	Analysis Step
WV	Windowed Variance
WM	Windowed Mean
WMS	Windowed Mean Stability
APE	Absolute Pointing Error
RPE	Relative Pointing Error
MPE	Mean Pointing Error
PDE	Pointing Drift Error
PD	Proportional-Derivative
PI	Proportional-Integral
PID	Proportional-Integral-Derivative
DC	Direct Current
BLDC	Brushless DC
VPC	Variable Pulse-Counter

Indices

u	Control
d	Disturbance
n	Noise
w	Window
rw	Reaction wheel
SC	Spacecraft
PL	Plateaus
SP	Spikes
cmd	Command
max	Maximum value
ref	Reference
sta	Stability
ind	Generic pointing error index
real	Real process value
CL	Closed Loop
P	Proportional
PD	Proportional-Derivative
PI	Proportional-Integral
SS	Steady-State
PID	Proportional-Integral-Derivative
ACS	ACS loop
RW	RW speed loop
ZOH	Zero order hold

Preface

Since my Bachelor studies, spacecraft attitude dynamics control has attracted my interest, due to my deep passion for mathematics and physics. As a result, during the Master in Space Engineering at the Delft University of Technology I aimed my studies in this direction, successfully completing an internships related to this topic in the Space System Department at SITAEL. Eventually, my interests brought me to Airbus Defence and Space in Friedrichshafen, where I had the great opportunity to complete my final thesis. The project has been very challenging since the beginning, due to the novelty of the topic addressed. The 7 months of thesis work was completed within the Flight Dynamics and AOCS/GNC Department (TSOTO31) of Airbus Defence and Space and the results are presented in this report.

Acknowledgement

After five years of studies I reached the conclusion of a very long journey that shaped me both as a person and as a space engineer. The Delft University of Technology offered me a great international experience that has been fundamental for my professional and personal growth. Therefore, thinking back to those times I see an incredible amount of people that I would like to thank.

First of all, I would like to express my sincere gratitude to the people who have helped me during the thesis: Dr. J. Guo for his guidance throughout the project and his very helpful advices that he provided me with during the final phases of it, my Airbus supervisors, T. Ott and M. Vitelli, that despite all the workload they had in the last months always found a time-slot to answer my questions and motivate me. Additionally, I would like to thank the whole group of fellow interns from Airbus with whom I shared a lot of amazing experiences, especially I am very grateful to my officemate Gustavo for his endless patience when I was desperately stuck on my work, the hilarious moments we had together and the valuable advices he gave me even when discussing about everyday life. Furthermore, my special thanks go to all my flatmates that I lived together with for the past 7 months in Germany, they constantly supported me and I now consider them as my German family. Then, a noticeable thank to Prof. Dr. E. K. A. Gill and Dr. Q. P. Chu for reading my thesis and completing my committee.

Last, but definitely not least, I owe my deepest gratitude to my parents, Alberto and José, for their unlimited support they provided me with and the great sacrifices they endured in the past 5 years to bring me where I am now. Their unconditional love and faith in me will remain a true source of inspiration throughout my whole life. I will be forever in your debt. Then, I would like to thank my little sister, Caterina, since being a valid role model for her has always pushed me to do my best, and my grandparents, Gaetano and Agnese, that even flew to the Netherlands to attend my graduation. Finally, I thank my girlfriend, Valentina, for the enormous support she gave me despite the distance, being always there listening to my problems and providing me with wise advices and energy boosts to keep going with the project.

*Edoardo Coccia
Delft, October 2016*

Introduction

Future satellite science missions, e.g. the European Space Agency (ESA) mission Meteosat Third Generation (MTG), will be characterized by high pointing performance requirements, in the order of 10^{-3} arcsec, [25]. Pointing performance requirements address instantaneous attitude errors as well as additional error indices which analyze the attitude error as it evolves over specific time windows. As a result, also time-windowed performance parameters are taken into account in the design of the Attitude Control System (ACS) of these highly demanding space missions.

Most science and Earth observation spacecraft are equipped with reaction wheels based attitude control solutions. When wheels are rotating within certain speed ranges, disturbance transients have been observed in the in-flight telemetry within several occasions, [20] and [16]. They are characterized by two distinct torque profiles, the first type of disturbances is addressed as *plateaus transients*, and it is illustrated in Figure 1.1, while the second type is addressed as *spikes transients*, and it is illustrated in Figure 1.2. Both are deemed to be due to instabilities occurring in the ball bearings of reaction wheels and they can considerably impair the pointing-stability performance of the spacecraft, sometimes also leading to a failure of the wheel. Both instantaneous and time-windowed pointing performance parameters mentioned above are greatly affected.

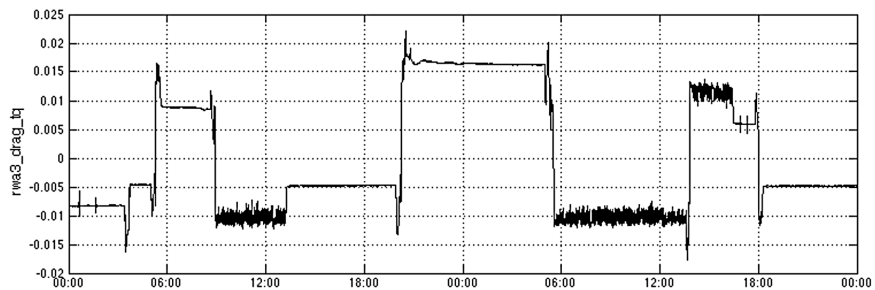


Figure 1.1: Plateaus drag torque profile observed on the wheel telemetry of Cassini spacecraft, [20]

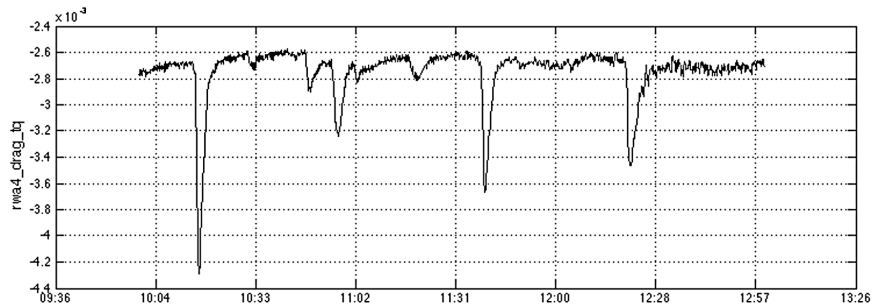


Figure 1.2: Spikes drag torque profile observed on the wheel telemetry of Cassini spacecraft, [20]

Then it follows that within high precision pointing missions the occurrence of these friction instabilities related

disturbances is a great concern for pointing-stability performance, especially when occurring during steady-state (SS) observations.

In the following, the problem's background is briefly introduced and then a summary of the literature study performed about wheels related disturbances is provided in order to explain the needs and the motivations that are driving this work. Consequently the thesis objective is defined and based on these considerations a research methodology is formulated. Eventually, according to the latter, the thesis report structure is outlined.

1.1. Problem Context

1.1.1. Pointing Error Engineering Framework

Within high precision pointing (HPP) missions, pointing-stability requirements are getting considerably demanding, hence in the recent years the development of a global and systematic approach to assess the impact of each single Pointing Error Source (PES) on the overall pointing performance was required. A Pointing Error Engineering methodology has been formulated in [11], and specifically applied to the Attitude and Orbit Control Subsystem (AOCS), [5]. A set of pointing error indices is defined and presented as the standard way to accurately describe and assess the pointing performance of an attitude control system.

In [11] two methods are commended as far as pointing-stability performance analysis is regarded. The first one consists in a simplified statistical method where the PES's are simply described by a variance, σ , and mean, μ , obtained either via time-domain simulations or assuming a standard error distribution. In the early design phase the simplified method is sufficient to provide first-order knowledge of the pointing error budget allocation. The second approach is instead to be used when a more detailed analysis needs to be performed, such as it is the case for high precision pointing space missions. It consists in an advanced statistical method according to which all the different PES's are modeled by means of a Power Spectral Density (PSD), as well as it is done for their contribution to the error indices. As the advanced method is concerned, it has to be stressed that the mathematical tools required to describe non-stationary transient processes, like plateaus and spikes transients, are not yet addressed in [11]. However, friction instabilities disturbance torques are crucial for high precision pointing missions, consequently a way to include these deterministic PES's in the advanced statistical method shall be developed.

1.1.2. Precision Pointing Control Design Tool

As far as the attitude dynamics of the spacecraft is concerned, classical control design methods are not capable of optimizing an Attitude Control Subsystem (ACS) with respect to all the absolute and windowed pointing-stability requirements systematically, an iterative approach is indeed commonly used, [24]. Therefore, a systematic control design methodology has been recently developed by Airbus Defence and Space (DS) which allows the synthesis of a robust controller in a systematic sequential manner. The Precision Pointing Control Design (2PCD) tool, [25], whose general logic is described in Figure 1.3, consists mainly of two steps.

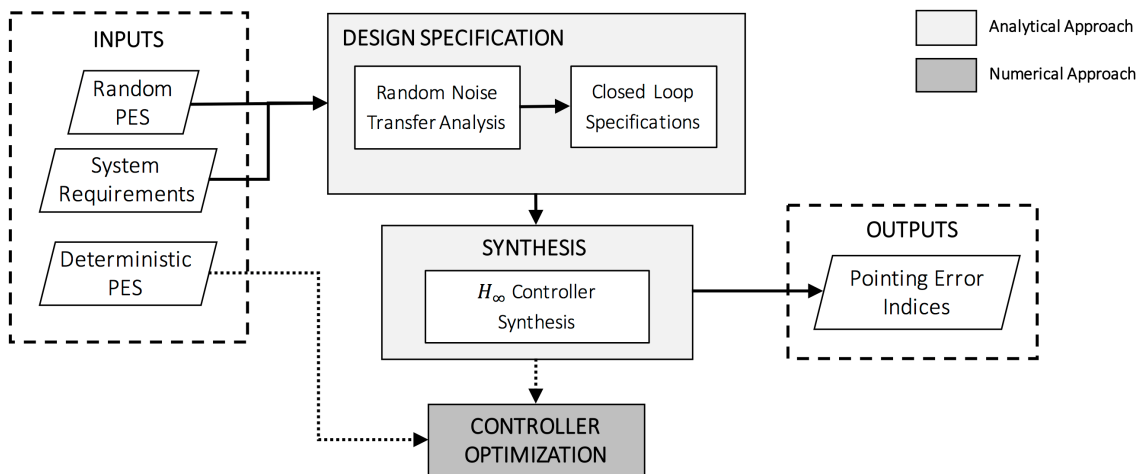


Figure 1.3: Systematic Precision Pointing Control Design approach developed by Airbus Defence and Space, [25]

Given different random noise error sources and the pointing-stability requirements, system specifications are derived, in terms of sensitivity and complementary sensitivity transfer functions. Then, an H_∞ synthesis is performed in order to obtain a controller that complies with all the pointing performance requirements considered in the previous step. Stationary random noise PES's are treated analytically in the frequency domain as suggested in [11], i.e. described by means of the PSD formalism, hence the overall system specification and synthesis process is purely analytical and no simulations are required among the loop. Nevertheless, since friction torque instabilities and the disturbance transients that they generate have been proved to be a major concern as far as SS operations of HPP missions are considered, a further controller tuning step has been added next to the H_∞ synthesis. Given the importance of these non-stationary disturbances the integral part of the controller is further optimized with respect to a step input, aiming to improve robustness of the controller with respect to undesired disturbances concentrated at low frequencies, [24]. This is currently done by means of iterative numerical simulations, since a detailed description in the frequency domain of the disturbance transients at issue has not yet been investigated.

1.2. Thesis Objective

It has been largely proven that the disturbance transients generated by reaction wheels can considerably impair the pointing-stability performance of a spacecraft, threatening the outcome of the whole mission, as discussed in [20] and [16]. Recently, spacecraft like Mars Odyssey, Kepler, the ESA Rosetta, Cassini and XMM-Newton have experienced bearing-related anomalies. Within the last two missions mentioned mitigation solutions have been proposed to handle this problem. The use of lubricants reservoirs was foreseen on the XMM-Newton spacecraft in [26], however the re-lubrication procedure, even though it can be regarded as a preventive strategy, can be applied only for a limited amount of times, [17]. A new AOCS mode was also investigated in [16] and [30] implementing a specific wheel's *de-caging* procedure. Maintaining the wheel speed below 1000 [RPM] is believed to be a valid solution to reduce the occurrence of cage instabilities, but on the other hand oil jogs become dominant at lower speed. On Cassini, a PI estimator of the bearing drag torque was added to the controller in order to locally compensate anomalous constant disturbances. Additionally, contingency hybrid controllers are suggested by [20] in order to let the system be able to cope with unexpected bearings degradation that, as proven by observations, can occur on multiple wheels.

Most of the solutions indicated however concern the reaction wheel hardware, whereas the strategies implemented at a control level consist only in procedures aimed to restore nominal conditions after the instabilities have already occurred. As a result, the output of this work should provide a valid control strategy at a software-level, so that the impact of these disturbances on pointing-stability performance is preventively handled. For HPP space missions the control system is generally designed with the aim of minimizing the spin rate of the wheels, as it was done for the Euclid mission in order to avoid micro-vibrations issues. Additionally, this is also important to ensure that the angular momentum capacity limit is not violated and that reaction wheels' lifetime is maximized, since the latter is usually expressed in terms of total revolutions. Nevertheless a further limit exists, spin rate shall be also maintained above the sub-Elasto-Hydro-Dynamic (EHD) boundary. When the spin rate drops below roughly 250 [RPM] the bearings enter a lubrication condition with metal-to-metal contacts between the balls and the races [20]. When this happens, the shear stress level increases as well as the drag torque. The resulting overheating leads to lubricant polymerization and a possible subsequent bearing failure. Then, in the available range of speeds considered, according to the literature presented spikes and plateaus transients occur in an unpredictable manner, jeopardizing the pointing performance of the spacecraft.

The main objective of this work is to analyze current and prospective reaction wheel based attitude control system strategies that can be employed in order to handle the above mentioned disturbance transients. In contrast with the common practice, according to which countermeasures for such disturbances have been mostly applied only at the hardware level, solutions at the control system design level are hereby investigated. The analysis is performed within the 2PCD frame and the H_∞ controller derived by means of it is considered as the reference starting point for the implementation of mitigation methods. As illustrated in Figure 1.4 the goal is eventually to extend the capabilities of the 2PCD tool, to obtain a control system that is also optimized with respect to wheels disturbance transients.

In order to achieve this goal, plateaus and spikes transients are analytically characterized in the frequency domain in order to make the control design process consistent with the analytical approach used in the tool within the H_∞ synthesis framework. A further benefit is that such analysis would allow wheels disturbance transients be included in the advanced statistical pointing error engineering approach. The latter would be eventually provided with the mathematical tools to describe and thus include also these error sources in the standard for

AOCS pointing error budget and analysis provided by [11].

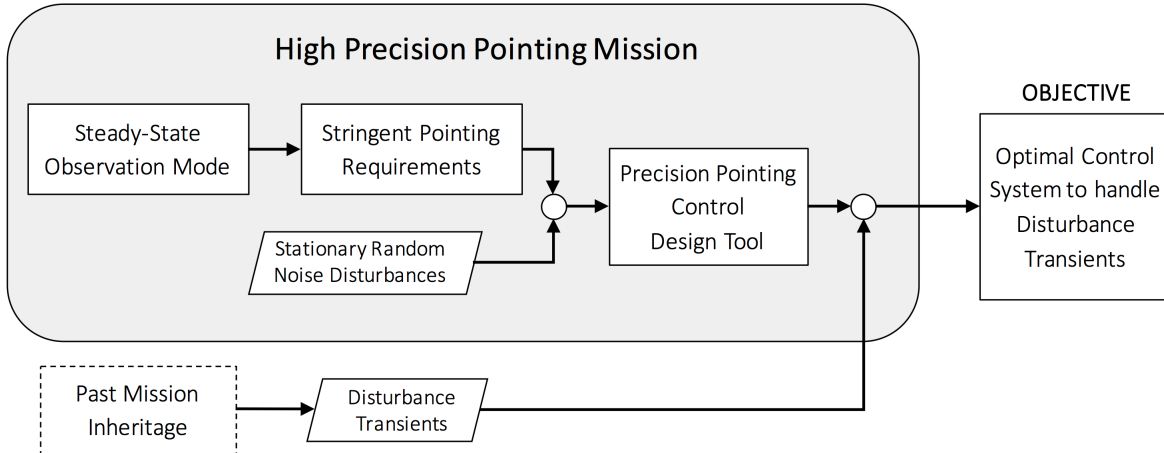


Figure 1.4: Diagram of the thesis project context and objective

1.3. Methodology Overview

The thesis project is approached systematically following a series of research questions that can be disclosed given the reasoning introduced in the previous sections. This section is indeed intended to provide an overview of the steps tackled and the research methodology developed in order to achieve the primary objective of the thesis.

In order to come up with a valid control solution to mitigate the effects of friction torque instabilities, the error source at issue should firstly be properly investigated and characterized. Therefore the first research question is formulated as follows:

Q.1 : How can the impact of wheels disturbance transients be characterized?

In details, the torque disturbances at issue are characterized analytically in the frequency domain and a Parametric Pointing Performance Estimation (*3PE*) tool has been developed. It consists in the definition of a *pseudo-PSD* formalism aimed to analyze this specific kind of error sources following the standard approach provided in [11]. The main benefits that can be achieved with the development of this mathematical tool are listed here below.

- Within the control design framework of the *2PCD* tool, the tuning of the ACS controller with respect to these disturbances can be performed analytically, hence avoiding time-consuming numerical simulations. Furthermore the approach would be consistent with the one used to characterize stationary random noise sources that are considered in the H_∞ control design tool.
- Once characterized in the frequency domain, deeper insights into the disturbance characteristics can be inferred. When a signal is represented in the frequency domain, via its PSD for example, it is easier to identify which is the frequency range where most of the signal power is concentrated. Such information can be used firstly to distinguish which pointing error index would be affected more than the others and later to tune the controller accordingly.
- The tool is also addressed as *parametric* because the impact of plateaus and spikes on the pointing performance can be described by analytical expressions explicitly depending on the disturbance profiles characteristics. These parametric formulas can be used to perform sensitivity analysis quickly without the need of simulations and also to further optimize the pointing error budget.
- Additionally, plateaus and spikes disturbances can be included in the advance statistical approach of the pointing error engineering methodology.

Once the tools, through which the problem can be handled analytically, have been developed and verified the following step consists in the investigation of mitigation methods that can be used to reject disturbances generated by friction torque instabilities. As a result the second main research question is formulated as follows:

Q.2 : Which control strategies can be used in order to handle wheels disturbance transients?

Firstly the integral action optimization solution, already mentioned above and proposed by [24], is further investigated and extended to plateaus and spikes torque profiles. Secondly, instead of optimizing the controller obtained through the H_∞ synthesis, a cascade control strategy is considered. In order to compare the performance enhancements brought by the two methods, in both cases the proposed control strategy should be optimally designed and implemented in a reference attitude pointing system, then the pointing-stability performance should be evaluated. In order to do so, the analytical tool developed before is used to design and optimize the control strategies investigated within a specific reference case study, which is described in Appendix A.

As a result, in Figure 1.5 the approach used to derive guidelines to improve the control system capabilities with respect to wheels disturbances is illustrated. Once an analytical characterization of the disturbance transients is carried out, the starting point is the design, by means of the 2PCD tool, of the H_∞ controller that optimizes the transfer characteristics of the system with respect to stationary random noise and disturbances. This is considered as the reference control system with respect to which performances of the two other mitigation control methods are compared. Consequently the controller is optimized so that disturbance rejection performance are further improved by implementing the two different solutions introduced above. In both cases, the pointing performance is then evaluated analytically following the pointing error engineering guidelines provided by [11]: performing a global system pointing performance evaluation and also evaluating the different Pointing Error Contributors (PEC's). With this respect, the 3PE analytical tool is used in order to specifically address wheels disturbance transients.

Additionally, the following analysis takes into account a linearized SISO model of the control problem, therefore numerical simulations of the complete ACS model are conducted in parallel to verify performance's improvements even when nonlinearities are taken into account.

The pointing-stability performance obtained with the different control strategies are then compared and eventually guidelines are derived to provide insights on further possible developments.

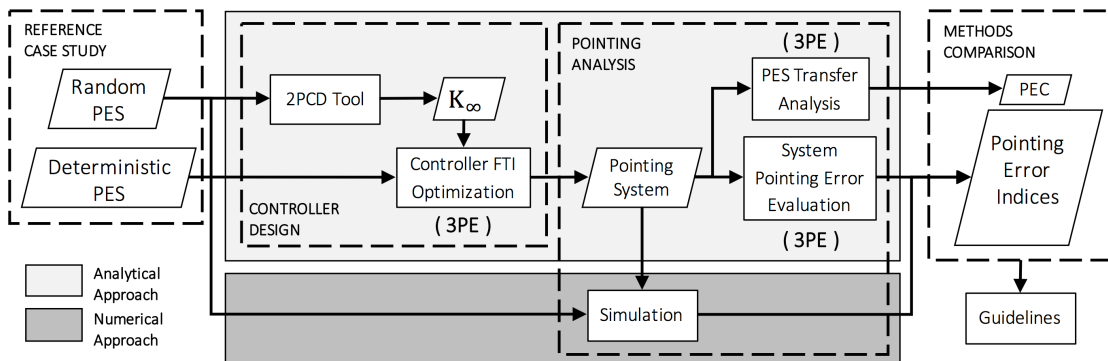


Figure 1.5: Methodology implemented to derive guidelines for optimal control of wheels disturbance transients

1.4. Thesis Outline

This thesis contains 6 chapters, starting with Chapter 1, where the problem has been presented together with the methodology applied among the thesis. Then Chapter 2 is meant to provide the basics of spacecraft attitude control and the mathematical tools required to understand the content of the overall work.

The following chapters, instead, represent the core of the thesis report, where the relevant contributions of this work are presented. Chapter 3 addresses the first research question introduced within the description of the research methodology. An analytical tool to describe the torque profiles of these disturbances is developed and then verified numerically. Afterward, Chapter 4 and 5 deal with the two control strategies investigated. The methodology illustrated in Figure 1.5 is applied in both cases with respect to the common reference case study

in order to compare results.

The results are then gathered and critically discussed in Chapter 6 where, eventually, also an outlook for the following steps expected to be carried out to further improve control capabilities with respect to these disturbances are provided.

2

Theoretical Background

2.1. Spacecraft Attitude Dynamics Control

The attitude control subsystem is an essential element since it is given with the task of stabilize and control the attitude (orientation) of the spacecraft. In the past, when pointing accuracy requirements were still coarse, passive methods of attitude stabilization were used. However, nowadays high accuracy is required because the scientific payloads carried on-board have highly demanding pointing-stability requirements. Therefore such spacecraft are actively controlled by specific actuators, driven by the ACS.

According to [8] the basic structure of an ACS can be summarized as illustrated in Figure 2.1. Attitude sensors measure the attitude of the spacecraft within a certain degree of accuracy. Then the information is fed into the controller, that consists in the electronics where the control law, used to calculate the control torque that the actuators should provide to the spacecraft is implemented.

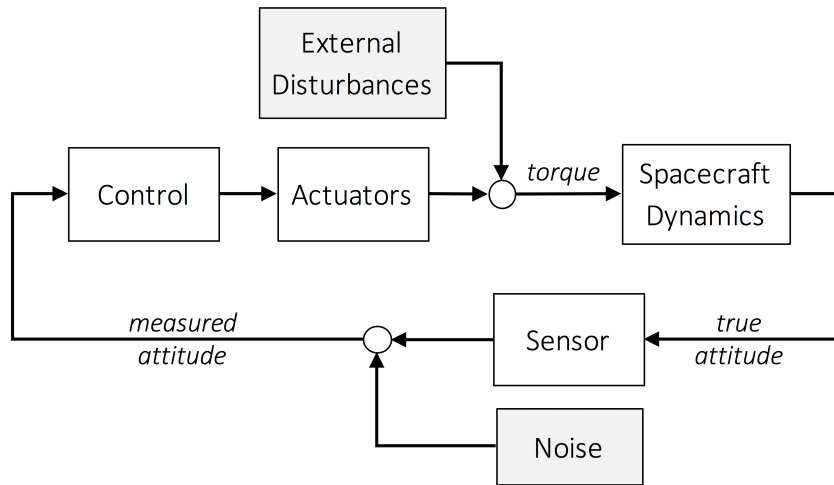


Figure 2.1: Standard spacecraft attitude control subsystem structure

The command is therefore sent to the actuators that generate a control torque. This torque is added to all the disturbance torques acting on the spacecraft, determining the body's angular momentum rate of change $\dot{\mathbf{h}}_{SC}$. The spacecraft dynamic is indeed steered by the *Euler's rotational equation of motion*, that according to [35] can be written as follows:

$$\dot{\mathbf{h}}_{SC} = \sum_i \boldsymbol{\tau}_i = \boldsymbol{\tau}_u + \boldsymbol{\tau}_d \quad (2.1)$$

where $\boldsymbol{\tau}_u$ is the control torque generated by actuators and $\boldsymbol{\tau}_d$ is the sum of all the disturbance torques acting on the spacecraft. As a result, the pointing performance is influenced by exogenous sources of error as the noise introduced by sensors and the external disturbance torques.

Moreover, in reality also actuators are an important source of errors. In a non-ideal case the control torque provided by reaction wheels (RW) is not exactly equal to the one commanded by the controller. According to [12], wheels introduce an inherent torque noise $\tau_{RW,n}$, that is modeled as a colored noise source as well as the sensor noise and the external disturbances. Additionally, as it is going to be explained later in this chapter, flywheels are the origin also of another type of disturbance torque, $\tau_{RW,d}$, which is due to friction instabilities occurring in the ball bearings. As a result, the control torque provided by a RW can be expressed as the sum of the nominal commanded torque, τ_{cmd} , a noise torque and a disturbance torque.

$$\tau_u = \tau_{cmd} + \tau_{RW,n} + \tau_{RW,d} \quad (2.2)$$

This thesis focuses indeed on the characterization of the rightmost term of Equation 2.2, how the pointing-stability performance of the ACS are influenced and how the control system design can be improved to minimize its impact. Further details about the wheel's torque disturbances are provided here below.

2.1.1. Reaction Wheel Assembly Overview

Spacecraft carrying high-resolution scientific instruments require high pointing-stability accuracy during imaging operations. In most of the cases three-axis stabilization is achieved by means of reaction wheels based systems. The reaction torque demanded by the ACS is provided by these mechanisms, as the one illustrated in Figure 2.2, using the momentum exchange principle.

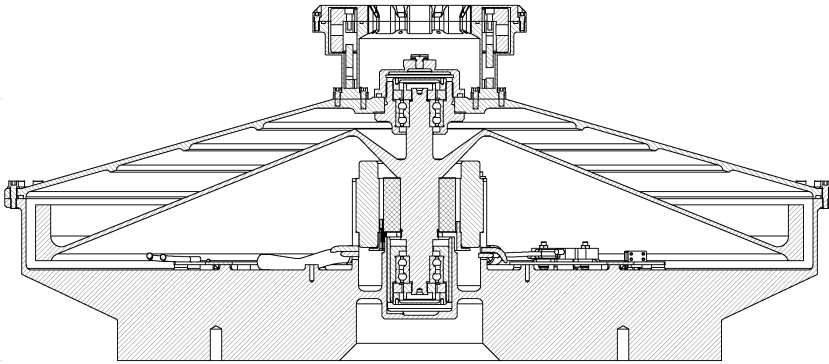


Figure 2.2: Typical reaction wheel assembly design, courtesy of [2]

The reaction torque is produced by accelerating or decelerating the wheel, then the torque applied to the wheel produces an equal and opposite one on the spacecraft. The standard practice for the design of an ACS subsystem is to use three active wheels for momentum exchange management and a fourth inactive wheel as cold redundancy. In the last years this concept has been substituted by the use of four active wheels. The torque practically usable for attitude control is opposite to the flywheel's angular momentum change and it follows the equation:

$$\tau_u = -\mathbf{C}_{r2b}\dot{\mathbf{h}}_{RW} = -\mathbf{C}_{r2b}J_{RW}\dot{\omega}_{RW} \quad (2.3)$$

where \mathbf{C}_{r2b} is the orthogonal rotational matrix relating the wheels' frame with the spacecraft body frame, while J_{RW} is the single wheel spin axis' inertia moment (expressed in $[Kgm^2]$).

The actuator subsystem can be split in three main sub-components: the Reaction Wheel Assembly (RWA), its associated Wheel Drive Electronics (WDE) and a mounting bracket. The RWA, as explained in [26], consists essentially in a high-inertia disk mounted on a bearing housing assembly as illustrated in Figure 2.2. The wheels are usually driven by brushless DC motors that converts into a reaction torque the current input received from the WDE. The RWA is then equipped with sensors such as: tachometers, over-speed and thermal sensors. The WDE, instead, converts the commands coming from the ACS computer into individual wheel currents and, additionally, it relays back telemetry from each wheel. Reaction wheels are the mostly diffused solution on space crafts ACS, however the complexity of such devices is very high, especially the design of the interface between the rotating mass and the internal motor. With this respect, the flywheel inertia is generally supported by robust ball bearings, in order also to withstand launch loads.

2.1.2. Reaction Wheel Disturbances

According to [28], where on-orbit misbehaviors were recorded for satellites launched from 1990 through 2001, anomalies categorized by subsystems showed that the Guidance, Navigation, and Control (GN&C) subsystems

have the highest share of anomalies that resulted in critical mission failures in the last phases of the missions. Among all the GN&C equipment failures, the largest number is attributed to reaction wheels, specifically mechanical wear-out in ball bearings is deemed to be an increasing significant factor. Hence, it is deemed that RW reliability is still a critical issue to be taken into account. For this reason the reaction wheels used in space missions such as SOHO, XMM, Integral and Rosetta were extensively tested, undergoing more than 10 years of qualification test programs, aimed to prove launch survivability and especially operational performances [21]. For 15 years programs the veracity of the lubrication system has been demonstrated to be a great concern and its reliability shall be proven only after very expensive and carefully planned test campaigns.

As a result, the aforementioned complexity of reaction wheels introduces a large amount of anomalies that can occur during their lifetime. In [23], where the most common wheel anomalies encountered are summarized, lubrication appears again to be the major threat for the wheel's bearings lifetime and retainer instability is deemed to be a major cause of bearing failure within a wide class of control actuators such as moment gyroscopes, momentum wheels, and reaction wheels.

Many spacecraft with attitude controlled by reaction wheels had indeed encountered bearing related in-flight anomalies. The wheels of FUSE, TIMED, Hayabusa, and DAWN faced either degradation or failure due to bearing problems. More recently, also the spacecraft Mars Odyssey, Kepler, and the ESA Rosetta have experienced bearing-related anomalies. In this section the lesson learned from the Cassini and XMM-Newton missions are reported and used as a baseline to describe friction disturbance transients.

In-Flight Observations The XMM-Newton [38] was launched in December 1999 and it is the largest X-ray observatory ever launched. The three-axis stabilization of the 3.8 tons bus is accomplished by means of a reaction wheel assembly consisting of 4 wheels, where one is used in cold redundancy.

In summer 2011 anomalies were noticed in the behavior of RW-1, [16]. During SS operations the nominal torque request showed a sudden jump. The spacecraft does not have an on board friction estimator, so there is no direct telemetry of friction, but only for commanded torque. However, an increase in the RW-1 temperature was also observed. This led the team to conclude that there might have been a correlation between the two phenomena. The command torque increment was very likely to be caused by an increase of the friction level, that then heated up the wheel. At the end of the anomalous friction increment, a jump of the torque and current back to nominal values took place. Lately, it was discovered that the problem had started a way long time before, but it was not easy to spot because it was masked by the maneuvers and by the wheel unloading. Cage instabilities were addressed as the most possible cause behind this anomalous behavior.

Furthermore, the same issue was spotted on Cassini. The sophisticated interplanetary spacecraft launched back in 1997 was the first one to achieve orbit at Saturn, in 2004. In this case the three-axis stabilization is achieved by means of three RW's. Moreover, in this case a drag torque estimator was designed to accurately track the physical bearing drag torque only in the steady state, [20]. Additionally, in-flight tests were periodically performed in order to characterize bearing performance of all the wheels, via the so-called coast-down tests. Then, in October 2002, the mission operation team observed anomalous drag torque in the bearings of RW-3. An abrupt step-up of the bearing drag torques followed by an abrupt step-down at an unpredictable time later were noticed from Cassini flight telemetry. The sequence of two steps with different sign is commonly addressed as a *plateau* torque profile and it is illustrated in Figure 1.1. These observations were explained as clear symptoms of bearing cage instabilities. Moreover, another anomalous drag torque signature were observed on the Cassini RWAs. This second class of friction instabilities were characterized by a *spiky* torque profile as depicted in Figure 1.2.

2.1.3. Origins of Disturbance Transients

Bearing cage instability, also called “retainer instability”, is one of the most troublesome failure modes afflicting bearings. Additionally the unpredictable “come and go” nature of the anomaly makes it a great concern.

Bearing retainers rotates circumferentially together with the balls. As a result, as the bearing spins impacts between the cage and the balls occur intermittently. The lack of lubricant at the interface leads to uncontrolled vibrations and erratic torque transients. According to [38], poor lubrication can be due to the following reasons.

- Lubricant starvation: in some cases the cage is made of non-metallic cotton based phenolic material. During the lifetime it might absorb a certain amount of oil, leading to oil starvation.
- Lubricant chemical degradation: as the bearing is lacking of oil, friction increases releasing heat. As the oil runs hotter it starts to degrade further until more complex parts boil off, and eventually it may lead to

bearing failure, [26].

- Lubricant migration: when in the bearing a thermal gradient is created, the oil migrates to colder regions.

While cage instabilities are considered as the principal cause of plateaus-like disturbance transients, drag torque spikes, as the ones observed on Cassini, are most probably related to the *oil jog* phenomena. They consist in a rapid incorporation of a small amount of lubricant by the bearings followed by its relatively slow dispersal. This generates a sudden rise in the drag torque which then dissipates quickly.

It is concluded that a major cause of bearing failures in control moment gyroscopes, momentum and reaction wheels are friction related instabilities such as cage instability and oil jogs. These disturbances occur unpredictably, whereas other are related to a more specific narrow speed range. These phenomena lead to bearings degradation and generate disturbance transients that impair the pointing-stability of the spacecraft. The in-flight observations made within the XMM-Newton and Cassini missions demonstrated that these phenomena can be respectively modeled as plateaus and spikes torque profiles that occur in an unpredictable way. Simplified representations of plateaus and spikes profiles are used in practice during pointing stability analysis campaigns to verify the control system performance, [36]. Worst-case scenario are considered which consists in describing these disturbance transients as deterministic periodic disturbances, where the torque profiles are respectively simplified as rectangular and triangular time-varying functions. Attitude controllers should be able to bear these kinds of disturbances and subsystem requirements are generally formulated with this respect.

2.2. Control Theory

The problem has to be formulated in the common control theory framework. According to [32], the notation commonly used to describe a dynamic system is the one summarized in Figure 2.3. The general configuration can be used to describe a wide class of multi-input/multi-output (MIMO) and single-input/single-output (SISO) systems with a state-space representation. The plant model is represented by P , while K is the system controller. Commands, disturbances and noise are grouped together as *exogenous inputs*, symbolized by w . In the same manner the output signals to be minimized, like the error with respect to the reference or the control effort, are addressed as *exogenous outputs*, whose symbol is z . Then, u is the control signal which is obtained by manipulating the controller input v . The diagram on the right of Figure 2.3 stands for the conventional control configuration commonly used to describe SISO systems. The most relevant parameters are the reference input r , the noise n , disturbances d and the controlled output variable y . It can be demonstrated that the two notations are indeed equivalent when SISO systems are concerned.

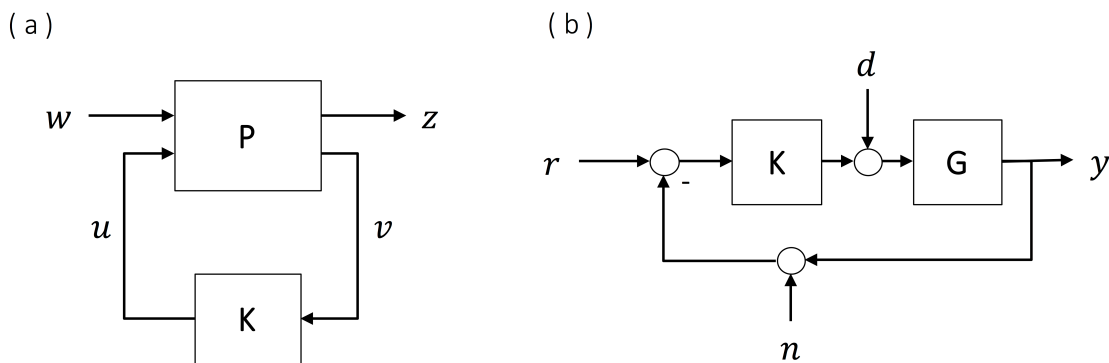


Figure 2.3: Standard notation, according to [32]: general control configuration (a) and one degree-of-freedom control configuration (b)

The starting point for the definition of the control problem can be found in the H_∞ -framework problem formulation provided in [25]. A state-space representation is employed in order to deal with the MIMO nature of the problem. In Figure 2.4 the standard attitude control system, previously introduced in Figure 2.1, is formulated in the general configuration. The input of the generalized plant \tilde{P} are the attitude reference r , the disturbances d and the noise n . The transfer function $G(s)$ represents the plant dynamics (Equation 2.1), in

addition also actuators and sensors dynamics are considered, respectively with $G_A(s)$ and $G_S(s)$. Eventually, $F_{\text{metric}}(s)$ are specific weighting filters to be applied to the absolute attitude error, e , in order to evaluate the different windowed pointing error indices, e_{ind} , that are further discussed in Section 2.4.

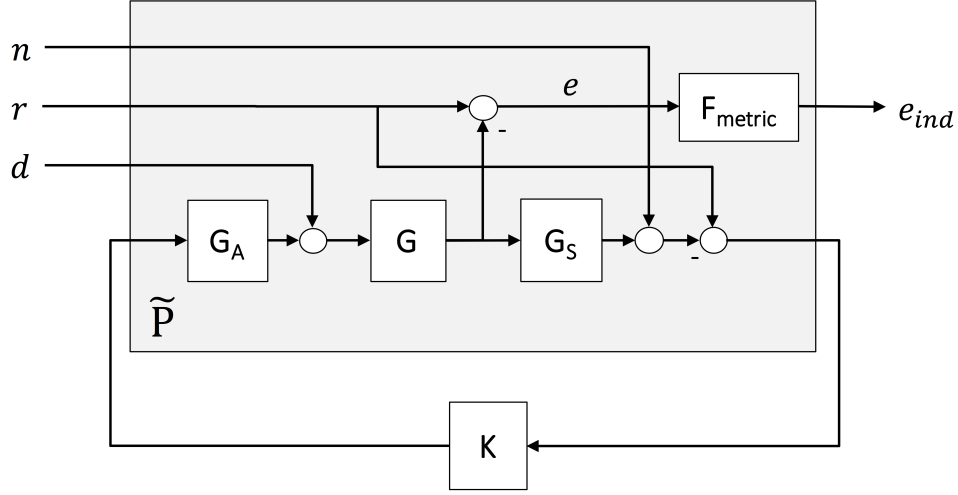


Figure 2.4: Attitude control problem described with the general control configuration

In some cases, the control problem's complexity can be reduced considering the attitude dynamics of the spacecraft decoupled, Equation 2.1 includes indeed some nonlinear coupling terms. According to the control design approach implemented in the 2PCD tool, the attitude dynamic of the three body-axes can be deemed as decoupled. This is a valid assumption firstly because when SS operations are concerned the cross-coupling nonlinear terms in Equation 2.1 can be neglected, they become significant only when large and fast angular maneuver are required, [33]. Additionally, according to [19] the attitude dynamic can be considered decoupled if the spacecraft's principle axes are very closely aligned with the mechanical axes. This is a common approach employed during controller synthesis phases, that can be later verified running simulations with the complete nonlinear plant. The attitude control system can be then described as a SISO system. Hence, the state-space representation of Figure 2.4 can be translated into the one degree-of-freedom configuration, as illustrated in Figure 2.5, where the dynamic of a generic attitude angle ϕ is considered.

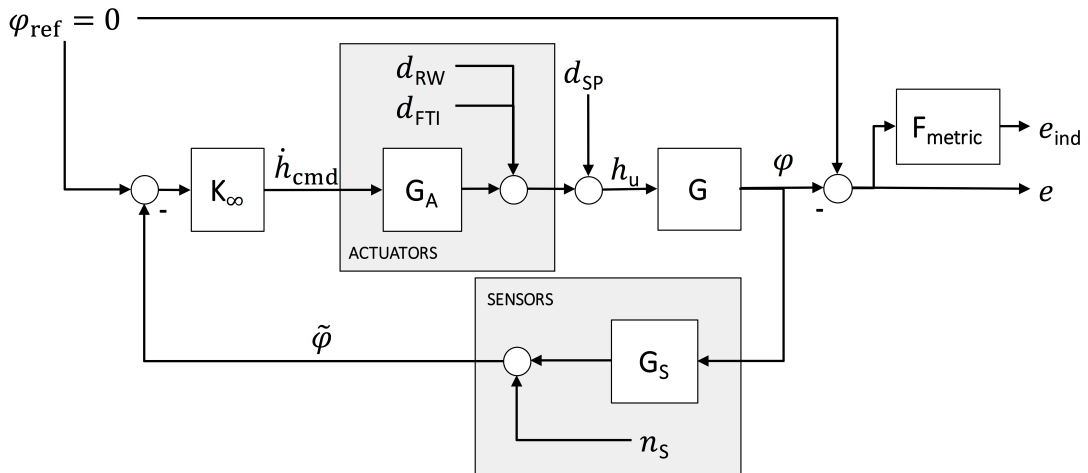


Figure 2.5: Attitude control problem described with the one degree-of-freedom control configuration

The controller K_∞ is the one obtained through the 2PCD tool, which is the starting point of the analysis. According to the design tool the output of the controller is a control torque normalized with respect to the spacecraft

inertia about the axis considered, it is hence expressed in [rad/s²] and therefore addressed as a commanded angular momentum rate, \dot{h}_{cmd} .

The reference pointing error sources considered in the 2PCD frame are measurement noise n_s , RW torque noise d_{RW} (internal disturbance) and solar pressure torque noise d_{SP} (external disturbance) and they are here addressed as *reference noise PES's*, in order to be distinguished by the disturbance transients d_{FTI} that are the focus of this thesis. The index *FTI* is motivated by the fact that these disturbances are due to friction torque instabilities generated in the RWA. All torque disturbances are then normalized with respect to the spacecraft moment of inertia.

Controller design has two main objectives: to achieve system stability and to improve performance. None of the two can be overlooked during the synthesis of a controller. As a result, in the analysis carried out in the next chapters both stability and performance are taken into account when different control solutions are analyzed. In the following two subsections, basic considerations about closed-loop performance and stability, applied to a SISO system, are therefore reviewed.

2.2.1. Closed-Loop Stability

Stability is a critical issue in designing a controller. Achieving high performance would indeed become purposeless if the dynamic system is unstable. According to [32], two methods are commonly used to determine whether the system is stable or not.

First method consists in the evaluation of the poles of the closed-loop system. Then the system is stable *if and only if* all the closed-loop poles are in the open left half-plane. In the case at issue the closed-loop transfer function can be easily derived from Figure 2.5.

$$H_{\text{CL}}(s) = \frac{\phi}{\phi_{\text{ref}}} = \frac{KG_A G}{1 + KG_A GG_S} \quad (2.4)$$

The second method regards, instead, the frequency response of the open-loop transfer function $L(s)$. Bode's stability condition can be then applied, which says that the closed-loop system is stable *if and only if* the open-loop gain $|L(s)|$ is less than 1 at the frequency where its phase crosses -180° . According to the system described in Figure 2.5 the open-loop transfer function is expressed as follows:

$$L(s) = KG_A G \quad (2.5)$$

However, in this way sensor dynamics do not have any influence on the system stability. This method applies when a unitary feedback gain is considered, as a result, when sensor dynamics are introduced in the feedback loop, according to [32] the open-loop system transfer function has to be written as follows:

$$L'(s) = KG_A GG_S \quad (2.6)$$

Sensitivity and complementary sensitivity functions can be then derived according to the respective definitions.

$$S'(s) = \frac{1}{1 + L'} \quad , \quad T'(s) = \frac{L'}{1 + L'} \quad (2.7)$$

The first method is well suited for numerical calculations, but time delays must be approximated by means of rational approximation. Whereas, the second method provides also useful measures of *relative stability*, i.e. how close the system is to instability. As a result, while the evaluation of closed-loop poles is going to be used to quickly check the stability of a given controller, gain margin (GM) and phase margin (PM), as defined in [32], are going to be evaluated in order to determine "how stable" the system is when different control solutions are implemented in the loop. Safe stability margins are generally guaranteed when GM > 6 dB and PM > 30 deg.

2.2.2. Closed-Loop Performance

Next to stability, the real purpose of control is to improve performance. With this respect, however, different performance objectives can be determined, as explained in [32].

One of the aims is to improve the reference tracking performance of the system, that for high precision pointing mission is an high priority requirement, at least during steady-state operations. To achieve this, the complementary sensitivity function $T(s)$ magnitude should be as close as possible to 1, in the frequency range of interest. In this way, also noise rejection is accomplished in the frequency range where $T(s)$ drops to 0. On the other hand, disturbance rejection is another objective that can be of high interest. To achieve this, instead, the

sensitivity function $S(s)$ magnitude should be as close as possible to 0, in the frequency range where disturbances have to be suppressed. These two performance objectives lead to the classic trade-off between noise and disturbance rejection, as it is extensively discussed in [32].

As far as the attitude control problem is regarded, pointing performance are evaluated by means of a set of statistical indices that are later on described in Section 2.4. Time-domain performance, as the peak values of the time response, are not considered in this analysis, even though they are important when specific payloads are regarded.

Then, if interest is pointed towards disturbance rejection, the transfer function to be analyzed is the one from the generic disturbance source d to the output pointing error e . According to the system depicted in Figure 2.5 it can be expressed as follows:

$$H_d(s) = \frac{e}{d} = -\frac{G}{1 + G_A K G_S G} = -\frac{G}{1 + L'} = -G S' \quad (2.8)$$

Also the impact of measurements noise on the absolute pointing error is going to be taken into account for the controller design, then the transfer function from n_S to e can be calculated as follows:

$$H_n(s) = \frac{e}{n_S} = \frac{G_A K G}{1 + G_A K G_S G} = \frac{G_A K G}{1 + L'} \quad (2.9)$$

For a standard SISO control problem as the one depicted in the right hand-side diagram of Figure 2.3, the noise transmission is driven by the complementary sensitivity function. In this case, where sensors' dynamic is also included, it can be observed that:

$$H_n(s) = \frac{G_A K G}{1 + L'} = \frac{T'}{G_S} \quad (2.10)$$

The most common way to assess disturbance and noise rejection performance is the *maximum peak criteria*, [32], which consists in evaluating the infinity norm of the sensitivity and complementary sensitivity functions.

$$M_S = \|S'(s)\|_\infty = \max_\omega |S'(j\omega)|, \quad M_T = \|T'(s)\|_\infty = \max_\omega |T'(j\omega)| \quad (2.11)$$

Commonly, as mentioned in [32] and [25], the two peak parameters M_S and M_T should be limited by a value of 6 dB. A large value of M_S or M_T indicates not only poor performances but also poor stability robustness. In practice there is a close relationship between these maximum peaks and the previously introduced GM and PM (mathematical justifications can be found in [32]).

In conclusion, among the thesis pointing error indices are going to be the main criteria used in the control design synthesis to optimize performances, however, both the maximum peaks, M_S and M_T and the margins, GM and PM, are going to be taken into account to assess the stability robustness.

2.3. Fourier Analysis

In order to address the problem in the frequency domain, Fourier analysis is applied. This branch of mathematics, also called *harmonic analysis*, concerns with the representation of functions or signals as the superposition of basic waves and it was disclosed in the 1807 paper *Mémoire sur la propagation de la chaleur dans les corps solides* by Joseph Fourier.

The basics of Fourier analysis are hereby presented and formulas and theorem are referring to any real-valued time domain signal $x(t)$ of a generic units of measurements [A]. In the following, the Fourier synthesis process is described for both periodic and aperiodic signals, since the representations of such signals in the frequency domain and the derivations are different.

2.3.1. Aperiodic Signal Analysis

Signals that do not show any periodicity can be represented in the frequency domain by a continuous spectrum, that is called *Fourier transform*. The necessary conditions to be fulfilled for the existence of the Fourier transform of a signal are the Dirichelet conditions, as described in [1] and [37]. In particular, the signal should verify the absolute integrability condition.

$$\int_{-\infty}^{\infty} |x(t)| dt < \infty \quad (2.12)$$

Then, the Fourier transform can be defined as:

$$\mathcal{F}\{x(t)\} = X(\omega) = \int_{-\infty}^{\infty} x(t) e^{-j\omega t} dt \quad (2.13)$$

The complex function obtained is the *two-sided spectral density* of the signal $x(t)$ and it can be rewritten in terms of magnitude and phase shift. Its units are [A/Hz].

$$X(\omega) = |X(\omega)| e^{j\theta(\omega)} \quad (2.14)$$

The function $X(\omega)$ gives the representation of the original signal in terms of an infinite sum of complex exponentials each weighted by $|X(\omega)| d\omega$.

When the magnitude of the Fourier transform is plotted against the frequency, the *magnitude spectrum* is obtained (also called *amplitude spectrum*). It is referred as *one-sided spectrum* when only the positive frequency domain is considered.

Energy Signal

Furthermore, the energy content of the signal can be analyzed by calculating the square of the spectral density $X(\omega)$. The quantity $|X(\omega)|^2$ is indeed called *energy spectral density*, E_x , with units [A²/Hz²].

If the signal is also *square integrable*, meaning that it has a finite normalized energy, it holds

$$E_x = \int_{-\infty}^{\infty} |x(t)|^2 dt < \infty \quad (2.15)$$

The Parseval's theorem can be then applied. According to it, the integral of the energy spectral density over the whole frequency domain equals the normalized energy of the signal, as computed in the time domain.

$$E_x = \int_{-\infty}^{\infty} |x(t)|^2 dt = \frac{1}{2\pi} \int_{-\infty}^{\infty} |X(\omega)|^2 d\omega = \int_{-\infty}^{\infty} |X(f)|^2 df \quad (2.16)$$

Note: The integrability of the signal necessary to define the Fourier transform is not sufficient for the validity of the Parseval's formula, as the finiteness of the integral in Equation 2.12 does not imply that the signal has finite energy E_x (and, vice versa, finiteness of E_x does not imply the absolute integrability of the signal).

2.3.2. Periodic Signal Analysis

A time-domain signal $x(t)$ is a periodic signal, and usually addressed as *period waveform* of period T_p , if it holds:

$$x(t + T_p) = x(t), \quad \forall t \in [-\infty, +\infty] \quad (2.17)$$

Periodic signals are not absolute integrable, for this reason the Fourier transform cannot be formally applied but another tool needs to be introduced. According to harmonic analysis a complex-valued signal $x(t)$ that is periodic with period T_p can be written in the form of an infinite complex *Fourier series*.

$$x(t) = \sum_{k=-\infty}^{+\infty} z_x(k) e^{-jk\omega_0 t} \quad (2.18)$$

Let the fundamental harmonic ω_0 be $\omega_0 = 2\pi/T_p$ expressed in [rad/s], or $f_0 = 1/T_p$ in [Hz], then the Fourier coefficients are determined as follows:

$$z_x(k) = \frac{1}{T_p} \int_{-T_p/2}^{T_p/2} x(t) e^{-jk\omega_0 t} dt \quad (2.19)$$

The convergence of the Fourier series is guaranteed if the Dirichlet conditions, mentioned before, are met, once expressed in a slightly different manner. The absolute integrability condition in this case has to be verified over a single period.

Power Signal

When periodic signals are addressed, the Parseval's relationship mentioned in the previous section applies to the computation of the average power of the signal instead of the normalized energy. According to [37], the Parseval's theorem can be translated as follows:

$$P_x = \frac{1}{T_p} \int_{-T_p/2}^{T_p/2} |x(t)|^2 dt = \sum_{k=-\infty}^{+\infty} |z_x(k)|^2 \quad (2.20)$$

The squared magnitude of the Fourier coefficient, when plotted against the respective frequency harmonics, produces the so-called *power spectrum* (unit of $[A^2]$). Hence, the power of a period waveform can be easily calculated in the frequency by the sum of all the Fourier coefficients squared.

2.4. Pointing Error Indices

High precision pointing missions impose requirements not only on the instantaneous pointing error at a given moment of time, but also on the properties of the error profile during specific time intervals and time-windows, e.g. the time length over which an image is integrated.

The Pointing Error Engineering Handbook [11] and the ECSS Control Performance Standard [10] provide specifications and solid definitions of pointing errors and their analysis. Previously, only two method were usually used to assess pointing stability: the *peak-to-peak* method and the *rms* method, as defined in [27]. The second one was indeed used in [29], [22] and [15] to define and analyze the pointing-stability requirements of the line-of-sight (LOS) vector of an on-board instrument. Nevertheless, for high precision missions, where pointing stability is crucial, a systematic method to describe and assess it is required. According to [6], the frequency domain techniques introduced by this novel framework are necessary to reduce uncertainties in pointing error budget.

In the following sections the standard tools provided by [11] for error sources' characterization are briefly described. In addition, in Section 2.4.4 the pointing error analysis methodology, used as a reference in the thesis, is presented.

2.4.1. Stochastic Measures

According to [1], stationary random processes, given the time history $x(t)$, can be described in the time domain using the established stochastic measures that are summarized in the Table 2.1.

Parameter	Definition
Mean value	$\mu_x = E[x]$
Mean square value	$\psi_x^2 = E[x^2]$
Variance	$\sigma_x^2 = E[(x - \mu_x)^2]$

Table 2.1: Stochastic measures definition for a stationary random noise process

The signal average power has an important meaning from a statistical point of view. It is indeed equal to the mean square value ψ^2 of the signal, while for zero-mean signals it corresponds also to the signal variance σ^2 .

$$P_x = \lim_{T \rightarrow \infty} \frac{1}{T} \int_0^T |x(t)|^2 dt = \psi_x^2 = \sigma_x^2 + \mu_x^2 \quad (2.21)$$

In [10], [11] and [12] the *power spectral density* (PSD) formalism is introduced in order to describe pointing error sources in the frequency domain. It is usually denoted as $S_{xx}(\omega)$ and its definition can be found in [1]. The area under a random process's PSD is equal to its mean square value, which in turn equals the noise's variance, for zero-mean random processes.

$$\psi_x^2 = \sigma_x^2 + \mu_x^2 = \frac{1}{2\pi} \int_{-\infty}^{\infty} S_{xx}(\omega) d\omega = \int_{-\infty}^{\infty} S_{xx}(f) df \quad (2.22)$$

In [1] it is defined both as a double-sided PSD, $S_{xx}(\omega)$, for frequencies $f = (-\infty, \infty)$ or as a single-sided PSD,

$G_{xx}(\omega)$, for non-negative frequencies. The latter definition is the more used for practical applications.

$$G_{xx}(\omega) = \begin{cases} S_{xx}(0) & \text{if } \omega = 0 \\ 2S_{xx}(\omega) & \text{otherwise} \end{cases} \quad (2.23)$$

This formalism is very useful in order to describe the frequency domain characteristics of a stationary random process. Additionally, it can be used to study how a random process is propagated through a system, as illustrated in Figure 2.6. The spectral distribution of the input signal's power is modified depending on the transfer characteristics of the system that can have different impacts depending on the frequency range. According to Equation 2.22 the area underneath the PSD is equivalent to the signal's average power then it can be said that the design of a controller consists in specifically shaping the transfer characteristics of the system with respect to different error sources (inputs) to minimize the average power of the different pointing error indices (outputs).

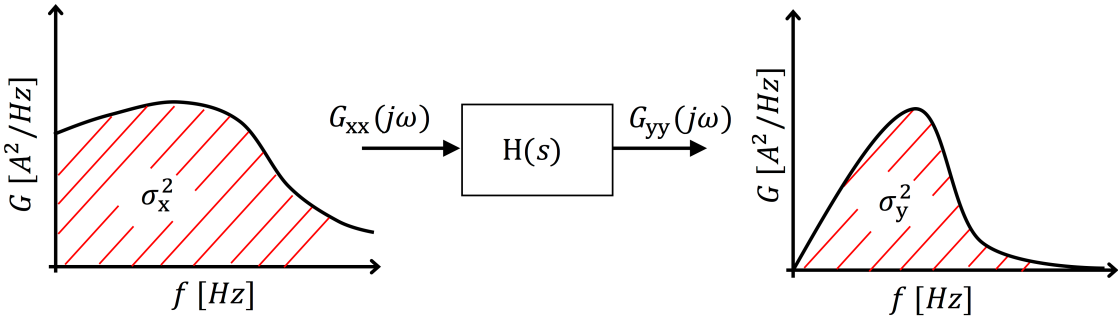


Figure 2.6: Propagation of the error sources' power spectral density through a linear time-invariant system

Given a linear, time-invariant (LTI) system, the *input/output auto-spectrum relation* can be applied, according to [1] and [5].

$$\mathbf{G}_{yy}(\omega) = \mathbf{H}(j\omega)\mathbf{G}_{xx}(\omega)\mathbf{H}^*(j\omega) \quad (2.24)$$

with $\mathbf{H}(j\omega)$ being the transfer matrix, e.g. an attitude control system, and \mathbf{G}_{yy} the output PSD's vector. Whereas for SISO systems Equation 2.24 can be reworked as follows:

$$G_{yy}(\omega) = |H(j\omega)|^2 G_{xx}(\omega) \quad (2.25)$$

with $H(j\omega)$ being the transfer function between the input signal x and the output signal y .

2.4.2. Time Domain Description

In practice, as stated in [10], also pointing errors defined over time windows are important and also the relation of those windowed errors with respect to each other. The approach provided in [11] is hereby applied to the spacecraft attitude control problem, in this case the pointing performance parameters considered are the angles describing the spacecraft attitude. Different time-dependencies are addressed in [10] and the Pointing Error Indices (PEI) related to them are described here below.

- **Instantaneous time t :** pointing error at any point in time t during system lifetime. Pointing performances are evaluated by means of the Absolute Performance Error (APE), which consists in the difference between the target attitude and the actual one.
- **Window time Δt_w :** pointing error within a time window Δt_w , whereas the time window can occur at any point in time t during system lifetime. Pointing performances are evaluated by means of the Mean Performance Error (MPE) and Relative Performance Error (RPE). The first one consists in the mean value of the APE over a specified time interval Δt_w . The second one consists in the difference between the APE at a given time within a time interval, Δt_w , and the MPE over the same time interval.
- **Stability time Δt_{sta} :** pointing error describing stability, thus the relative error, among pointing errors in time-windows of length Δt_w . The time-windows are separated by a time difference of length Δt_{sta} , and

can occur at any point in time t during system lifetime. Pointing performances are evaluated by means of the Performance Drift Error (PDE) which consists in the difference between MPEs taken over two time intervals separated by a specified time, Δt_{sta} .

Let $e(t)$ be the instantaneous pointing error over an observation period, the time dependencies above introduced are furthermore graphically illustrated in Figure 2.7. MPE and RPE regard a single time-window of length Δt_w , while the stability index PDE considers two time-windows with the same length Δt_w separated by Δt_{sta} .

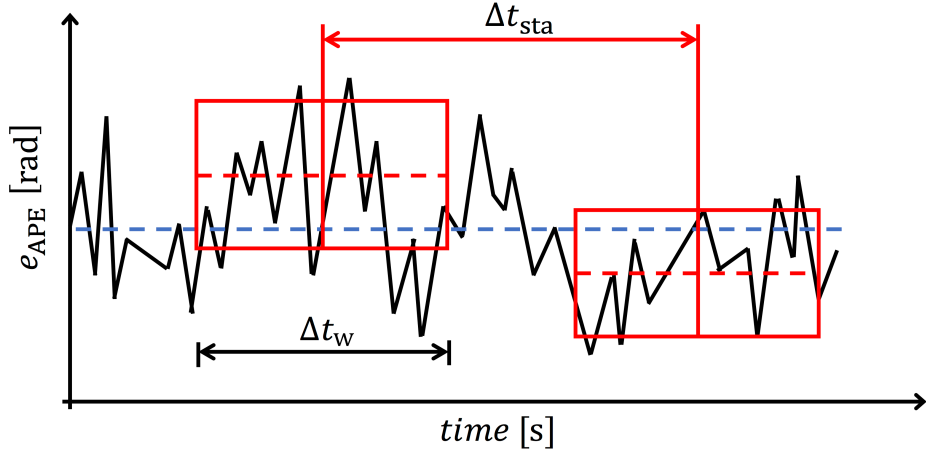


Figure 2.7: Time dependencies of the various pointing errors

In the guidelines provided by [11], the different error indices are addressed in terms of their variance, since it is a direct indicator of the power content of the error signal. Hence, they can be derived in the time domain according to the metrics listed in Table 2.2, to be applied to the absolute pointing error time-series $e(t)$.

Index	Time-domain Metric
σ_{APE}^2	$= \text{E}[(e(t) - \mu_e)^2]$
$\sigma_{\text{MPE}}^2(\Delta t_w)$	$= \text{E}[(\langle e(t) \rangle_{\Delta t_w} - \mu_e)^2]$
$\sigma_{\text{RPE}}^2(\Delta t_w)$	$= \text{E}\left[\left\langle (e(t) - \langle e(t) \rangle_{\Delta t_w})^2 \right\rangle_{\Delta t_w}\right]$
$\sigma_{\text{PDE}}^2(\Delta t_w, \Delta t_{\text{sta}})$	$= \text{E}\left[\left(\langle e(t) \rangle_{\Delta t_w} - \langle e(t - \Delta t_{\text{sta}}) \rangle_{\Delta t_w}\right)^2\right]$

Table 2.2: Time-domain metrics definitions of the performance error indices, according to [11]

It has to be highlighted that the RPE hereby defined in the Pointing Error Engineering framework is equivalent to the *rms* pointing stability as it was addressed before the topic was investigated systematically by [11]. Therefore in the following analysis the RPE is deemed to be the pointing error index of major interest. It is indeed representing the signal stability over a specific time-window, that for science space applications can be represented by the observation time required by the payload instrumentation to perform a measurement.

2.4.3. Frequency Domain Description

These pointing error indices introduced here above can also be addressed in the frequency domain. The different pointing errors are commonly modeled as zero-mean stationary random processes, and according to [11] the PSD formalism can be used to analyze them in the pointing error engineering framework. In steady-state operations the absolute pointing error is indeed supposed to be zero-mean if the controller has been designed properly, as a result the variance of the different errors can be also evaluated through the integral of the PSD, according to Equation 2.22. Therefore, given the PSD of the absolute attitude error index G_{ee} , considering

time-windowed errors in the frequency domain is equivalent to regarding a weighted PSD. Hence, the different pointing error indices can be calculated as described in Table 2.3.

Index	Frequency-domain Metric
σ_{APE}^2	$= \int_0^\infty G_{ee}(f) df$
$\sigma_{MPE}^2(\Delta t_w)$	$= \int_0^\infty G_{ee}(f) F_{WM}(f) df$
$\sigma_{RPE}^2(\Delta t_w)$	$= \int_0^\infty G_{ee}(f) F_{WV}(f) df$
$\sigma_{PDE}^2(\Delta t_w, \Delta t_{sta})$	$= \int_0^\infty G_{ee}(f) F_{WMS}(f) df$

Table 2.3: Frequency-domain metrics definitions of the performance error indices, according to [11]

The weighting filters to be applied correspond to either low-pass or high-pass filtering. Their definitions together with rational approximations are provided in Figure 2.8.

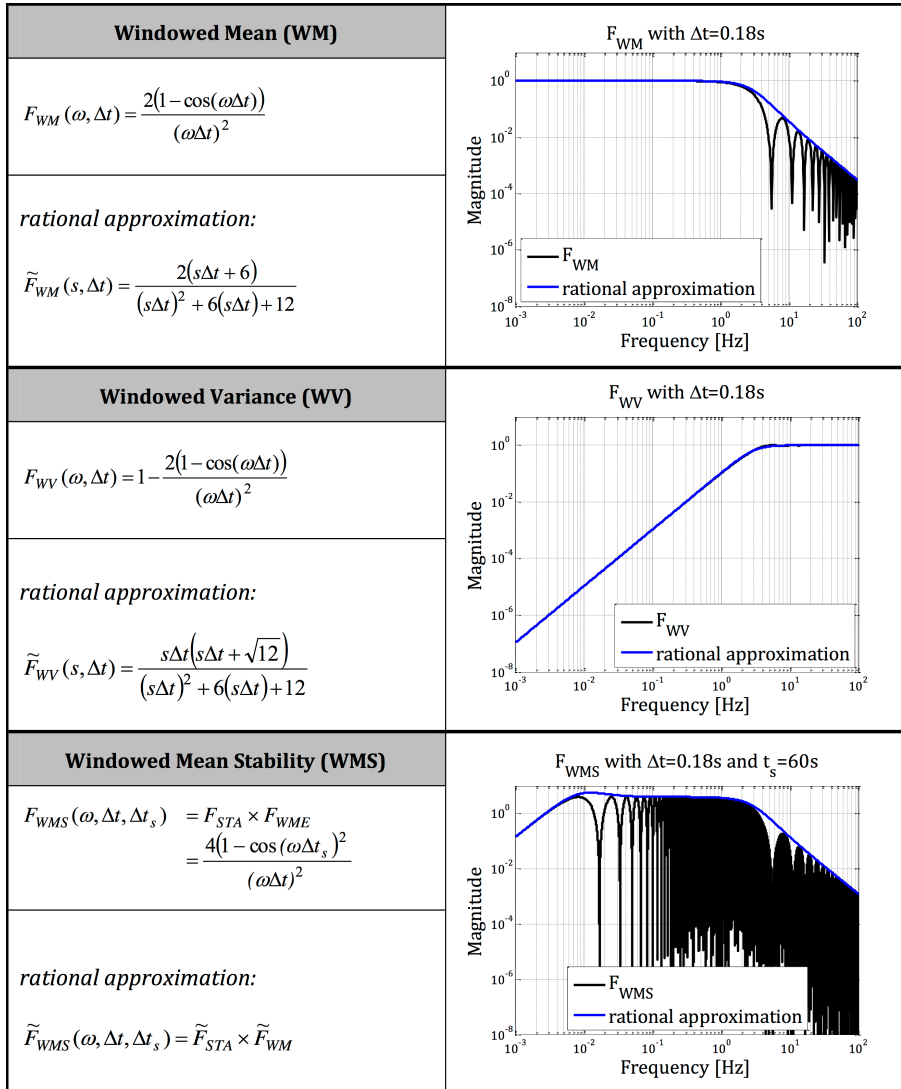


Figure 2.8: Frequency-domain weighting filter definitions of the various time-dependencies errors, according to [11]

The rational approximations are provided since they can easily be implemented in numerical simulations,

however it has to be highlighted the fact that the rational approximations of the Windowed Mean (WM) and Windowed Meas Stability (WMS) filters are not accurate in certain frequency range. As it can be observed in the graphical illustrations where the weighting filters and their approximations are compared, the signal's power is over-estimated if the latter are considered in the analysis, this specifically holds for the MPE and PDE indices. As a result, according to standards defined in [11], the performance indices can be derived both from the pointing error time series and from frequency domain analysis. However, according to [11], the use of PSD to describe pointing error sources and perform pointing error budgets is the approach to be preferred for very detailed analysis. Hence, when the attitude control problem is considered, the frequency domain approach is recommended for high-precision pointing missions and in the final phases of the ACS design.

2.4.4. Pointing Error Analysis

Within this framework a Pointing Error Engineering methodology is formulated in [11], and specifically applied to the spacecraft attitude control subsystem design and performance's assessment, [5]. This is the reference with respect to which the design of the controller and the evaluation of pointing performance are carried out within this thesis, therefore the guidelines provided in [11] are hereby briefly described. The approach is illustrated in Figure 2.9 and the main analysis step (AST) are briefly described in the following.

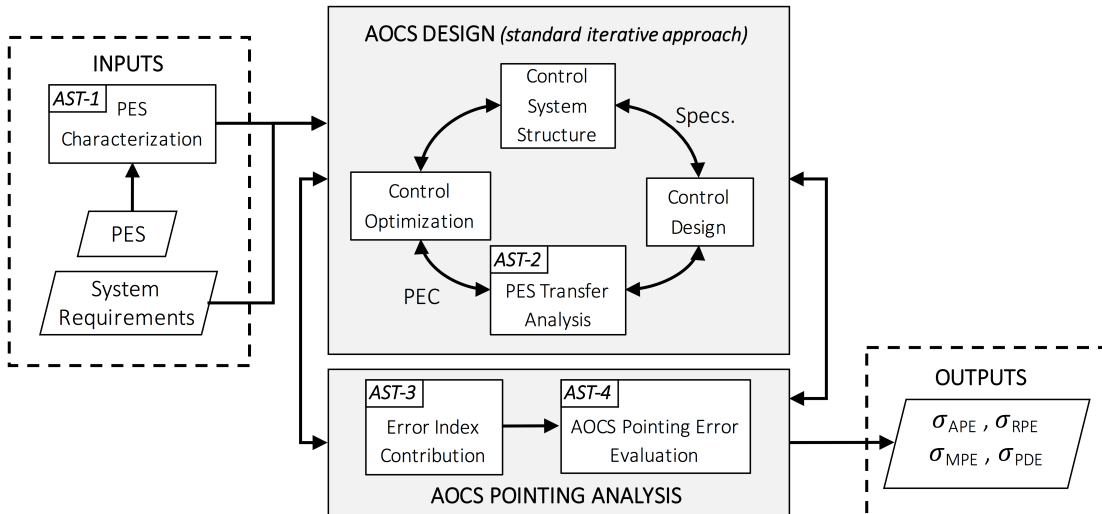


Figure 2.9: Standard control design approach within the pointing error engineering framework, as provided by [11]

The process starts with the identification and characterization of the different PES's in **AST-1**. Afterwards, the design of the controller follows and, with this respect, the standard iterative approach is addressed. PES transfer analysis, **AST-2**, consists in evaluating how the different error sources impact the pointing error. The various Pointing Error Contributors (PEC) are hence obtained, depending on the system transfer characteristics at issue, as graphically explained in Figure 2.6. When an ACS problem is considered, the controller design consists in the iterative tuning of the closed-loop system's transfer characteristics in order to fulfill the pointing performance requirements. Eventually, the contribution of the PES's to the pointing error indices is elaborated in **AST-3** and the absolute and different time-windowed pointing error contributors are compiled to obtain an estimate of the overall pointing error in **AST-4**.

The pointing error analysis methodology hereby introduced is adapted to the available PES data and tools as the pointing system design matures. Provided with a LTI system, a frequency domain approach can be used to analyze characteristic error properties and then perform the transfer analysis to evaluate their contributions to the different pointing error indices (APE, MPE, RPE, PDE).

As already mentioned before, two different methods are provided: a simplified statistical method and an advanced statistical method. For the performance analysis of high-precision pointing space mission the second method is to be employed, and it consists in handling the different PES's through the power spectral density formalism introduced here above. However, as far as the advanced method is concerned, it has to be stressed that only stationary random processes and sinusoidal periodic waves are addressed as pointing error sources.

The mathematical tools required to address specific transient processes, like plateaus and spikes disturbances, are not regarded in [11]. Motivated by the approach here above discussed a similar mathematical formalism to model disturbance transients as statistical pointing error sources is presented in the next chapter.

3

Parametric Pointing Performance Estimation

In Section 1.2 the thesis objective is introduced, and it has been explained why the need for an analytical tool to characterize friction torque instabilities in the frequency domain is essential. In order to properly investigate how the rejection capabilities of control system can be improved, the disturbances at issue have indeed to be specifically characterized.

In Section 3.1, following the approach suggested in the pointing error engineering framework [11], a pseudo-PSD formalism is derived to describe disturbance transient signals in the frequency domain. The derivations are performed with respect to a general deterministic waveform. In this way, a powerful mathematical tool, that can be later exploited to optimize the control system with respect to friction torque instabilities is provided. By means of it, in addition, PES transfer analysis can be performed according to [11] in order to evaluate the impact of disturbance transients on the system pointing performance. Later in Section 3.2 the formalism is specifically applied to the wheels disturbance transients and an expression of plateaus and spikes torque profiles' pseudo-PSD is obtained. Hence parametric expressions of the different PEC's are formulated in order to analyze how the disturbance torque profiles' characteristics can influence the overall pointing-stability performance.

Before proceeding, the mathematical tools are verified comparing the analytical estimation with numerical simulations. This is done in Section 3.2, where a pointing error evaluation is conducted within the reference case study. In Figure 3.1 these steps are graphically illustrated in order to highlight the needs that led to this analysis and how the output tools are essential to approach the following step of the thesis.

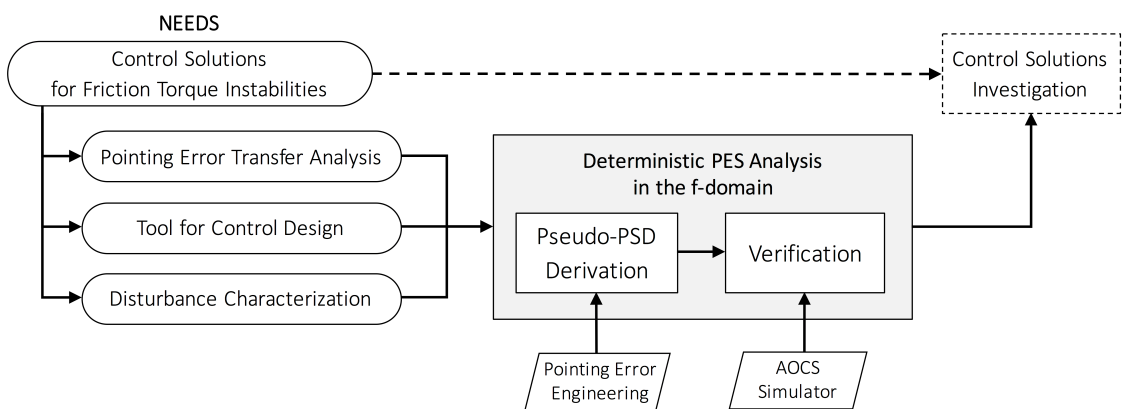


Figure 3.1: Overview of the third chapter's contents

3.1. Frequency Domain Analysis of Disturbance Transients

In order to address in the frequency domain friction torque instabilities generated by RW's, the torque profiles have to be firstly characterized in the time domain, this is done in Section 3.1.1. Then, a pseudo-PSD formalism is derived in Section 3.1.2 for a general case of a deterministic periodic signal.

3.1.1. Signal Characterization

In Chapter 1 it has been showed that plateaus and spikes torque disturbances occurring due to ball bearings misbehaviors are still lacking of a detailed description of the physical phenomena that drive them. Their occurrence and the torque level characteristics have been so far deemed to be unpredictable. Such disturbances have not yet been considered in the control system design phase, nevertheless they were taken into account in [36] in order to carry out a pointing stability analysis, aimed to verify whether the controller designed for the Euclid mission was capable of dealing with such additional disturbances. In the latter case, according to the mission requirements, such disturbances were addressed in a worst-case scenario. Plateaus have been modeled as periodically occurring rectangular profiles, while spikes were approximated by periodic triangular profiles as they were also regarded in [20] and [36].

Since the mathematical tool hereby presented is intended to be employed in the design process of the control system, plateaus and spikes torque profiles are going to be addressed in the same worst-case scenario according to [36], the characteristics of the time-domain functions used are listed in Table A.3. Employing worst-case disturbance and noise models in the design phase of the control system is indeed common practice to guarantee safety margins, at least in the preliminary analysis. As a result, the disturbance torque profiles hereby considered consist in a series of plateaus or spikes, respectively modeled as periodically occurring rectangular and triangular functions, as illustrated in Figure 3.2 and 3.3. A rectangular function is used to represent a plateaus disturbance, while a triangular function describes a spike profile with good approximation.

Even though in reality these disturbances occur randomly during the last phases of a RW's lifetime, for as far as the worst-case scenario is regarded, according to the classification provided in [1] these disturbance signals can be deemed as *deterministic* because the torque profiles can be described by a mathematical function. Moreover, they belong to the class of *complex periodic data*, that according to [1] are signals defined mathematically by a time-varying function whose waveform exactly repeats itself at regular intervals.

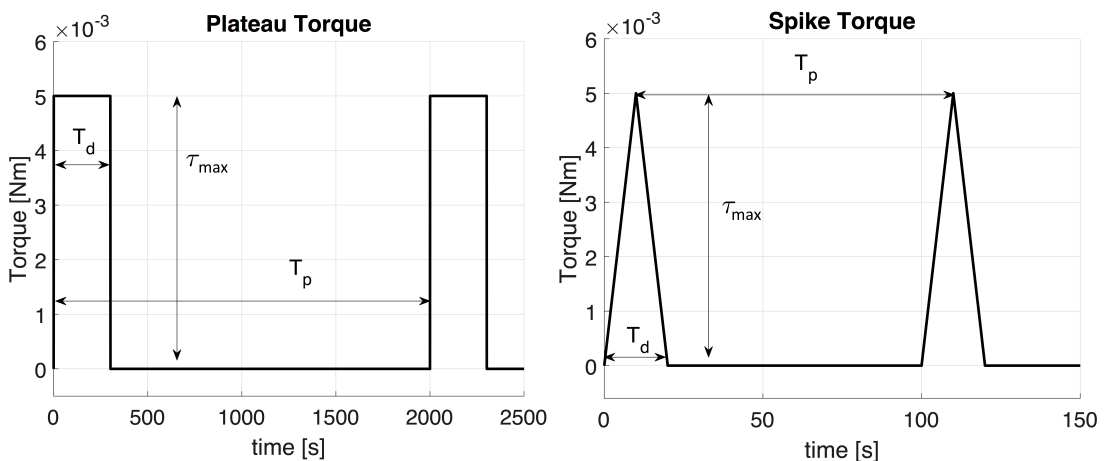


Figure 3.2: Profile of periodic plateaus torque instabilities in Figure 3.3: Profile of periodic spikes torque instabilities in the time domain

The rectangular and triangular waveforms can be indeed described mathematically as explained in the following. Let $b_0(t)$ be the function describing a single plateau centered at the time instant t_0 , while $b(t)$ the one describing a periodic series of plateaus. The relevant parameters that are necessary to determine uniquely the rectangular waveform are illustrated in Figure 3.2. Accordingly, a single rectangular profile is defined in the time domain as follows:

$$b_0(t) = \begin{cases} \tau_{\max} & \text{if } t_0 - \frac{T_d}{2} < t < t_0 + \frac{T_d}{2} \\ 0 & \text{otherwise} \end{cases} \quad (3.1)$$

Then, the rectangular waveform $b(t)$ can be determined by summing multiple shifted single-box functions.

$$b(t) = \sum_{k=-\infty}^{\infty} b_0(t - kT_p) \quad k = 1, 2, \dots \quad (3.2)$$

Then spike torque profiles can be regarded in the same manner. Let $p_0(t)$ be the function describing a single triangular spike centered at the time instant t_0 , while $p(t)$ the one describing a periodic series of spikes. Then, according to the nomenclature provided in Figure 3.3, a single triangular profile can be described in the time domain as follows:

$$p_0(t) = \begin{cases} \tau_{\max} \left(1 - \frac{2|t|}{T_d}\right) & \text{if } |t| < \frac{T_d}{2} \\ 0 & \text{otherwise} \end{cases} \quad (3.3)$$

Then, the periodic triangular waveform $p(t)$ can be determined by summing multiple shifted single-triangle functions.

$$p(t) = \sum_{k=-\infty}^{\infty} p_0(t - kT_p) \quad k = 1, 2, \dots \quad (3.4)$$

3.1.2. Derivation of the Pseudo-Power Spectral Density Formalism

According to the considerations made in Section 2.3, a period waveform does not have a Fourier transform in the usual sense of the word because it is not a finite-energy signal. What it does have is a Fourier series representation and this is also the case for deterministic complex periodic signals as stated in [1]. For this reason, a proper spectral density function cannot be derived for a deterministic periodic signal, thus the same reasoning cannot be extended to this class of data. Nevertheless a pseudo-PSD formalism is hereby defined, where the starting point of the derivations is the definition of average power. In order to make the analysis as more general as possible, let assume $x_0(t)$ to be a time-varying function defined over a single period T_p and $x(t)$ the periodic function obtained by repeating $x_0(t)$ indefinitely with the same time period T_p . According to [1], the average power of a periodic signal $x(t)$ can be calculated in the time domain only considering a single period.

$$P_x = \lim_{T \rightarrow \infty} \frac{1}{T} \int_0^T |x(t)|^2 dt = \frac{1}{T_p} \int_0^{T_p} |x_0(t)|^2 dt \quad (3.5)$$

Let then $X_0(f)$ be the Fourier transform of $x_0(t)$, after some further algebraic calculations reported in Annex B.1, it can be showed that:

$$P_x = \int_{-\infty}^{\infty} \frac{|X_0(f)|^2}{T_p} df \quad (3.6)$$

As a result, the average power of a deterministic periodic signal can be also evaluated computing the integral over the whole frequency spectrum of a pseudo-PSD that is defined as the spectral density squared of one period of the same signal, divided by the period itself. The double-side pseudo-PSD of $x(t)$ can be then calculated as follows:

$$\tilde{S}_{xx}(f) = \frac{|X_0(f)|^2}{T_p} \quad (3.7)$$

Hence, the mean square value of a deterministic periodic signal, or equivalently its power if the signal is stationary, can be calculated both by the summation of its Fourier series coefficients squared, as according to the Parseval's theorem (Equation 2.20), and as the area underneath the pseudo-PSD defined here above.

$$P_x = \sum_{k=-\infty}^{\infty} |z_x(k)|^2 = \int_{-\infty}^{\infty} \tilde{S}_{xx}(f) df \quad (3.8)$$

The aperiodic version of the Parseval's theorem defined in Equation 2.16 is here generalized in Equation 3.8 to complex periodic waveforms.

3.2. Analytical Pointing Performance Estimation

Once the pointing error source has been characterized in the frequency domain the following step is to evaluate its contribution to the system pointing error budget. First of all, a PES transfer analysis is hereby performed to verify the theory describing plateaus and spikes disturbances in the frequency domain by means of a comparison of analytical results with numerical results. Secondly, a pointing error evaluation is performed in order to assess the overall pointing performance of the H_∞ controller with respect to both the disturbance transients

due to friction instabilities, d_{FTI} , and the reference noise PES's, d_{RW} , d_{SP} and n_{S} , according to the problem configuration provided in Figure 2.5. The overall pointing error indices obtained are the reference performance's values with respect to which the control solutions, described in the next two chapters, are compared with.

3.2.1. Plateaus and Spikes Torque Transfer Analysis

Recalling the expressions of the rectangular and triangular functions introduced in Section 3.1.1, the transient profiles can be described in the frequency domain both by the Fourier series coefficients and by the pseudo-PSD formalism. The mathematical derivations of the Fourier representations of rectangular and triangular periodic functions are reported in Annex B.2, while the resulting expressions of the pseudo-PSD's are provided here below in Table 3.1.

	Fourier Series Coefficients	Pseudo-PSD
Plateaus	$z(k) = \tau_{\max} \frac{T_d}{T_p} \text{sinc}(k\omega_0 T_d / 2)$	$\tilde{G}_{dd}(\omega) = \frac{(\tau_{\max} T_d)^2}{T_p} \text{sinc}\left(\omega \frac{T_d}{2}\right)^2$
Spikes	$z(k) = \tau_{\max} \frac{T_d}{2T_p} \text{sinc}(k\omega_0 T_d / 4)^2$	$\tilde{G}_{dd}(\omega) = \frac{(\tau_{\max} T_d)^2}{4T_p} \text{sinc}\left(\omega \frac{T_d}{4}\right)^4$

Table 3.1: Plateaus and spikes torque profiles' pseudo-power spectral density expressions

Thus, the expressions of the pseudo-PSD's obtained can be plotted as graphically illustrated in Figure 3.4. From the magnitude plot (left side) it can be noticed that the power is concentrated at the fundamental frequency and its multiples, which is to be expected for a periodic signal. Additionally, magnitude converges to a non-zero value as $\omega \rightarrow 0$, this is because both the signals illustrated in Figure 3.2 and Figure 3.3 do not have a zero mean. The Fourier coefficient in correspondence of $\omega = 0$ represents indeed the static gain of the signal. However, what is more important is that from the cumulative sum of the integral of the pseudo-PSD derived, it can be observed that these disturbances bring the major contribution in the low frequency domain. However, it has to be remarked that these error sources cannot be addressed as solely low-frequency disturbances because their power spectrum is still distributed among the whole frequency domain. Most of the periodic plateau disturbances' power is spread up to 0.1 Hz. The power of the periodic spike disturbance is instead distributed over a wider frequency range. This difference is due to the fact that since spikes have been spotted to occur more frequently, therefore in Table A.3 the spike profile considered has a smaller period. This leads to a higher fundamental frequency $f_0 = 1/T_p$ and hence a wider power distribution over the spectral domain.

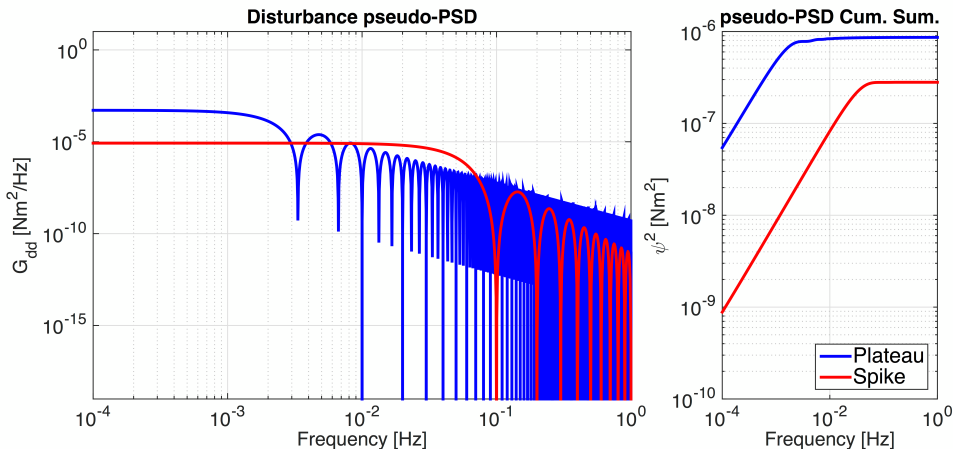


Figure 3.4: Pseudo-power spectral density (left plot) and cumulative sum of the latter (right plot) for plateaus and spikes torque profiles

As a result, also the contribution of periodic plateaus and spikes disturbances to the absolute pointing error can be evaluated using Equation 2.25. The pseudo-PSD of these disturbances is transmitted through the system as follows:

$$G_{ee} = |H_d(j\omega)|G_{dd} \quad (3.9)$$

where H_d is the transfer function from the RW disturbance to the attitude pointing error as defined in Section

2.2. Since a parametric expression of these disturbances' pseudo-PSD has been obtained, also a parametric expression of their contribution to the different pointing error indices, i.e. the PEC, can be computed. According to the ECSS standard the PEC has to be expressed in terms of error variance, that can be obtained integrating the PSD of the error signals at issue.

$$\begin{aligned}\sigma_{\text{ind,PL}}^2 &= \frac{(\tau_{\max} T_d)^2}{T_p} \frac{1}{2\pi} \int_0^\infty |H_d(j\omega)|^2 F_{\text{metric}}(\omega) \text{sinc}\left(\omega \frac{T_d}{2}\right)^2 d\omega \\ \sigma_{\text{ind,SP}}^2 &= \frac{(\tau_{\max} T_d)^2}{4T_p} \frac{1}{2\pi} \int_0^\infty |H_d(j\omega)|^2 F_{\text{metric}}(\omega) \text{sinc}\left(\omega \frac{T_d}{4}\right)^4 d\omega\end{aligned}\quad (3.10)$$

The expressions derived give important insights on the impact of the torque profiles characteristics to the pointing error budget. It can be noticed in Equations 3.10 that in both cases the PEC's are proportional to the maximum torque level of the disturbance squared, τ_{\max} , and inversely proportional to the disturbance period, T_p . As a result, once the integral on the right-hand side is calculated, sensitivity analysis can be analytically performed with respect to these two parameters. As far as the disturbance duration, T_d , is concerned, the integral in Equations 3.10 can be calculated for different values of T_d and a regression curve can be later constructed as illustrated in Figure 3.5 (calculations are hereby performed considering the plateaus torque profile).

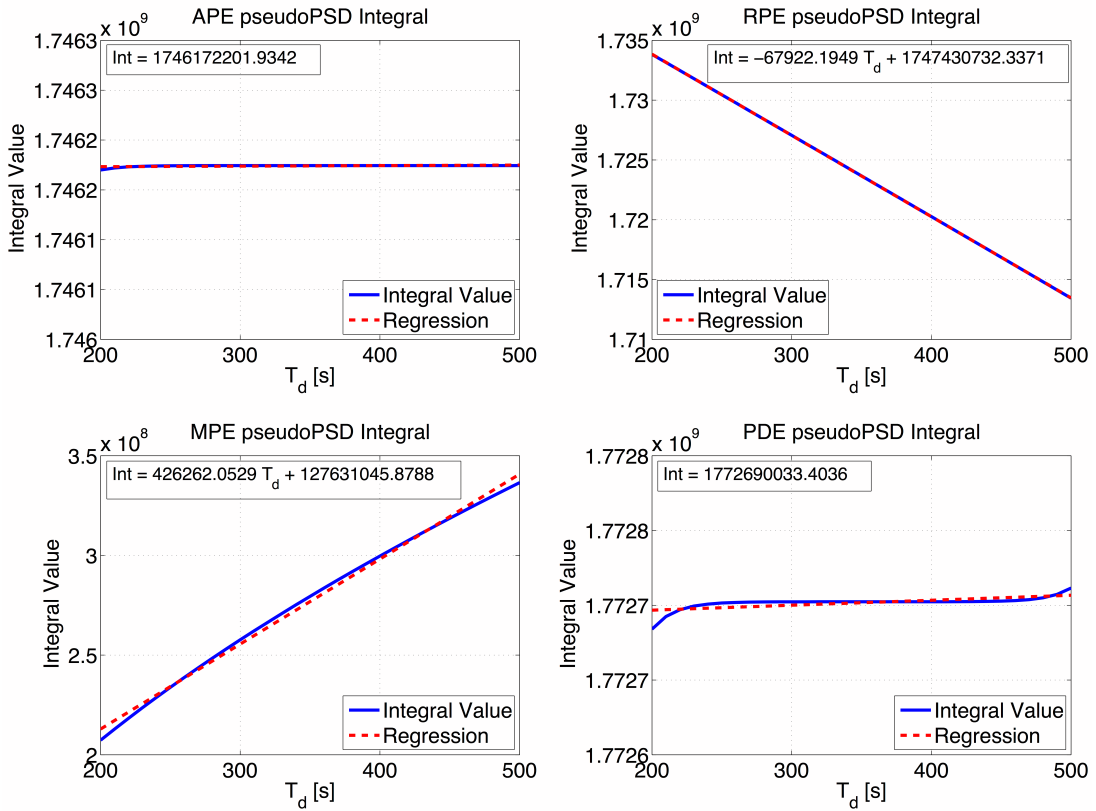


Figure 3.5: Variation of the PEC's integral with respect to the plateau transient's duration T_d

The integrals of the APE is independent of the duration of the plateaus, at least for a controller characterized by asymptotic disturbance rejection. If a single period is considered, the absolute pointing error drops to zero after both the initial and final steps that a plateau profile consists of, the system response to these steps is equal but with opposite signs. Therefore the APE over a single period clearly depends only on the amount of step-like disturbances occurring and not on the time passing between the positive and negative steps. The reasoning can be then extended ideally to the complete time domain response with an infinite periodic series of plateaus. Then, the greater is the plateaus' duration the larger is the impact on the low frequency range. Thus, the contribution on the MPE increases while the one on the RPE evidently decreases. Also the PDE, in the range of plateau's durations considered hereby, can be regarded as constant but it is affected by a greater variability depending on the values of time windows used. In conclusion, the contribution of a plateaus disturbance to the different pointing error indices can be parametrized with respect to the different torque profile characteristics as described in Table 3.2. The values of the regression curve's coefficients, C_0 and C_1 , are the one reported in Figure 3.5.

Parametric Estimation	
$\sigma_{\text{APE},\text{PDE}}$	$= \frac{\tau_{\max}}{\sqrt{T_p}} (C_0)$
$\sigma_{\text{RPE},\text{MPE}}$	$= \frac{\tau_{\max}}{\sqrt{T_p}} (C_1 T_d + C_0)$

Table 3.2: Parametric formulas for pointing error contributions' estimations with respect to a plateaus disturbance

3.2.2. Pointing Error Evaluation

Provided with the PSD of an error source, the different pointing error contributors, as introduced in Chapter 2, can be evaluated transferring the pointing error through the ACS. Therefore, the transfer characteristics of the control system have to be derived. The standard scheme illustrated in Figure 2.6 is then specifically applied to the reference attitude control problem. As described in Figure 3.6, the PSD's of noise and disturbance inputs considered in the case study, respectively G_{nn} and G_{dd} , are propagated through the system to the pointing error index of interest, G_{ee} , eventually the integration over the frequency spectrum leads to the different PEC's, which are expressed in terms of standard deviations of the absolute and windowed pointing errors.

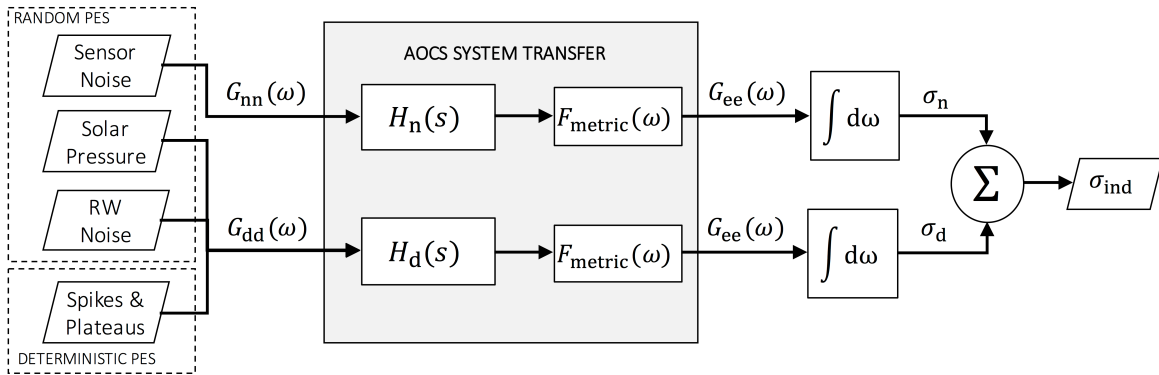


Figure 3.6: ACS pointing error sources transfer analysis diagram

According to the control system structure, as described previously in Figure 2.5, the relevant system transfer functions can be derived. These are reported in Table 3.3.

e_{APE}	
n_S	$H_n(s) = \frac{KG_A G}{1+KG_A GG_S}$
d_{FTI}	$H_d(s) = -\frac{G}{1+KG_A GG_S}$
d_{RW}	$H_d(s) = -\frac{G}{1+KG_A GG_S}$
d_{SP}	$H_d(s) = -\frac{G}{1+KG_A GG_S}$

Table 3.3: Transfer function from the different input noise/disturbances (rows) to the absolute pointing error index

According to the nomenclature used in Figure 3.6 and the guidelines provided in [11], the pointing error budget can be assessed calculating the different contributions of noise and disturbance error sources.

$$\sigma_{\text{ind},n}^2 = \int_0^\infty |H_n(j\omega)|^2 F_{\text{metric}}(\omega) G_{nn}(\omega) d\omega \quad (3.11)$$

$$\sigma_{\text{ind},d}^2 = \int_0^\infty |H_d(j\omega)|^2 F_{\text{metric}}(\omega) G_{dd}(\omega) d\omega \quad (3.12)$$

Assuming the error sources to be uncorrelated, the overall pointing error can be calculated as the statistical sum of the noise and disturbances contributions.

$$\sigma_{\text{ind}}^2 = \sigma_{\text{ind,d}}^2 + \sigma_{\text{ind,n}}^2 \quad (3.13)$$

where the disturbance contribution consists of the RW friction noise, RW disturbance transients and solar pressure torques, $\sigma_d^2 = \sigma_{d,\text{FTI}}^2 + \sigma_{d,\text{RW}}^2 + \sigma_{d,\text{SP}}^2$. The pseudo-PSD's of the disturbance transients, as far as spikes and plateaus profiles are concerned, are analytically provided in Table 3.1 and the analytical expressions of their PEC's have already been derived in the previous section. Whereas as far as the reference random PES's are regarded, they are treated as band-limited white noise, hence their contributions to the pointing error budget are evaluated according to the procedure used in [25]. The power spectral density of these noise sources can be derived directly from shaping filter used to describe them that are provided in Appendix A.

$$\begin{aligned} G_{nn}(\omega) &= W_n(s)N_{ww}(\omega)W_n(s)^* = |W_n(s)|^2 \\ G_{dd}(\omega) &= W_d(s)N_{ww}(\omega)W_d(s)^* = |W_d(s)|^2 \end{aligned} \quad (3.14)$$

where $W_n(s)$ and $W_d(s)$ are spectral shaping filters, and N_{ww} is an ideal white noise PSD with unitary power.

3.2.3. Verification

The analytical tool is then applied to the case study in order to assess the performance of the H_∞ controller designed with the 2PCD tool. The different pointing error indices are calculated both analytically, according to the procedure described above, and numerically.

Firstly, the validity of the mathematical derivation described in Section 3.1.1 are verified comparing the pointing error budget obtained analytically through Equation 3.10 and the one calculated applying the proper time-domain metrics of Table 2.2 to the absolute pointing error obtained through simulations. Time-series of the disturbance transients profiles are manually constructed and the time response of $H_d(s)$ is numerically evaluated using the Matlab function *lsim*.

In a second instance, the overall pointing error indices are evaluated analytically summing all the noise and disturbance contributions, as it is done in Equation 3.13, and then compared to the results obtained using time-domain simulations performed with the AOCS simulator of the 2PCD tool. To do so, the Simulink block of the RWA has been properly enhanced, so that plateaus and spikes transients can be included in the time-domain simulations. The parameters used for the windowed pointing error metrics are listed in Table A.2.

Plateaus Disturbance Case Study

Pointing error budget analysis is performed considering a rectangular waveform as the one illustrated in Figure 3.2 and the disturbance profile's parameters used are the one listed in Table A.3.

In the following figures, the square root of the variance cumulative sum is reported with respect to the different pointing error contributors. According to the Parseval's theorem it is equivalent to the square root of the cumulative integral of the PSD. It is a powerful tool to analyze in which frequency range the power of the spectrum is concentrated. In each figure, the blue line represents the cumulative error variance calculated through the integration of the PSD that has been obtained numerically from the error's time-series.

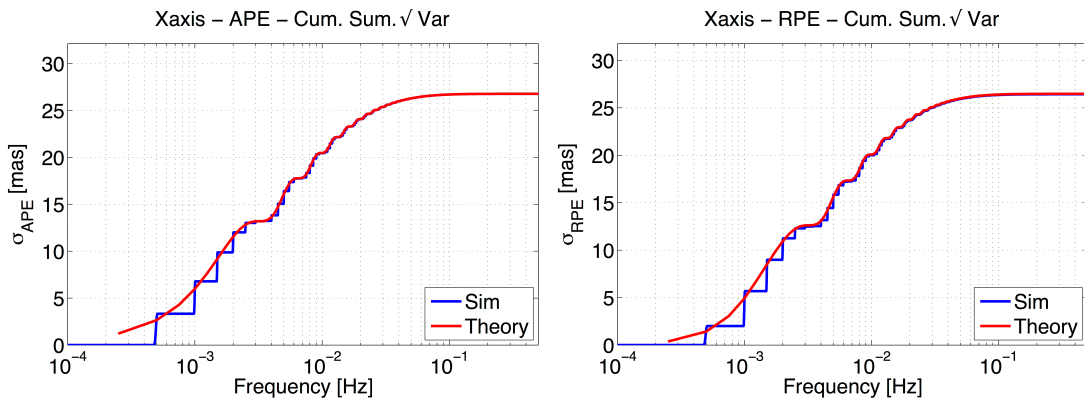


Figure 3.7: APE cumulative spectral variance (plateaus profile)

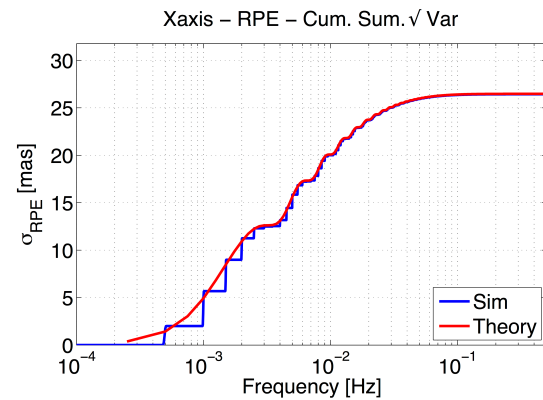


Figure 3.8: RPE cumulative spectral variance (plateaus profile)

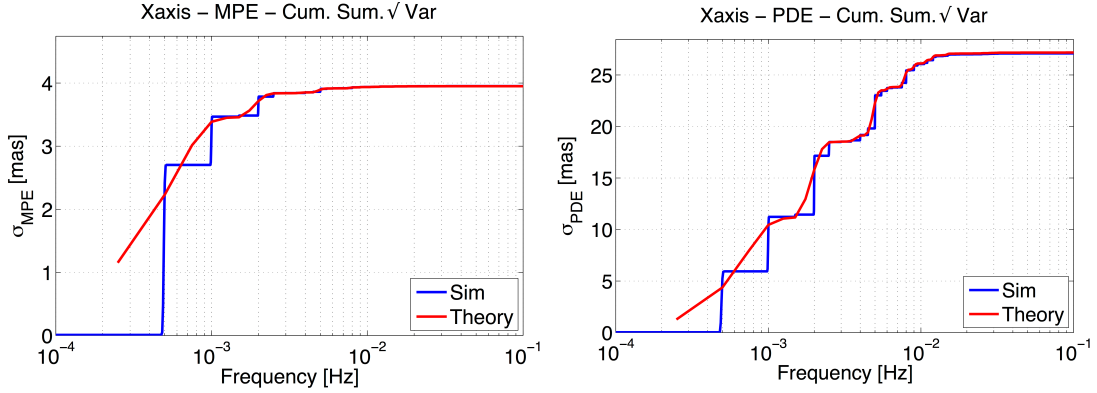


Figure 3.9: MPE cumulative spectral variance (plateaus profile)
Figure 3.10: PDE cumulative spectral variance (plateaus profile)

Since the disturbance considered is periodic, the power spectrum is concentrated at discrete frequencies thus the variance builds up through a series of discrete steps, clearly visible in the figures below. The analytically derived pseudo-PSD (red line) is instead defined among the continuous frequency spectrum according to the expressions provided in Table 3.1, hence the signal power is distributed over the whole frequency domain. At high frequencies the input is filtered out by the system so the PSD of the pointing error drops to zero and the area underneath converges to a finite value as $f \rightarrow \infty$.

Moreover, it can be observed in the figures that APE and RPE contribution is spread until 0.1 Hz while MPE and PDE are limited to 0.01 Hz. This result is in accordance with theory because MPE and PDE weighting filters cut-off the high-frequency content of the pointing error signal. After all, the numerical and analytical estimations converge to the same value as $f \rightarrow \infty$.

The pointing error contributions of a plateaus disturbance, i.e. the value at which the cumulative sum converges, are reported in Table 3.4, showing the compliance between analytical estimations and numerical simulations. Values displayed are expressed in terms of standard deviation.

	σ_{APE} [mas]	σ_{RPE} [mas]	σ_{MPE} [mas]	σ_{PDE} [mas]
Theory	26.770	26.477	3.950	27.177
Simulation	26.770	26.475	3.951	27.02

Table 3.4: Pointing error contributions of plateaus disturbance calculated analytically and numerically

The differences existing between results are due to the fact that when statistical metrics are applied to time-series obtained through numerical simulations the outcome depends on the time step and simulation time regarded. Eventually, as far as also the reference noise PES's are taken into account in the error budget, the overall pointing performance is computed and reported in Table 3.5.

	σ_{APE} [mas]	σ_{RPE} [mas]	σ_{MPE} [mas]	σ_{PDE} [mas]
Theory	34.143	33.907	4.001	27.778
Simulation	37.7	35.5	4.58	28.4

Table 3.5: Global pointing performances with respect to plateaus disturbance calculated analytically and numerically

The analytical estimations are hereby compared with a numerical simulation performed with the in-house AOCS simulator. The differences between results are due to the fact that nonlinearities and model uncertainties are additionally regarded in the simulator.

Spikes Disturbance Case Study

The same pointing error budget analysis is then performed considering a triangular waveform as the one illustrated in Figure 3.3 and the disturbance profiles parameters used are the one listed in Table A.3.

In the following figures, the cumulative sum of the variance is reported w.r.t. the different pointing error contributors. The same considerations made for the plateaus profile analysis hold also in this case. Compared to the previous case, spike disturbances' contribution is more shifted towards higher frequencies according to the reasoning provided in Section 3.2.1. It can be observed that the pseudo-PSD well reproduces the actual disturbance contribution and the cumulative variance of the different pointing error indices converges to the same value, both if calculated analytically and numerically.

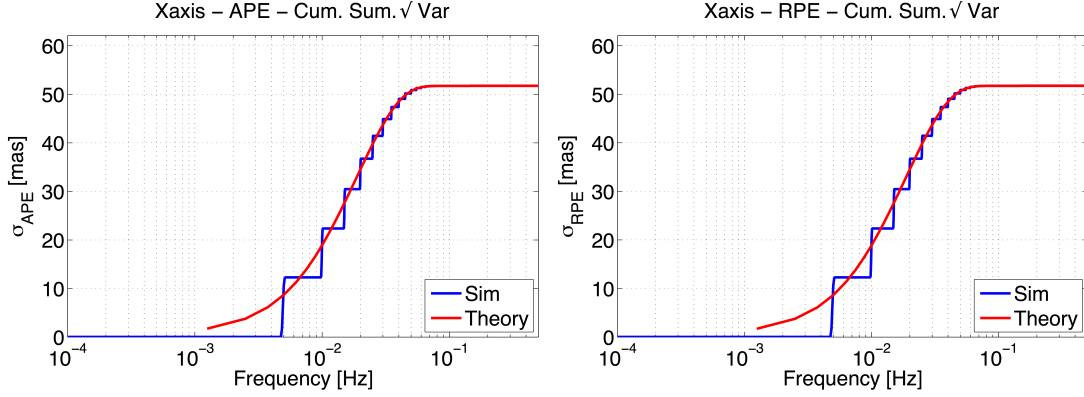


Figure 3.11: APE cumulative spectral variance (spikes profile) Figure 3.12: RPE cumulative spectral variance (spikes profile)

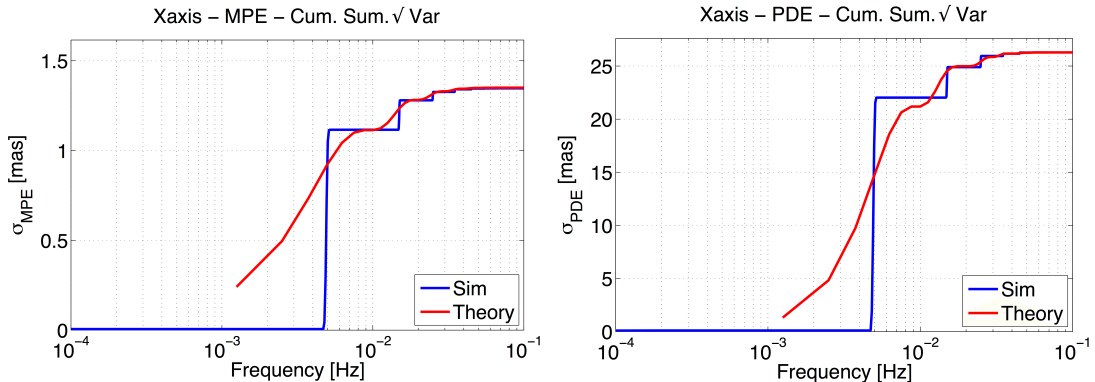


Figure 3.13: MPE cumulative spectral variance (spikes profile) Figure 3.14: PDE cumulative spectral variance (spikes profile)

The pointing error contributions of a spikes disturbance torque are then reported in Table 3.6, showing the compliance between analytical estimations and numerical simulations. Values displayed are expressed in terms of standard deviation.

	σ_{APE} [mas]	σ_{RPE} [mas]	σ_{MPE} [mas]	σ_{PDE} [mas]
Theory	51.751	51.733	1.350	26.280
Simulation	51.751	51.733	1.347	26.281

Table 3.6: Pointing error contributions of spike disturbance calculated analytically and numerically

Eventually, as all the other pointing error sources are also taken into account, the overall pointing performances are computed. The analytical estimations are compared with numerical simulation performed with the in-house AOCS simulator and results are provided in Table 3.7. Also in this case, the difference within results is due to the fact that nonlinearities and model uncertainties are considered in the simulator.

In both cases, Table 3.7 and 3.5, it can be observed that the largest relative error, between analytical estimations and numerical simulations, concerns the pointing error indices addressing the high frequency domain (like APE and RPE). In this region the impact of noise error sources is dominant and its value is higher if computed with time-domain simulations. The MPE instead, since its weighting filter is a low-pass, addresses the

low-frequency domain where the contribution of spikes and plateaus is prevailing. With this respect the discrepancy between results is relatively smaller, meaning that the analytical characterization of plateaus and spikes disturbances, which are the focus of this work, is valid.

	σ_{APE} [mas]	σ_{RPE} [mas]	σ_{MPE} [mas]	σ_{PDE} [mas]
Theory	55.9	55.9	1.52	26.9
Simulation	56.8	56.5	1.62	28.8

Table 3.7: Global pointing performances with respect to spikes disturbance calculated analytically and numerically

3.3. Discussion of Results

An analytical tool has been developed to describe plateaus and spikes torque profiles in the frequency domain. Its validity has been later on verified and proved comparing the results with numerical simulations. The pseudo-PSD formalism defined for friction torque instabilities can be then later use for several purposes:

- In the following chapters the controller tuning can be quickly performed analytically without the need of numerical simulations. Because the impact of disturbance transients on the different pointing error indices can be estimated analytically and then optimized.
- The plateaus and spikes disturbances' pseudo-PSD could be later included in the noise transfer optimization procedure implemented in the 2PCD tool. Its capabilities can be then further extended also to wheels disturbances transients.
- Parametric expressions for the impact of plateaus and spikes on the different performance pointing errors have been derived. These can be used to draw important considerations when the pointing error budget is compiled. Pointing error allocation can be then optimized also with respect to friction torque instabilities' torque profiles.

After all, the mathematical derivations introduced here above have some room of improvements. For example, the spikes disturbances might be modeled more in details as a sequence of a very steep ramp and an exponential decay, in order to obtain an even closer representation of the actual disturbance. Then, the same approach introduced hereby could be applied to perform pointing error analysis. In addition, other disturbance torque profiles can be considered and included in the calculations.

4

Optimization of the H_∞ Controller Integral Action

In this chapter, the first solution that can be applied to reduce the impact of wheels disturbance transients is confronted. It consists in adding an integral action to the reference controller and further optimize it with respect to the friction torque instabilities at issue. This solution has been already investigated in a pointing stability analysis performed for the Euclid mission, [36], and the idea of adding an integral estimator was mentioned in [20] to improve the ACS performance with respect to constant disturbances. Within the 2PCD frame, in [24] the integral part of the H_∞ controller is optimized with respect to a step disturbance by means of iterative simulations. The main objective is hereby to extend the controller optimization to periodic plateaus and spikes, as addressed in Chapter 3, by means of the analytical tool developed.

The first question that has been tackled is why an integral action is required within the problem at stake, hence in Section 4.1 some analytical preliminaries are provided. Then, both strengths and weaknesses of this solution are investigated and discussed. Later on, a method to optimize the effectiveness of the integral action with respect to both plateaus and spikes disturbances is implemented in the 2PCD tool and discussed in Section 4.2. In conclusion the performance improvements achieved with an optimized integral action are assessed analytically with respect to the reference case study and results are reported in Section 4.3.

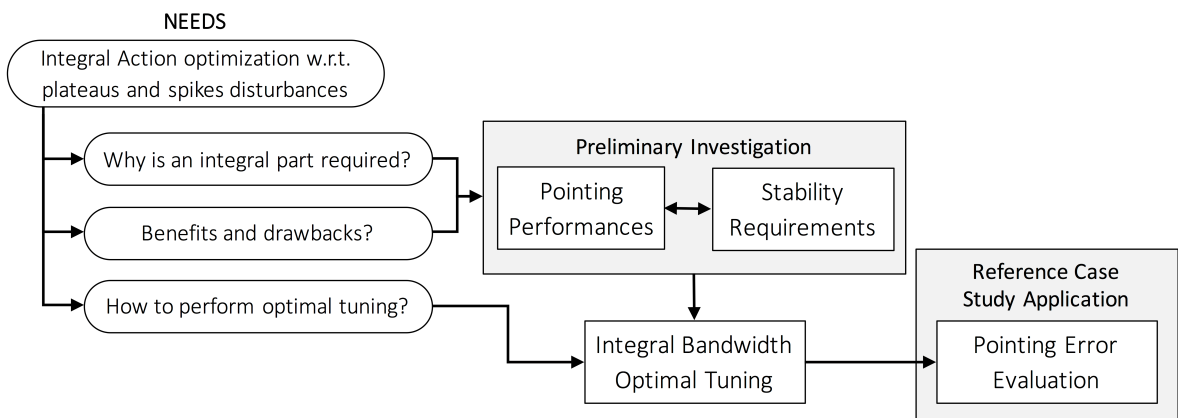


Figure 4.1: Overview of the fourth chapter's contents

In Figure 4.1 the various steps of the analysis discussed in this chapter are illustrated. The investigation about the benefits and drawbacks of such a solution is a crucial step because it leads to discover unavoidable trade-offs that brings about the need for an optimal tuning of the integral controller. Indeed, the choice of the optimal integral controller results to be influenced by both stability requirements and noise and disturbance rejection performance. Eventually, it turns out that the optimization of the pointing performance impairs the stability of the attitude control system.

4.1. General

From general control theory, the presence of a integrator in the controller is necessary when constant disturbances are affecting the system, according to [35] and [8]. This is the case of the wheel disturbance transients here regarded, it has indeed been showed in Section 3.1 that cage instabilities lead to a disturbance drag torque characterized by two subsequent steps.

The need for a integrator, i.e. a pole in $\omega = 0$ can be analytically demonstrated by looking at a simple case study. In the following, a standard proportional-derivative (PD) and proportional-integral-derivative (PID) controllers are compared in order to show the importance of an integral action at the ACS level. PID controllers have been studied within the spacecrafts attitude control problem because they are very easy to implement. A PD controller can be also employed for stability purposes, in [13] the Lyapunov stability of an attitude control system driven by a PD controller is demonstrated. Nevertheless, as far as constant external disturbances are regarded only a PID controller can cope with them as discussed in [13] and [7]. Specifically, if a single step is considered as a disturbance torque, it can be shown that, when only a PD controller is regarded, the system's steady-state reference tracking performance is impaired. A PD controller's transfer function can be indeed written as follows:

$$K_{\text{PD}}(s) = k_P + k_D s \quad (4.1)$$

where k_P and k_D are the proportional and derivative coefficients, respectively. According to [8], a PID controller can be designed as a combined PD and PI, so that the contributions of the two parts can be treated separately. This approach is going to be also exploited later on when the reference case study is concerned. The PID controller transfer functions can be then written as follows:

$$K_{\text{PID}}(s) = K_{\text{PD}}(s)K_{\text{PI}}(s) = k_0(k_{\text{PD}}s + 1) \left(\frac{k_{\text{PI}}s + 1}{s} \right) \quad (4.2)$$

where k_0 is the proportional gain, while k_{PD} and k_{PI} are the derivative and integral gain, respectively. When the spacecraft is operating in observation mode the controller should be able to provide the system with zero steady-state tracking error. This capability is commonly addressed as *asymptotic disturbance rejection* and it is achieved only if the magnitude of the transfer function from the disturbance to the pointing error, $H_d(s)$, collapses to zero as $\omega \rightarrow 0$, [8]. Thus, assuming no delays due to actuators or sensors acting on the system, $H_d(s)$ can be derived according to the diagram illustrated Figure 2.5, further details are provided in Annex C.1. Then, applying the final value theorem the steady-state error, e_{ss} , due to a step response can be computed as follows:

$$e_{\text{ss}} = \lim_{s \rightarrow 0} s H_{d,\text{PD}}(s) \frac{1}{s} = \frac{1}{k_P} \quad (4.3)$$

$$e_{\text{ss}} = \lim_{s \rightarrow 0} s H_{d,\text{PID}}(s) \frac{1}{s} = 0 \quad (4.4)$$

It can be observed that in the PD controller case $H_d(s)$ has a non-zero static gain, thus it cannot provide zero steady-state when step or plateaus-like disturbance are acting on the system. This can be also inferred from the left-side plot of Figure 4.2, where the response of a system with a PD controller is displayed when a plateau transient is given as disturbances input. While the cage instability is occurring, the absolute pointing error is subjected to a non-zero mean jump and also the other windowed pointing error indices are greatly affected. However, from Equation 4.3 it can be said that if there is no integrator in the controller, the steady-state error can still be reduced by increasing the proportional gain. Nevertheless, as mentioned by [8], the latter solution is very likely to violate the actuators' limitations, hence it is not feasible.

In contrast, the transfer function $H_d(s)$ has a null static gain when a PID controller is included in the loop. In this case constant disturbances can be then handled. From the right-side plot of Figure 4.2 it can be indeed observed that the absolute pointing error drops back to the zero reference after a step has occurred.

In conclusion, it has been demonstrated that as constant disturbances are acting on the system an integrator is strictly required if asymptotic disturbance rejection is to be achieved. Also in the field of robot manipulators, where gravity acts as a constant disturbance, a sole PD controller is not sufficient, either it has to be coupled with a model-based disturbance compensator or with an additional integral term as proposed in [14]. In Chapter 1 it has been shown that in-flight observation reported the occurrence of plateaus-like disturbances due to RW's instabilities. Hence, since zero steady-state tracking is required for high-precision science operation modes, it follows that the controller should be provided with an integral part.

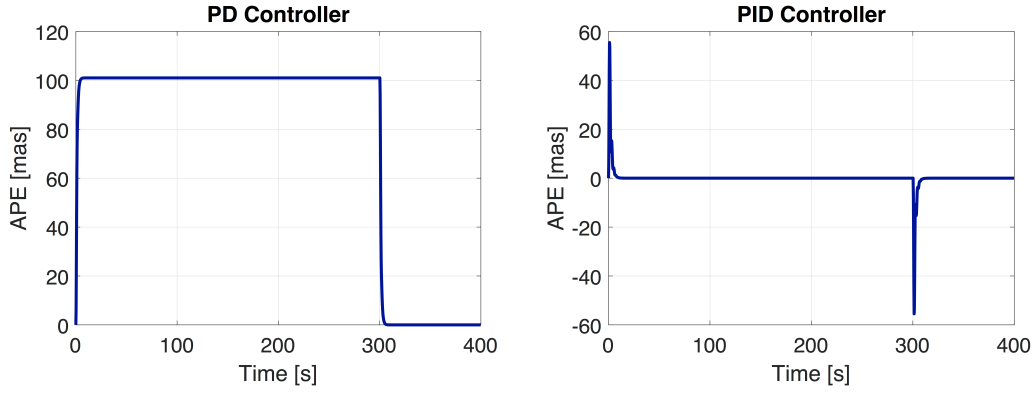


Figure 4.2: Time-domain response of a PD controller (left figure) and of a PID controller (right figure) when a plateau transient is introduced as disturbance

Limits Recalling Equation 4.2, the zero of the PI controller transfer function is located in $\omega = k_{\text{PI}}$ and it corresponds to the corner frequency that determines the integral bandwidth of the controller. The closed-loop's system bandwidth is pushed towards higher frequencies the higher the value of k_{PI} is. The integral term adds gain in the low frequency range to the open-loop transfer function $L(s)$, that hence approaches infinity at the origin, while the high-frequency (HF) range is not influenced. Therefore, if an integrator is added in the open-loop, the sensitivity function $S(s)$ will drop to zero more rapidly as $\omega \rightarrow 0$. This results in improved steady-state external disturbance rejection in the low-frequency (LF) range, where indeed friction torque instabilities concentrate their power content, as it has been showed in Section 3.1. The transfer function from the disturbance source to the attitude pointing error, according to Section 2.2.2 is indeed proportional to the sensitivity transfer function. As a result, the greater is the integral bandwidth the larger is the amount of low-frequency disturbances suppressed. Whereas, as far as measurement noise is concerned, according to Section 2.2.2 the complementary sensitivity function $T(s)$ has to be analyzed. In the high frequency range it holds $T(s) \approx L(s)$ hence, since noise signals are concentrated in this region, the noise rejection performance remains unchanged, nevertheless the greater is the integral bandwidth the higher is the complementary sensitivity function cut-off frequency. This leads to an increasing level of noise contribution to the pointing error. The classical trade-off mentioned in Section 2.2 between disturbance and noise rejection objectives here shows up, and it is also graphically explained in Figure 4.3, where the magnitude of $H_d(s)$ and $H_n(s)$ are plotted for increasing values of the integral coefficient k_{PI} .

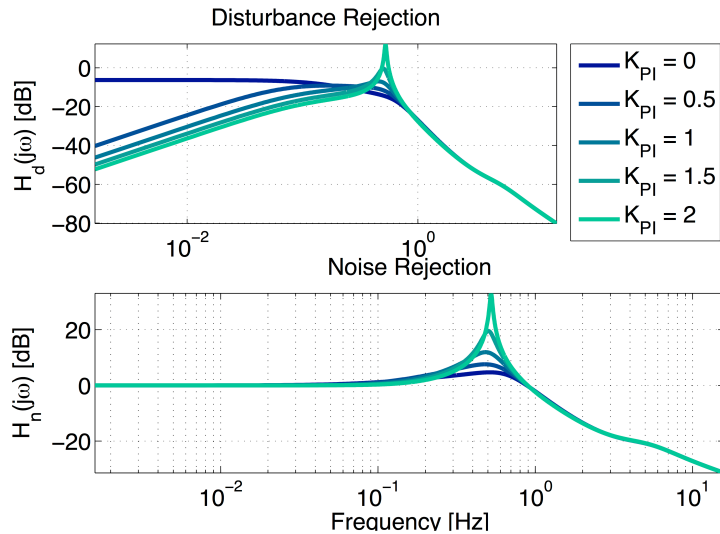


Figure 4.3: Magnitude plots of disturbance and noise rejection characteristics of a PID-based attitude control system, transfer functions are evaluated for different values of integral bandwidth

Benefits with respect to LF disturbance rejection are clearly visible in the upper diagram since the disturbance

transfer function drops to zero faster for large value of k_{PI} . While performance with respect to noise sources are worsened because the transmission of this error source is amplified close to cut-off frequency.

In addition, the PI controller introduces also a certain amount of phase lag that increases as the integral bandwidth gets larger. It can be indeed noticed in Figure 4.3 that the integral contribution leads to a modification of the dynamic resonance in the system's bandwidth neighborhood. In Figure 4.4 the time responses of the system to a torque step of 5 [mNm] is illustrated for different values of integral bandwidth. In the last simulated cases an under-damped response can be observed, the behavior of the system then worsens until for $k_{PI} = 2$ it becomes unstable. It appears that the impact on the peak level of the absolute error is rather small as the integral bandwidth is increased. But on the other hand, the transient phase is greatly improved. The larger is the integral coefficient, faster dynamics are excited and the system response w.r.t. a step disturbance is faster as well, leading to a shorter settling time.

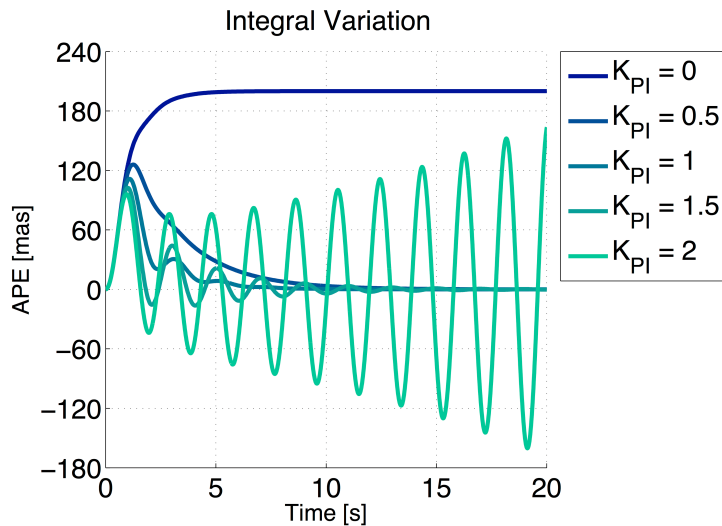


Figure 4.4: Step responses of a PID-based attitude control system evaluated for different values of integral bandwidth

Hence, there is a maximum value of the integral bandwidth over which the system becomes unstable. This can be proven by looking at the root locus plot of the closed-loop transfer function $H_{CL}(s)$ defined in Section 2.2.1 as the integral coefficient moves further from the origin. The root locus represented in Figure 4.5 regards the closed-loop transfer function with a PID controller included.

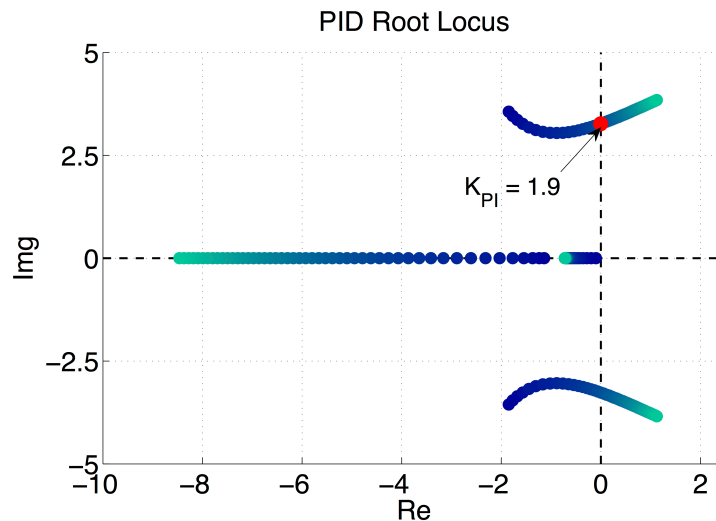


Figure 4.5: Closed-loop system's root locus for a PID-based attitude control system as the integral gain varies

As it can be noticed in Figure 4.5, when the value of the integral gain is larger than 1.9 the closed-loop system has two positive real-part poles, meaning that stability is lost according to the criteria introduced in Section

2.2. Both gain and phase margins are indeed affected by a large integral bandwidth, but the phase margin is the parameter that endures the highest impact and that leads to instability.

4.2. Integral Action Optimization

4.2.1. Controller Synthesis

The analysis presented here above demonstrates that once the ACS controller is required to deal with non-stationary disturbances, an integrator is necessary for asymptotic disturbance rejection. However, the integral bandwidth cannot be increased without bounds because stability might be lost and the noise contribution to the pointing error becomes larger.

The original controller obtained with the H_∞ synthesis from the 2PCD tool is optimized with respect to noise disturbance transmission. The idea introduced in [24] consists in performing several pointing error evaluations numerically, for different value of the integral bandwidth and then to select the optimal one. While only a step disturbance was considered before, hereby the optimization is performed analytically and additionally both spikes and plateaus are regarded. Since the controller obtained from the H_∞ synthesis already has a pole in the origin, the integral part K_{int} of the original controller K_∞ has to be isolated, as illustrated in Figure 4.6.

$$K_\infty = K_0 K_{\text{int}} = K_0 \left(\frac{s + k_{\text{PI}}}{s} \right) \quad (4.5)$$

The slowest zero of the K_∞ controller, k_{PI} , is addressed as the zero of the integral part according to [24]. Then, the integral action is optimized with respect to the position of the zero k_{PI} along the frequency axis.

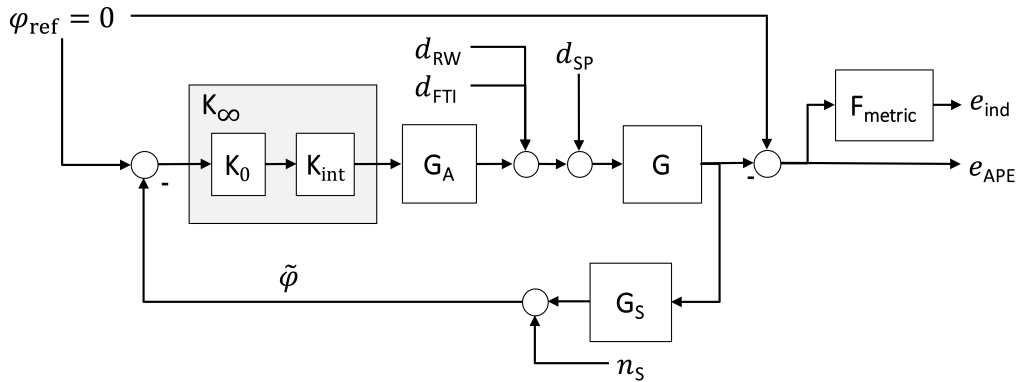


Figure 4.6: Closed-loop system diagram (SISO) for integral action optimization

Previously, it has been showed that the tuning of the integral controller results in a trade-off between disturbance and noise rejection and system stability, however, pointing performance is the driving factor for HPP mission. As a result, the integral tuning procedure implemented consists in the optimization of the pointing performance (i.e. the minimization of a pointing error index selected by the user) with the constraint of fulfilling the stability margins' requirements introduced in Section 2.2. The different pointing error contributors can be evaluated as explained in Section 3.2. According to Figure 4.6 noise and disturbance sources are then propagated through the ACS by means of the transfer functions described in Table 3.3. All the contributions are then statistically added up to come up with the overall pointing error indices as illustrated in Figure 3.6. Recalling Equation 3.13, for the reasons explained above the disturbance contribution $\sigma_{\text{ind},d}$ is expected to decrease as the integral bandwidth is raised, while the noise contribution $\sigma_{\text{ind},n}$ is likely to increase at the same time. Therefore it is reasonable to expect that the overall pointing error index has a local minimum when calculated for different values of k_{PI} .

All in all, the optimization process consists in evaluating both the disturbance and noise contributions to the pointing error index to be optimized, then looking for the value of k_{PI} that minimizes it and at the same time making sure all the stability requirements are met. The optimal tuning procedure hereby described is illustrated in Figure 4.8. Given the disturbance and noise PES's characterization in the frequency domain, the overall pointing error indices can be estimated analytically. Hence the optimal integral gain can be selected so that

the PEI considered is minimized and system stability is still preserved. In conclusion, the choice of the optimal integral action coefficient is led by the search of the minimum impact of combined noise and friction torque instabilities disturbances but also by stability reasons.

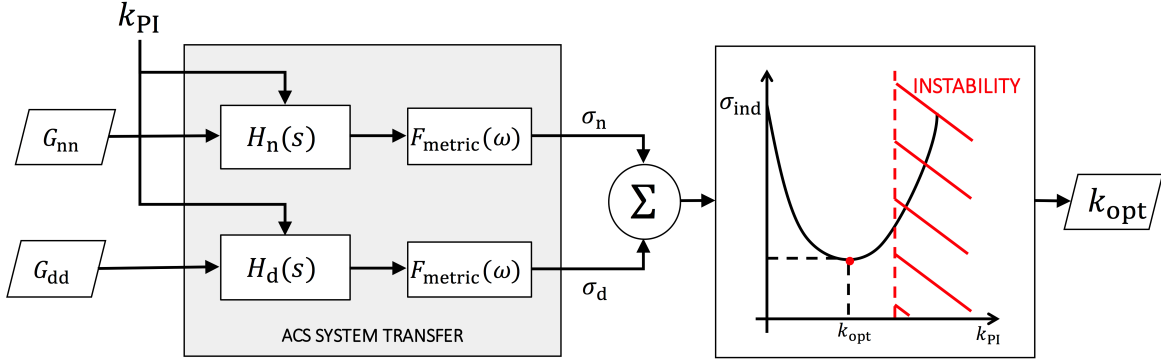


Figure 4.7: Integral gain optimization procedure diagram

4.2.2. Application to the Reference Case Study

The integral action optimization procedure introduced here above is then applied to the reference case study. Thus, given the K_∞ controller previously derived by means of the 2PCD Tool, the integral part K_{int} is optimized with respect to both a series of plateaus and spikes torque profiles. The parameters used for the transient disturbances are listed in Table A.2, while the stability requirements in Table A.4.

The tuning is performed with respect to the minimization of the RPE index. This error metric addresses the pointing error stability within a specific time window and, as explained in Chapter 2, it is equivalent to the concept of pointing stability commonly used within past HPP missions. Moreover, in [34] other types of reaction wheel disturbances were considered and the RPE was the pointing performance parameter addressed among the whole analysis. In Figure 4.8 the results of the integral action optimization for the reference case study are reported. The different impacts on the overall RPE of noise and disturbances, as the integral bandwidth is increased, can be distinguished.

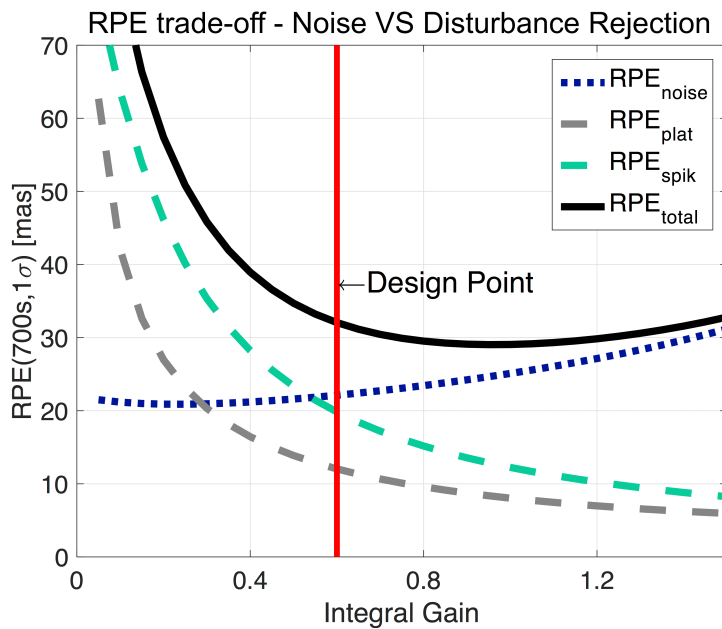


Figure 4.8: RPE budget for optimal tuning of the controller integral gain (x axis)

It can be indeed noticed that increasing the integral gain the performance with respect to plateaus and spikes

instabilities are enhanced while the noise's PEC gets larger, even though with a gentle slope. This result is in accordance with the preliminary analysis carried out in Section 4.1. As a result, the curve representing the cumulative RPE has a local minimum, that corresponds to the optimal value of integral gain, k_{opt} . However, as mentioned previously, stability also plays a considerable rule. Indeed, as it can be noticed in Figure 4.8, the resulting optimal value for the integral coefficient is not the one corresponding to the RPE curve minimum. All the relevant stability margins are worsened as the integral gain gets larger, as it can be observed in Figure 4.9. Phase margin, PM , drops quickly as expected from theory, while the gain margin, GM , decreases to a smaller extent with respect to the integral coefficient increment. According to the preliminary analysis the resonance behavior is also amplified therefore the peak values of the sensitivity and complementary sensitivity functions increase rapidly as more phase lag is added to the system. In this case, in correspondence of the RPE minimum the complementary sensitivity function peak value requirement is violated. As a result the value of k_{PI} smaller than the optimal one is considered.

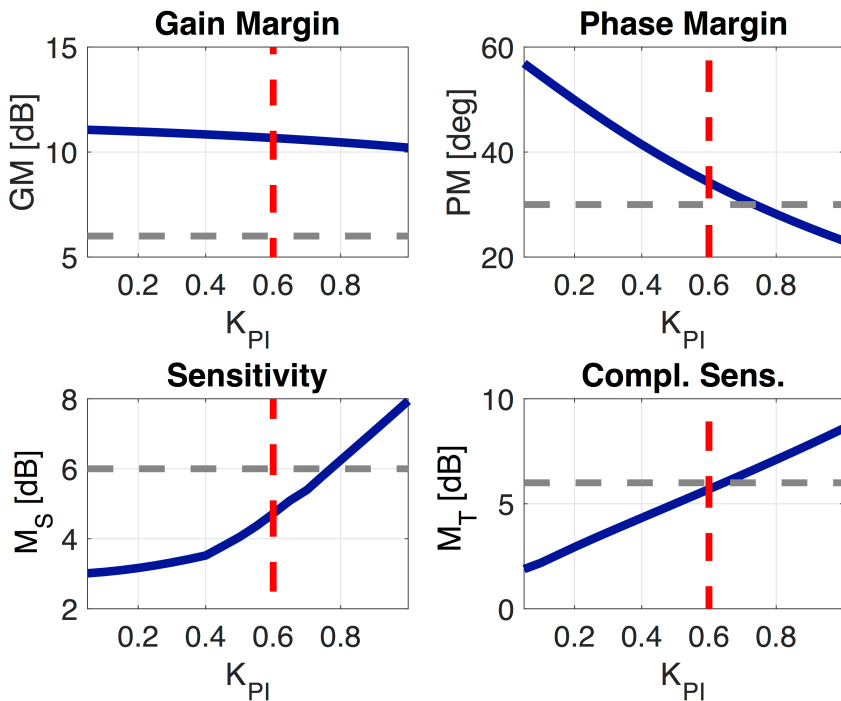


Figure 4.9: Stability margins' evolution with respect to the value of integral coefficient (x axis)

The figures hereby reported concern the optimization of the x axis controller within the reference case study. An optimal value of $k_{\text{PI}} = 0.6$ is the result of the integral action tuning. Results obtained for the y and z axes are summarized in Annex C.2.

4.3. Pointing Performance Evaluation

Eventually, in order to verify the performance improvements brought by the integral action optimization, a pointing error evaluation analysis has been performed, firstly regarding the reference controller designed through the 2PCD Tool, K_∞ , and then considering the controller with the optimized integral action, $K_{\infty,\text{opt}}$. Pointing and stability performances' improvements can be then verified comparing the results. The different error contributions are reported in order to investigate the impact of the control solution proposed on the transmission of the different PES's. The worst-case plateaus and spikes profile are addressed separately since according to the lesson learned from past missions the two disturbance transients have different origins and therefore occur in different situations.

4.3.1. Plateaus Disturbance Case Study

Numerical results obtained by analytical estimation of the pointing error budget when a plateau disturbance waveform is considered are displayed in the Table 4.1. The pointing error indices are reported in terms of standard deviation. The contributions of plateaus, d_{FTI} , reference measurement noise, n_S , and reference disturbances (RW friction noise, d_{RW} , and solar pressure noise, d_{SP}) to the different pointing error indices are reported.

		σ_{APE} [mas]	σ_{MPE} [mas]	σ_{RPE} [mas]	σ_{PDE} [mas]
K_∞	Plateaus	26.7701	3.9499	26.4771	27.177
	Ref. Disturbance	15.8139	0.2390	15.8121	4.6076
	Ref. Noise	14.1079	0.6456	14.0931	3.4402
	Total	34.1431	4.0095	33.9069	27.778
$K_{\infty,\text{opt}}$	Plateaus	5.7955	0.42259	5.7801	3.2949
	Ref. Disturbance	11.5393	0.04765	11.5393	0.9441
	Ref. Noise	18.6275	0.64533	18.6163	3.4116
	Total	22.6656	0.77285	22.6524	4.8395

Table 4.1: Pointing error budget with respect to a plateaus disturbance, (x axis)

From the results obtained several considerations can be made, specifically looking at Table 4.2 where the various PEC's resulting from the integral action optimization case, $K_{\infty,\text{opt}}$, are expressed in relation to the values obtained when the original controller, K_∞ , is regarded in the calculations. The impact of the disturbances is decreased both for the RWs' transients, d_{FTI} , and for the reference disturbance, d_{RW} and d_{SP} . Since the integral action is aimed to improve disturbance rejection performance in the LF range, plateaus disturbance's contribution is minimized to a greater relative extent if compared to reference disturbances and, additionally, MPE and PDE which are the windowed errors addressing the LF domain experience a greater decrement compared to APE and RPE. Regarding random noise disturbances this difference is considerable, 27% reduction for APE and RPE against 80% for MPE and PDE, this is due to the fact that reference noises' power content is distributed also at high frequencies that are not affected by the integral action. Whereas for the plateaus disturbance also APE and RPE are greatly optimized since the error source is in this case concentrated at low frequencies. On the other hand, as far as the measurement noise source n_S is concerned, very poor improvements are achieved for the LF pointing error indices, MPE and PDE, while as expected from the preliminary analysis the error contributions at high frequencies is increased, in this case up to 30%.

	σ_{APE}	σ_{MPE}	σ_{RPE}	σ_{PDE}
Plateaus	-78.35%	-89.30%	-78.17%	-87.88%
Ref. Disturbance	-27.03%	-80.06%	-27.02%	-79.51%
Ref. Noise	+32.03%	-0.04%	+32.09%	-0.83%

Table 4.2: Relative increase/decrease in the different pointing error contributions after integral action optimization (plateaus disturbance)

In the following figures, the impact of a plateaus disturbance is graphically illustrated in terms of the different pointing error indices' time-series, to further visualize the improvements achieved with respect to disturbance transients. They are derived by applying the respective window metrics defined in Table 2.2 to the absolute

pointing error time series obtained from numerical simulations, the dashed line represents the standard deviation of the disturbance transient's PEC. The simulations are performed with the Matlab *lsim* function.

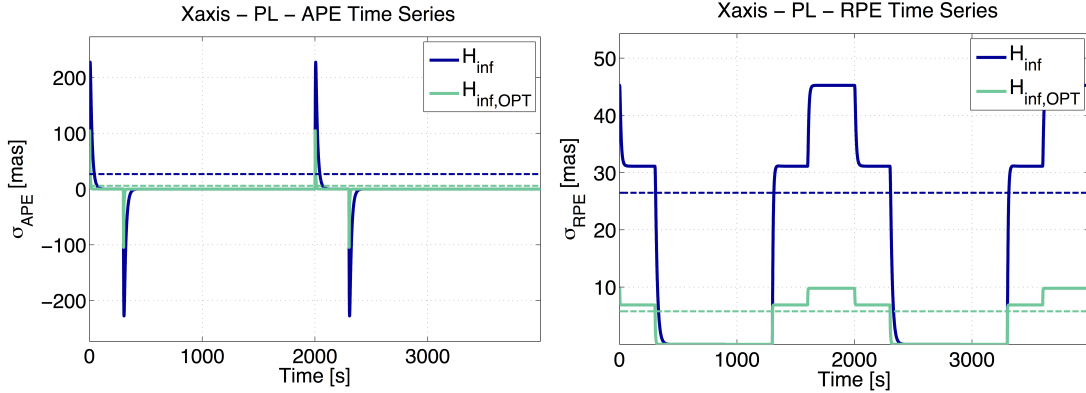


Figure 4.10: Time-series of the plateaus disturbance contribu-
tion on APE

Figure 4.11: Time-series of the plateaus disturbance contribu-
tion on RPE

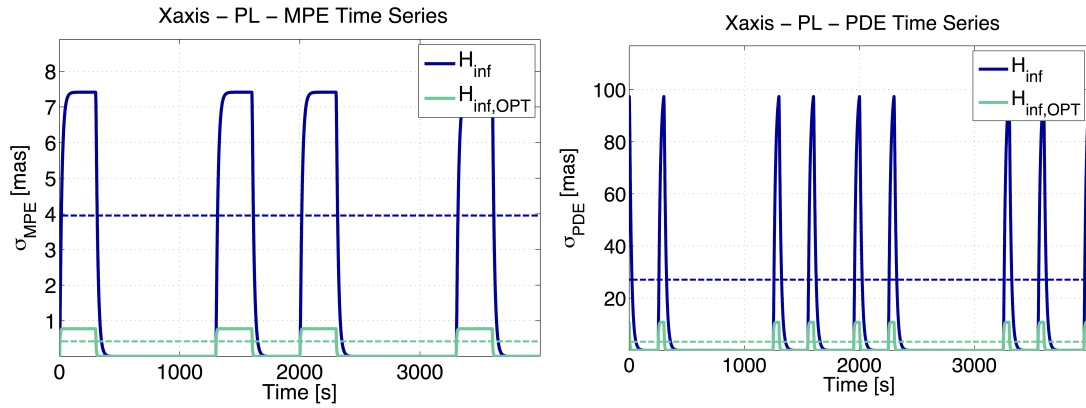


Figure 4.12: Time-series of the plateaus disturbance contribu-
tion on MPE

Figure 4.13: Time-series of the plateaus disturbance contribu-
tion on PDE

4.3.2. Spike Disturbance Case Study

Then results obtained by analytical estimation of the pointing error budget when a spike disturbance waveform is considered are displayed in the Table 4.3. The pointing error indices are reported in terms of standard deviation. The contributions of the different error sources is also presented in this case.

		σ_{APE} [mas]	σ_{MPE} [mas]	σ_{RPE} [mas]	σ_{PDE} [mas]
K_∞	Spike	51.7512	1.3524	51.7335	26.2800
	Ref. Disturbance	15.8139	0.2390	15.8121	4.6076
	Ref. Noise	14.1079	0.6456	14.0931	3.4402
Total		55.9222	1.5175	55.9016	26.9004
$K_{\infty, opt}$	Spike	14.0925	0.21275	14.0909	4.2122
	Ref. Disturbance	11.5393	0.04765	11.5393	0.9441
	Ref. Noise	18.6275	0.64533	18.6163	3.4116
Total		26.0526	0.68116	26.0437	5.5052

Table 4.3: Pointing error budget with respect to a spikes disturbance, (x axis)

Also in this case, from the results obtained several conclusions can be derived and the pointing error budget resulting from the implementation of optimized controller, $K_{\infty, opt}$, is reported in Table 4.4 in relation to the

values obtained when the original controller, K_∞ , is regarded in the calculations. Concerning the reference noise PES's the same considerations made in the previous section still apply. Additionally, as far as the spikes disturbance rejection is considered the relative improvements achieved are smaller compared to the ones obtained in the plateaus case. The reason behind this is that the periodic plateaus disturbance considered in this analysis has a way more low frequency components compared to the spikes profile as illustrated in Figure 3.4. Therefore, since it has already been proved that the lower is the frequency content of the disturbance signal the larger the rejection performance improvements brought by a larger integral bandwidth are, the PEC's of a plateaus torque disturbance are minimized to a greater extent compared to the one of a spikes disturbance.

	σ_{APE}	σ_{MPE}	σ_{RPE}	σ_{PDE}
Spikes	-72.77%	-84.27%	-72.76%	-83.97%
Ref. Disturbance	-27.03%	-80.06%	-27.02%	-79.51%
Ref. Noise	+32.03%	-0.04%	+32.09%	-0.83%

Table 4.4: Relative increase/decrease in the different pointing error contributions after integral action optimization (spikes disturbance)

In the following figures, the pointing error contribution of a spikes disturbance is graphically illustrated in terms of the different pointing error indices' time-series, to further visualize the improvements achieved with respect to disturbance transients. They are derived by applying the respective window metrics defined in Table 2.2 to the absolute pointing error time series obtained from numerical simulations, the dashed line represents the standard deviation of the disturbance transient's PEC. The simulations are performed with the Matlab *lsim* function.

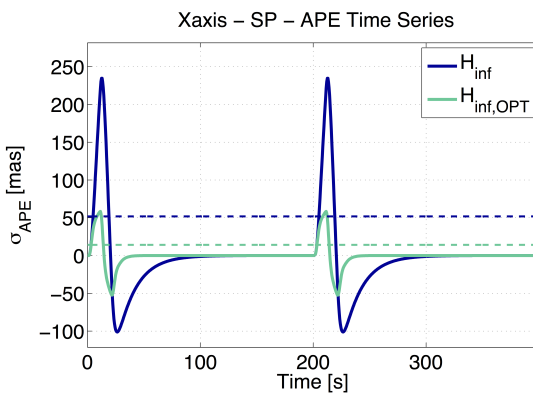


Figure 4.14: Time-series of the spikes disturbance contribu- tion on APE

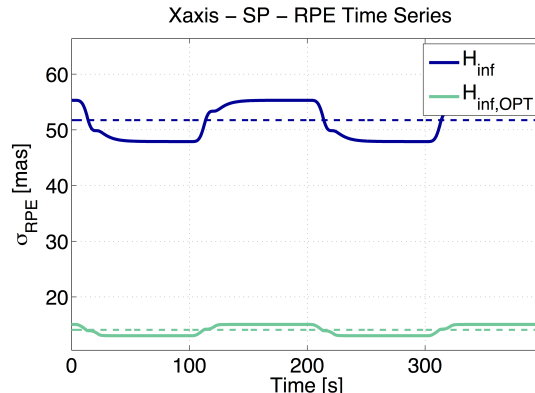


Figure 4.15: Time-series of the spikes disturbance contribu- tion on RPE

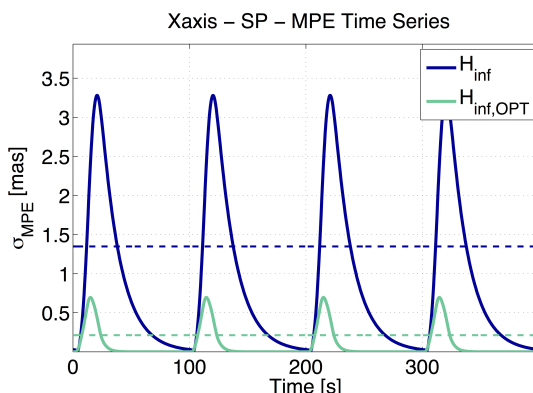


Figure 4.16: Time-series of the spikes disturbance contribu- tion on MPE

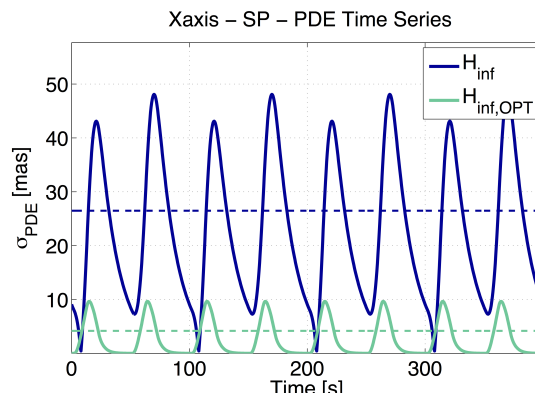


Figure 4.17: Time-series of the spikes disturbance contribu- tion on PDE

4.3.3. Stability Margins

Additionally, stability margins are hereby reported in Table 4.5. As expected, the price to be paid for improved pointing performances is poor stability margins. According to the results obtained, the solution with the optimized integral action greatly impairs the phase margin, which is barely kept above the requirement, this is due to the phase lag that is introduced in the system by the large integral bandwidth, which also affect the gain margin indeed. In addition, the larger integral bandwidth leads the resonance dynamics of the system to be more excited, therefore higher peak value of $S(s)$ and $T(s)$ are indeed obtained.

	GM [dB]	PM [deg]	M_S [dB]	M_T [dB]
K_∞	11.05	56.277	3.02	1.99
$K_{\infty,\text{opt}}$	10.67	34.216	4.72	5.69

Table 4.5: Comparison of the stability margins obtained with the $K_{\infty,\text{opt}}$ and K_∞ control strategies (x axis)

4.3.4. Simulation Results

Eventually, the optimized controller $K_{\infty,\text{opt}}$ has been also implemented in the AOCS simulator of the 2PCD tool, which is used to verify the performance obtained after the control synthesis. The aim here is to prove also numerically that the optimization of the integral bandwidth of K_∞ brings benefit to the AOCS global pointing performance. Results are both provided for the plateaus and spikes disturbance cases in Table 4.6 and both the control solutions are regarded to demonstrate the improvements.

		σ_{APE} [mas]	σ_{MPE} [mas]	σ_{RPE} [mas]	σ_{PDE} [mas]
K_∞	Plateaus	37.7	4.58	35.5	28.4
	Spikes	56.8	1.62	56.5	28.8
$K_{\infty,\text{opt}}$	Plateaus	21.1	0.924	20.8	5.00
	Spikes	24.4	0.695	24.3	5.70

Table 4.6: Results of the pointing error evaluation conducted by means of numerical simulations (x axis)

Results illustrated in Table 4.6 show that pointing performance improvements are achieved in accordance with the analytical estimations conducted in the previous sections. Numerical simulations have been performed considering the nonlinear attitude dynamics, delays and parameters uncertainties that explain the slightly different values. The aim, however, is to verify also numerically the performances improvements brought by the optimal integral action rather than to compare numerical results with analytical estimations.

4.4. Discussion of Results

At the end of this analysis it can be concluded that:

- An integral action is required at an ACS level in order to cope with constant disturbances, otherwise asymptotic disturbance rejection cannot be achieved. Given the fact that friction torque instabilities predominantly impair performance in the low-frequency range, a larger integral bandwidth can help suppressing their contribution to the output pointing error. Furthermore, according to a preliminary analysis a large integral bandwidth provides a faster response and shorter settling time but, on the other hand, it also leads to instability. The optimized integral action introduces an additional phase lag that can greatly impair the stability of the ACS loop. As far as pointing performance is concerned, disturbance transmission is improved while noise rejection is worsened.
- Based on these considerations the integral bandwidth of the controller designed with the 2PCD tool is further optimized with respect to spikes and plateaus disturbance transients. The optimization of the RPE index is however hindered by stability reasons. The first main drawback of this solution is indeed related to the system stability which is very sensitive to changes in the integral bandwidth of the ACS controller, results demonstrates that the phase margin is greatly impaired as well as the closed-loop peak values.

- As far as pointing performance is regarded, the contribution of both plateaus and spikes disturbances is minimized for all the different pointing error indices. In the following figures the overall pointing performance improvements are illustrated with respect to plateaus torque profiles, Figure 4.18, and spikes torque profiles, Figure 4.19, summarizing the pointing error budget analysis performed within the reference case study. The original solution consists in the controller designed with the 2PCD tool K_∞ and it is compared with the performance of the controller where the integral action has been optimized, $K_{\infty,\text{opt}}$.

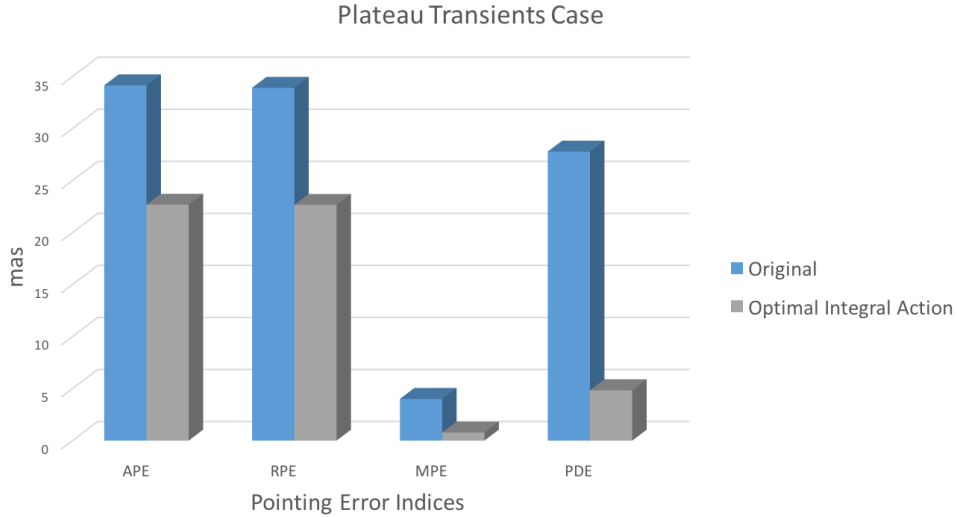


Figure 4.18: Overall pointing performance comparison between $K_{\infty,\text{opt}}$ and K_∞ control strategies, with respect to a plateaus disturbance

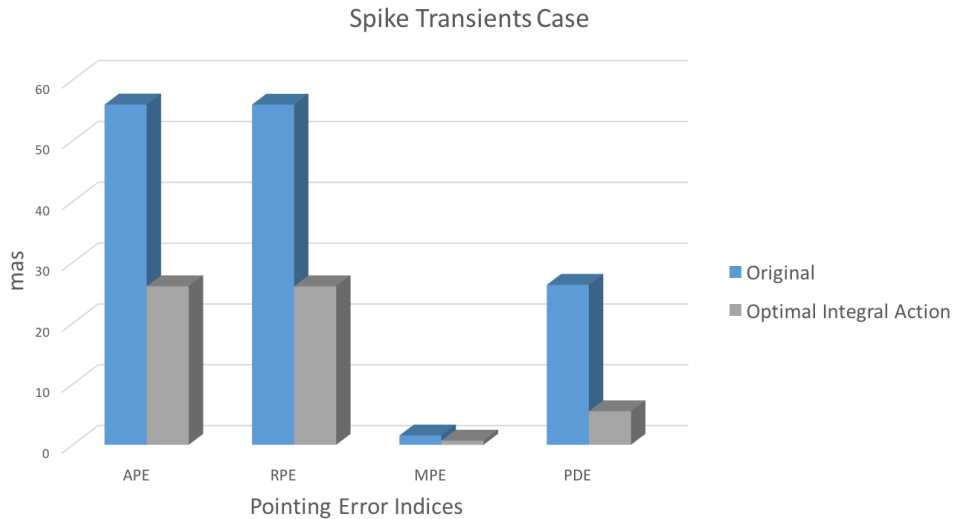


Figure 4.19: Overall pointing performance comparison between $K_{\infty,\text{opt}}$ and K_∞ control strategies, with respect to a spikes disturbance

In both cases, the optimized integral action enhances the system's rejection capabilities of LF disturbances. MPE and PDE indices address the low frequency content of the absolute pointing error, thus they are characterized by greater improvements compared to APE and RPE. On the other hand, as expected from the preliminary considerations, the pointing error contributions of the random noise inputs are increased especially for the indices addressing the high frequency content of the absolute pointing error, APE and RPE. Hence, the second main drawback of this control solution consists in the fact that while disturbance rejection is optimized, noise's influence on the pointing performance is impaired.

5

Design of a Wheel Speed Control Loop

This chapter focuses on a second method that can be implemented in order to handle wheels disturbance transients. The idea consists in adding an inner loop controller to the reference ACS loop, specifically designed to suppress disturbances originating at the reaction wheel level. This solution is currently under study and it is deemed to be a promising alternative but only preliminary studies have been conducted at Airbus DS. In addition, since the practical implementation would require modifications of the actuators' hardware, an agreement with the wheels' supplier has not yet been found, hence the solution it has never been applied yet. Therefore further proves and analysis of the benefits are needed also to derive guidelines for the suppliers.

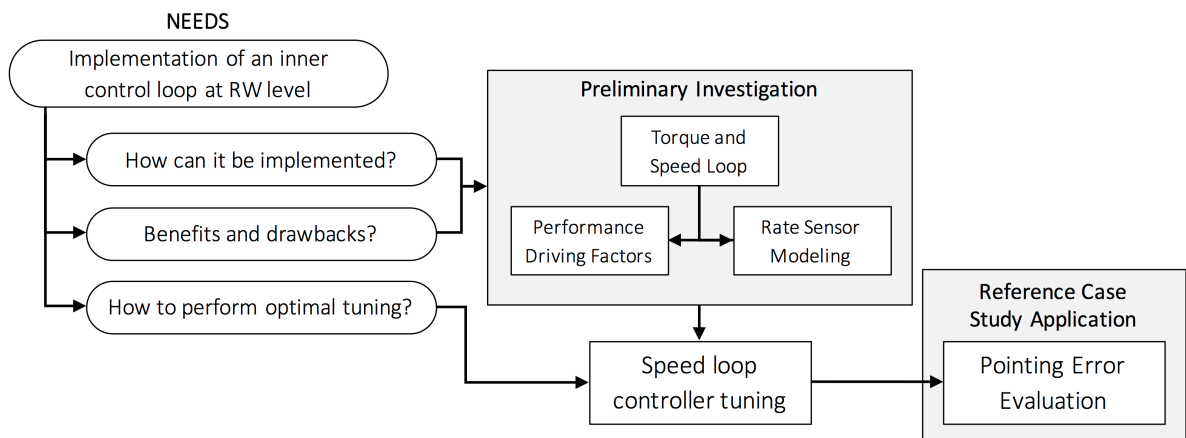


Figure 5.1: Overview of the fifth chapter's contents

In Figure 5.1 the various steps tackled in the following analysis are illustrated. Firstly it has been asked whether this solution can actually bring improvements, which the relative drawbacks are and how it can be implemented. The answers to these questions are provided in Section 5.1. From this preliminary investigation it is concluded that the angular rate sensor (ARS) has a crucial role with respect to both pointing and stability performance, thus in Section 5.2 the working principle of this component is addressed together with the relevant design parameters that are deemed to have a considerable impact on the global loop performance. Eventually a linear model of the sensor is derived in order to be able to address the problem in the same analytical way as done in the previous chapters. Then, in Section 5.3 the speed loop controller is designed following the same reasonings applied within the optimization of the integral action performed in Section 4.2. In conclusion the performance improvements achieved with an wheel speed loop are assessed analytically and compared to the reference case study, results are reported in Section 5.4.

5.1. General

Taking a closer look at the origin of these disturbances, since the reaction wheel technology has a strong commercial appeal, unfortunately only a small number of academic papers describe RW design and control and few are the companies designing and delivering RW's for space applications. However it has been largely demonstrated that these actuators are affected by non-linear behaviors and friction related problems. The electronics is usually equipped with a *current loop*, i.e. an internal control loop that adjusts the commanded current/voltage provided to the brushless DC motor (BLDC) that is spinning the wheel. Additionally, in order to suppress the non-linearities mentioned before, as it has been investigated by [4], [3] and [31], wheels can be equipped with a speed control loop in order to make the wheel follow a given reference speed rate. Nevertheless, the wheels' manufacturers are not providing customized solution for the RWA with this respect, as a result this mitigation method has not yet been practically implemented.

As far as the design of the speed loop is concerned, according to [18], two possibilities are available and they are illustrated in Figure 5.2: a *torque loop* and a *speed loop*, respectively addressed as *T-loop* and *H-loop*.

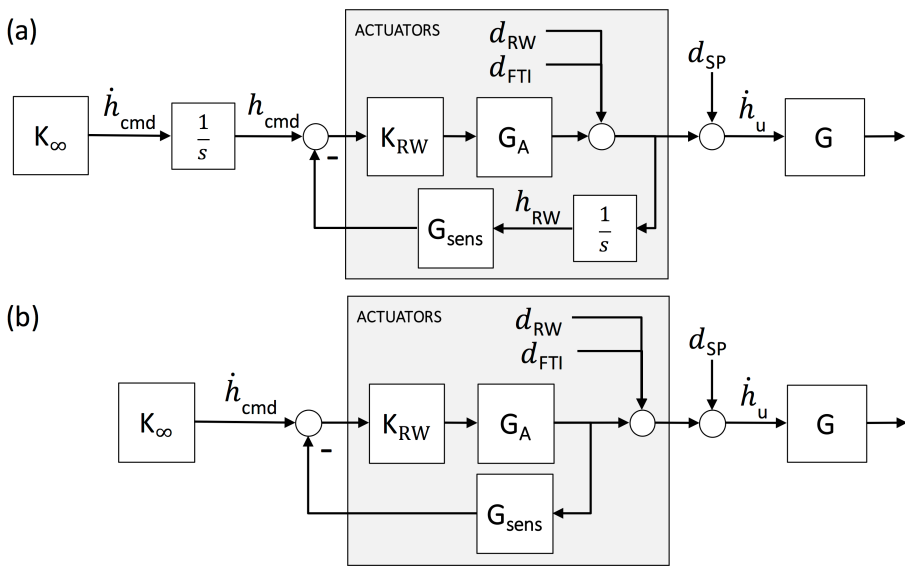


Figure 5.2: Block diagram of two different wheels control loop configurations: *speed loop* (b) and *torque loop* (a)

The T-loop corresponds to the current loop mentioned before, where the torque is controlled comparing the command with the output torque provided by the BLDC motor. However, according to technical notes, this control loop does not take into account disturbances whose sources are friction instabilities occurring in the bearings, since they are introduced in the system "after" the BLDC motor. The H-loop, instead, adjusts the output control torque provided by the reaction wheel measuring its angular rate. With such a control loop the wheel disturbance transients, d_{FTI} , can be handled by the controller, as well as the friction noise, d_{RW} . In this case, an additional integrator has to be added to the outer loop controller and in order to make the control problem consistent an integrator belonging to the system plant G is moved on the speed loop feedback channel. As a result in the following analysis an H-loop is implemented and the main benefits and drawbacks are hereby listed.

- As long as the friction torque instabilities, such as plateaus and spikes, are concerned, it has been showed in Section 3.1 that their contribution is predominantly concentrated in the low-frequency range, whereas the original K_∞ controller is designed to optimize random white-noise transmission. Introducing an inner control loop is a way to solve the classical trade-off, discussed in Section 2.2, concerning noise and disturbance rejection. With a single ACS controller, like in the original control configuration illustrated in Figure 2.5, a high bandwidth controller would lead to great low-frequency disturbances rejection but poor high-frequency noise rejection, while a low bandwidth controller would lead to great HF noise rejection but poor LF disturbance rejection. Additionally, very high bandwidth control solutions cannot be achieved due to practical implementation limits.

If an inner fast controller is introduced right where disturbances are acting, the trade-off can be partially solved. As illustrated in Figure 5.3, given an inner closed-loop H_{RW} with a 2 or 3 times faster bandwidth

than the outer closed-loop H_{ACS} , the HF noise rejection performance is not influenced by the inner loop since the first one has a unitary gain in the frequency range of interest of H_{ACS} . At the same time, the high-bandwidth of H_{RW} can be used to suppress the LF internal friction instabilities to a greater extent.

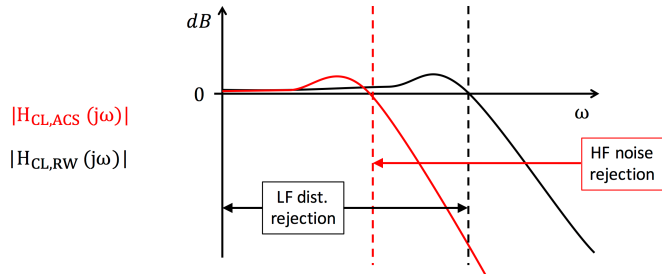


Figure 5.3: Comparison between the outer attitude control loop and the wheel speed loop bandwidths

- The main drawback shows up when the practical implementation of this control solution is concerned. It indeed requires the use of an angular rate sensor in order to measure the rotational speed of the flywheel. In the analysis performed in [4] and [3], this issue was mentioned but not specifically considered in the calculations, while it has been discovered to be a major concern in the preliminary analysis performed in [18].
The sensors used for this purpose can have different working principles and implementations, however they all show in first instance, quantization and resolution problems, as mentioned in [3] and, furthermore, they introduce a delay and an additional noise, [18] and [31].
- Moreover, stability is another major concern when cascade controllers are considered. The stability of the inner loop does not always imply that the outer loop is also stable. Classical tuning methods consist in a first tuning of the inner loop and secondly the tuning of the outer loop. This, however, is not the case, since the outer loop controller has already been generated through the 2PCD tool, and the wheel speed loop controller is, hence, to be designed afterwards.

In conclusion, a fast wheel speed loop is likely to be valid alternative in order to handle plateaus and spikes disturbance profiles. For the reasons explained here above, a *H-loop* is investigated in the following. In order to draw valuable conclusions from the analysis, the impact of the ARS needs to be considered, as a result, based on what is available from the preliminary studies carried out at Airbus DS, a model of the sensor has to be developed. After this, taking advantage of the analytical tool developed in Chapter 3 the inner loop controller K_{RW} can be designed.

5.2. Angular Rate Sensor Model

Sensors for measuring the angular rate of a rotating shaft are widely used in several different engineering fields. They are indeed also used in the automotive and aeronautical sectors as well as inside the hard-disk of computers. Depending on the specific application, performance and power consumption requirements, several sensor typologies are commercially available, according to [9] they can be split in optical, proximity and magnetic encoders. It holds that angular motion sensors based on magnetic field sensing principles prevail on the market due to the their many inherent advantages and sensing benefits [9]. Also in the space engineering domain, as far as rotating mechanisms are concerned, according to [23] Hall sensors are deemed to be the preferred solution for tachometers due to the good accuracy (zero speed measurements are possible), low complexity and low power consumption.

One of the main drawbacks identified in the implementation of a RW speed loop is that the angular rate sensor has a great impact on the performance of the inner loop. Therefore, in order to proceed with the inner loop controller's synthesis also a linear model of the ARS has to be developed in order to be included in the PES transfer analysis.

According to the standard guidelines provided in a technical note for RW dynamic modeling, the tachometer module output is the number of pulses counted by the sensor. A series of magnetic markers or slits are spread around the wheel and when they passes in front of the encoder a modification in the magnetic field is detected

and a pulse is counted. Then, as it is also described in the RWA specifications of a Bradford's wheel, a specific electronic unit equipped with a digital clock is used to process this information and compute the angular rate of the wheel. Given a time window T_S over which a number of pulses n_{ARS} is counted, the actual angular rate can be estimated as follows:

$$\omega_{ARS} = \frac{N_{ARS}\Delta\alpha}{T_S} = \frac{N_{ARS}2\pi}{T_S n_{ARS}} \quad (5.1)$$

where $\Delta\alpha$ is the angular distance from two following sensor markers distributed around the wheel and n_{ARS} is the total amount of them. The sampling time, T_S , and the number of pulses per round, n_{ARS} , are the two variables that indeed determine the performance of the sensor. As a result, the model of a Hall-effect based ARS can be summarized as illustrated in Figure 5.4. Depending on the number of slits and the actual speed of the wheel the magnetic sensor counts the pulses, then the electronics depending on the sampling time adopted provides an estimate of the wheel's speed.

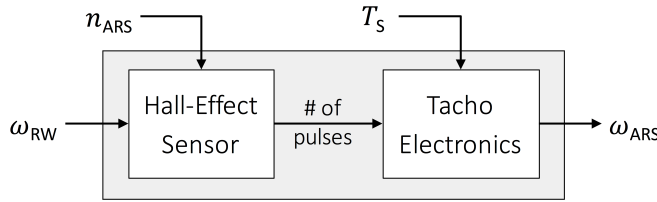


Figure 5.4: Basic functional block diagram of a Hall-effect based rate sensor

According to [18] and [31], the tachometer acts as an additional source of noise to the overall system. Additionally, one of the main drawbacks has been identified in the quantization and resolution error introduced due to sampling, [4] and [18]. Moreover, when sampling is considered a delay is also introduced in the loop as further explained later. The sampling frequency, the delay and the noise level are the three main factors identified to be the drivers of the wheel speed loop performance. For this reason, the tachometer is hereby modeled as the combined action of a sample and hold, a delay and an additional noise source, as represented in Figure 5.5.

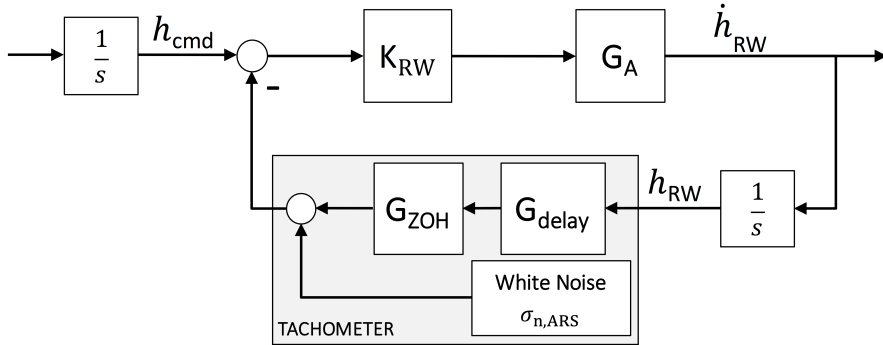


Figure 5.5: Block diagram of the wheel speed loop in the *H-loop* configuration with the linear model of the tachometer

As a result the sensor transfer function can be described analytically and addressed with the standard mathematical tools for pointing error engineering. The delay is described by means of a Padé approximation, while the sampling is described by a zero-order hold (ZOH) as follows:

$$G_{ZOH} = \frac{1}{1 + T_S \frac{s}{2}} \quad (5.2)$$

The working principle based on which pulses are counted is the one of a magnetic encoder. Nevertheless two different ways of translating the sensor output in an estimate of the wheel speed's exist. Both the methods are implemented in the Simulink RW model developed by Airbus DS that contains also an embedded function that models the tachometer. In the following subsections these two methods are thus compared in terms of delay,

refreshment rate and noise. In addition, simulations are performed to provide grounds to the considerations made and to check the compliance of the linear model illustrated in Figure 5.5 with the output of the RW block developed by Airbus DS.

5.2.1. Fixed Delay Mode

According to the Simulink RW model developed in-house, the first method consists in using a fixed time step T_S . Hence the following consideration can be made by observing the simulations output of the Simulink RW model and taking into account the results of the analysis performed in the past, [18]. This method is addressed as *fixed delay mode* because, in contrast with the method proposed later on, the sampling time, T_S , is constant with respect to wheel speed variations.

- First of all the actual spin rate of the wheel is sampled with a frequency $f_{ARS} = 1/T_S$. The estimated rate information is then hold for the all sampling time window T_S . As a result, as it can be observed in Figure 5.6 the output of the ARS model (red line) is characterized by a staircase-like delayed time-varying function.

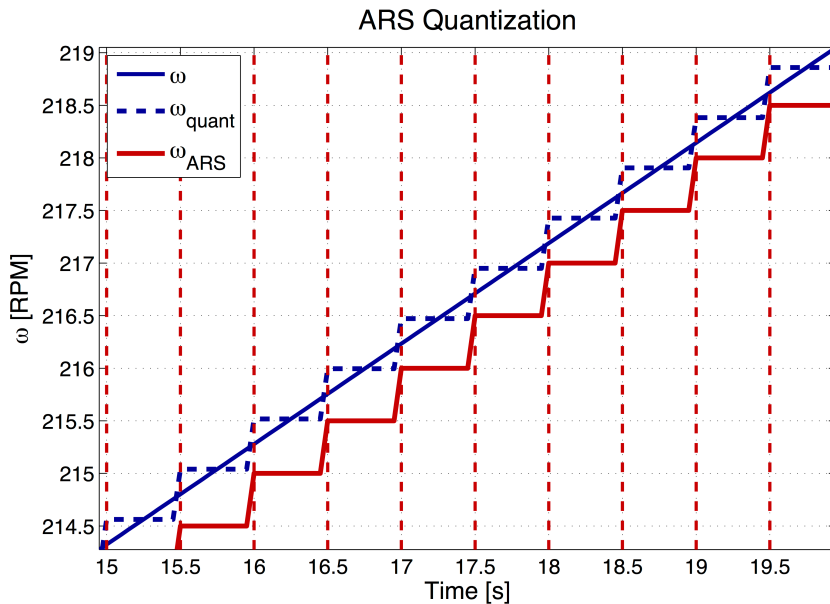


Figure 5.6: Sample & Holder effect and additional delay introduced by the angular rate sensor, according to RW Simulink block output

The behavior is the typical one of a sample and holder, which is the common method to describe sensors and specifically the electronics that is used to convert signals from analog to digital. If no noise is considered, the actual angular rate (solid blue line), when compared to the ARS output of the RW Simulink block (red line), is firstly sampled at the mean value of speed between the two time steps (dashed blue line) and then delayed.

- The delay introduced by the sensor is fixed and it is equal to half the value of the ARS time window selected, $\Delta t_{ARS} = T_S/2$. As is can be noticed in Figure 5.6, given a time window $[t_1, t_2]$, the sensor, after it has performed a measurement at the time instant t_1 , counts the pulses sensed until the time instant t_2 . Hence, an estimate of the RW speed is obtained as follows:

$$\omega_{ARS}(t_2) = \frac{N_{ARS}(t_2)\Delta\alpha}{T_S} \quad (5.3)$$

The estimated rate is an approximation of the wheel's spin rate averaged over the time window. As a result the first effect of the ARS sampling is that the actual value of the spin rate is sampled and delayed of half the value of the ARS time window selected, provided that:

$$\omega_{ARS}(t_2) = \omega \left(\frac{t_2 + t_1}{2} \right) \quad (5.4)$$

To reduce the delay the time window T_S shall be set as small as possible.

- The angular rate estimation is then affected by an error which is due to quantization [3]. The latter can be graphically and intuitively understood looking at Figure 5.7. If two following time steps are considered, depending on the speed of the wheel, an erroneous estimation can be performed by the sensor due to the limited resolution it is characterized by. Further details are provided in Annex C.3.

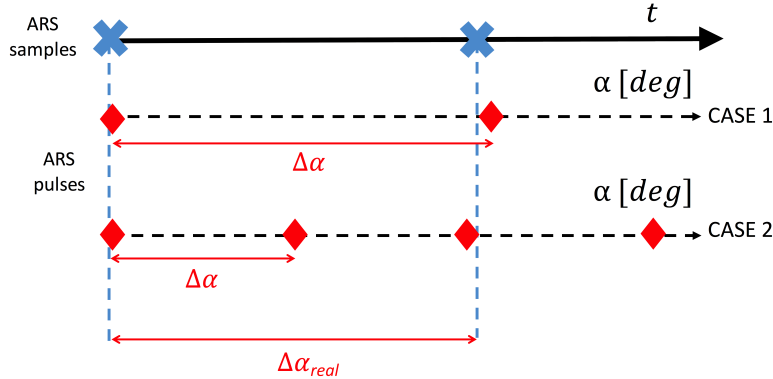


Figure 5.7: Graphical explanation of the resolution error for fixed delay mode algorithm. Case 1 represents the most favorable case scenario. Case 2 represents the worst case scenario

Given an ARS time window, T_S , and a specific number of slits, n_{ARS} the maximum deviation of the ARS output from the actual mean spin rate is equal to one resolution step:

$$\Delta\omega = \frac{\Delta\alpha}{T_S} = \frac{2\pi}{n_{ARS} T_S} \quad (5.5)$$

The validity of this reasoning is then proven comparing the analytical result obtained for the maximum error with simulations. Assuming a time window $T_S = 0.1$ [s] and $n_{ARS} = 300$ it follows:

$$\Delta\omega = \frac{360}{n_{ARS} T_S} = 5 \text{ [deg]} \quad (5.6)$$

Due to the small time step chosen great resolution issues are expected and simulations confirm the analytical result. In the left plot of Figure 5.8 it can be noticed that the ARS output of the RW Simulink block (red line) is affected by a high level of quantization noise and it cannot represent the actual speed properly (blue line). In Figure 5.9 it can be observed that the error generated by the ARS model has a Gaussian-like distribution noise truncated at a maximum value of 5 [deg], as predicted by calculations.

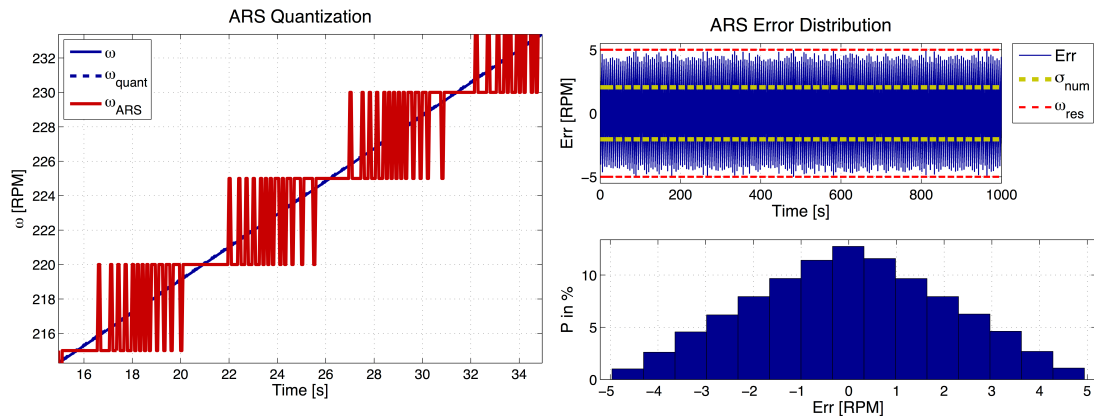


Figure 5.8: Simulation output of the RW Simulink block with fixed delay mode

Figure 5.9: Resolution error distribution with fixed delay mode

Quantization errors are usually characterized by a uniform distribution but this does not hold for the results showed in Figure 5.9 because the error in this case is not due to a proper random process and in addition a specific wheel's rate profile has been considered. Furthermore, the ARS does not handle

constant spin rates, since the sensor output jumps periodically between the two closest quantization levels. In order to reduce the impact of the resolution error hereby described, the quantity ($n_{ARS} T_S$) shall be as large as possible.

- Finally, the behavior of the Hall-effect sensor at low spin rates is considered one of the major concerns, since the frequency at which pulses are counted decreases. Zero speed can be detected and the lower speed detectable equals to $2\pi/n_{ARS}/T_S$ that is equal to the smallest quantization level.

5.2.2. Variable Delay Mode

A second method can be employed in order to derive the spin rate from the Hall-effect sensor pulses. In this case the time between a certain fixed amount of pulses m_{ARS} is measured with the clock. Same analysis has been conducted in order to assess the impact of the use of such algorithm in terms of: refreshment rate, noise, delay and behavior at low speed values. The spin rate is then computed as follows:

$$\omega_{ARS} = \frac{m_{ARS}\Delta\alpha}{T_S} \quad (5.7)$$

This method is addressed as *variable delay mode* because since the number of pulses to be counted is fixed, the sampling time, T_S , and hence the delay vary with respect to the wheel speed.

- In this case a measurement is performed whenever a fixed amount of pulses is detected by the sensor. As a result, the refreshment rate is:

$$f_{ARS} = \frac{1}{T_S} = \left(\frac{m_{ARS}\Delta\alpha}{\omega} \right)^{-1} = \frac{n_{ARS}}{2\pi m_{ARS}}\omega \quad (5.8)$$

Thus, the higher is the density of sensor's slits or markers ($n_{ARS}/2\pi$) the higher is the sampling rate. In addition the refreshment rate increases linearly with respect to the actual speed of the wheel, but it is inversely proportional to the number of pulses considered for each measurement, m_{ARS} .

- Due to the same reasonings explained in the previous case, the delay introduced by the sensor is equal to half the refreshment rate's time interval.

$$\Delta t_{ARS} = \frac{1}{2} \frac{m_{ARS}\Delta\alpha}{\omega} = \frac{m_{ARS}\pi}{n_{ARS}\omega} \quad (5.9)$$

Also the time delay is therefore variable, indeed it gets smaller as the spin rate of the wheel increases. This can be graphically visualized in Figure 5.10 where the ARS sampling time is plotted for an increasing RW spin rate profile.

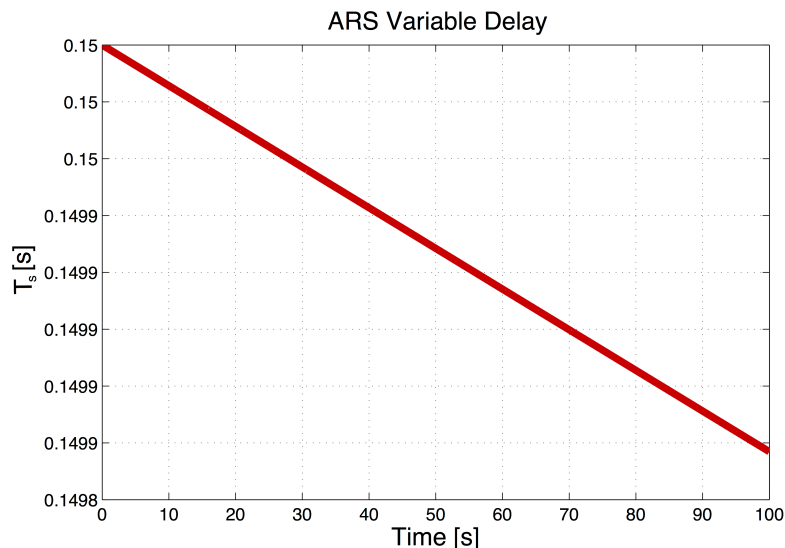


Figure 5.10: Variation of the rate sensor's sampling time with respect to an increasing wheel's rate profile

In this case the delay is proportional to the number of pulses considered for each measurement and inversely proportional to the number of pulses per round of the wheel.

Additionally simulations were performed to verify the sample-and-delay model illustrated in Figure 5.5. From Figure 5.11 it can be observed that, in noise-free conditions, the simulation output (red dots) deviates slightly from the sample-and-delay model (blue dots). This error is somehow periodic and it can be demonstrated to be due to numerical issues, further explanations are provided in Annex C.3. Beside this, the linear model is demonstrated to be compliant with the output of the RW Simulink block.

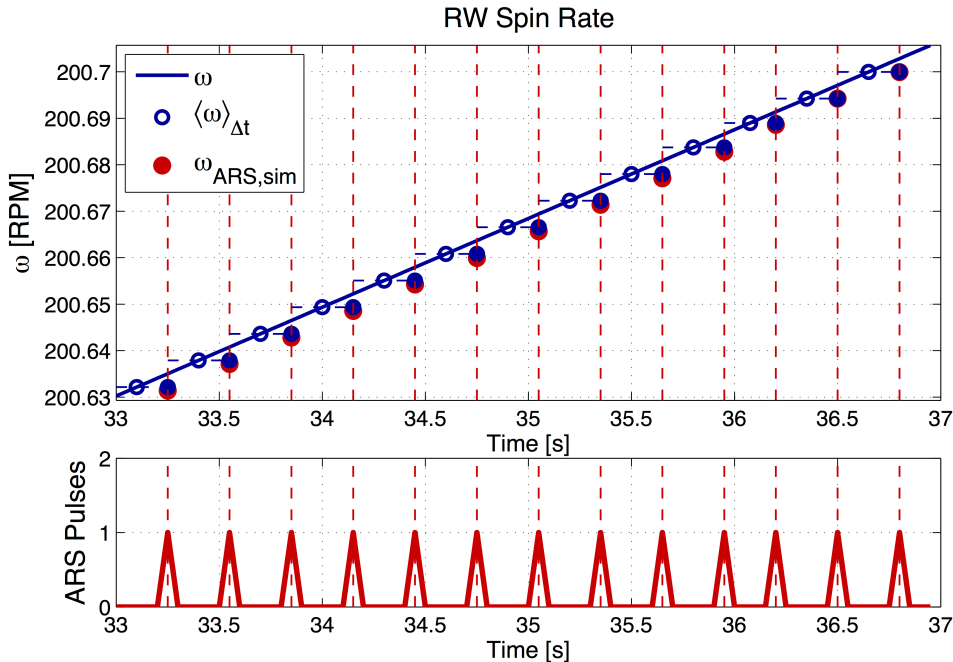


Figure 5.11: Comparison between the RW Simulink model output and the expected noise-free behavior of the rate sensor model

- With this method, the angular displacement measured by the sensor $\Delta\alpha_{\text{ARS}}$ is equal to the actual one $\Delta\alpha_{\text{real}}$, neglecting for the moment the numerical issues mentioned before. However a source of noise exists, as identified by [18], and it is related to the electrical jitter due to the Hall-effect sensor. This introduces an error in the calculation of the time between the tachometer pulses. Let Δt_0 be the actual amount of time passing between two following pulses, an additional delay is added due to jitter.

$$\Delta t = \Delta t_0 + \delta t_j \quad (5.10)$$

With some algebraic steps it can be shown that this is translated in a error on the measured spin rate as follows:

$$\delta\omega = \frac{\delta t_j n_{\text{ARS}}}{2\pi m_{\text{ARS}} + \delta t_j n_{\text{ARS}}\omega} \omega^2 \quad (5.11)$$

According to [18], the jitter noise is in the order of 1 $[\mu\text{s}]$ (3σ). The noise magnitude increases as the refreshment rate and hence also the angular rate increases.

As far as this method is concerned, two variables are to be selected in the design phase: m_{ARS} and n_{ARS} . Given a certain number of magnetic slits on the RW, m_{ARS} shall be as small as possible at low speed, in order to reduce the delay. Hence, $m_{\text{ARS}} = 1$ might sound as a wise choice, however if the speed of the RW increases, the refreshment rate would do so as well but the jitter noise would, in turn, gets larger and larger. This can be observed in Figure 5.12, where an electrical jitter of 1 $[\mu\text{s}]$ is regarded in the calculation of the noise magnitude. The noise level and the delay curves have been evaluated for different values of n_{ARS} that has clearly a considerable impact. In order to solve this trade-off, firstly it has to be reminded that one of the basic assumptions made is that, since dealing with steady state operations, RW's are considered to spin at rates higher than 250 [RPM] to avoid the sub-EHD region, as a result, as it can be seen from Figure 5.12, the delay already reaches reasonable values if $\omega > 250$ [RPM] is considered as the range of interest. Additionally, an algorithm with a variable m_{ARS} could be implemented. The pulses counter can be scheduled splitting the range of angular rate at

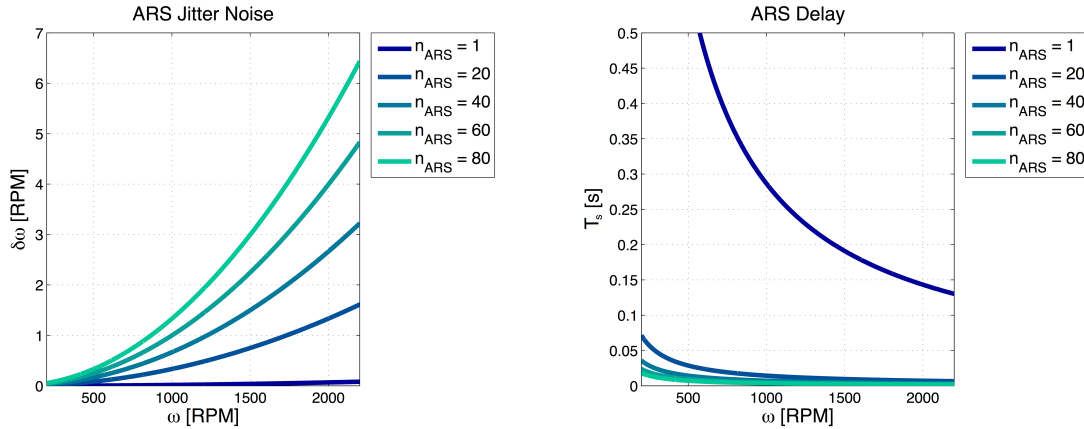


Figure 5.12: Delay and jitter noise generated within the wheel speed loop with a *variable delay mode* implemented in the rate sensor

issue in different slots and assigning an increasing value of m_{ARS} to each slot as the speed increases. In Figure 5.13 the benefit of such solution is visible, both noise and delay can be kept below a certain value required, scheduling properly the values of m_{ARS} .

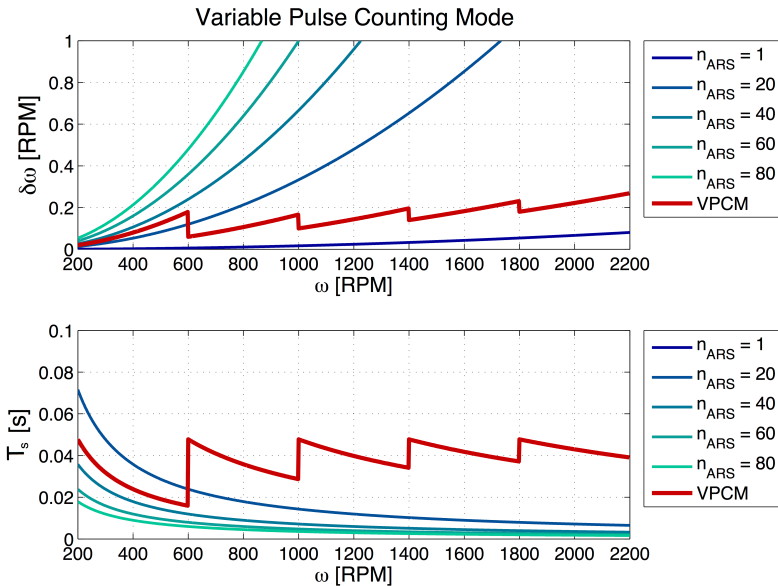


Figure 5.13: Noise and delay performance with variable pulses-counter (VPC) scheduling approach implemented in the rate sensor

The number of pulses per round n_{ARS} can be selected so that at the lower boundary of the speed range considered the delay is below a certain required value. In second instance, both the width of the speed slots and the values of m_{ARS} can be optimized so that the jitter noise and delay remain below the specifications.

5.2.3. Sensor Model Implementation

Eventually, the two methods are compared in order to select the one more suitable for the purpose. In Figure 5.14 the strengths and weaknesses of the two methods, already discussed in details previously, are summarized. Additionally numerical results are provided. In the *fixed-delay* case two design solutions are provided, one aimed to minimize the delay introduced by the sensor and the other one to minimize the noise. While in the *variable-delay* case performance achievable with the variable pulse-counter (VPC) scheduling are provided. The noises due to quantization and electrical jitter described in the previous sections are hereby assumed to have a white-noise signal behavior, characterized by a standard deviation (3σ) determined by the expressions of the maximum error derived before. This is a very conservative approach that is deemed to be sufficient for a preliminary analysis, as a detailed model of the sensor is not yet available.

	DELAY	NOISE
BENEFITS	Small delay can be set	Not affected by electrical jitter
DRAWBACKS	Resolution gets worsened	Great errors due to resolution
$\sigma_n = 2.5 \text{ RPM}$ $\Delta t_{ARS} = 0.1 \text{ s}$	$\sigma_n = 0.3 \text{ RPM}$ $\Delta t_{ARS} = 0.75 \text{ s}$	
VARIABLE DELAY	DELAY	NOISE
BENEFITS	Can be scheduled for high rates	Not affected by resolution error
DRAWBACKS	High delay when running slow	Affected by electrical noise jitter
PULSES COUNTER SCHEDULING		
$\sigma_n = 0.2 \text{ RPM}$ $\Delta t_{ARS} = 0.05 \text{ s}$		

Figure 5.14: Angular rate sensor estimation algorithms comparison

The first method is affected by a trade-off between delay and resolution error. One way to further improve both performance would be to increase the number of pulses per round n_{ARS} , however there is a limitation due to the practical implementation of very large number of magnetic markers. Additionally, the closer they are between each other, the more is the magnetic interference they can be affected by. When the second method is addressed it has been found out that with VPC scheduling the noise-delay trade-off can be solved. Better results are then achieved, with an even smaller amount of pulses per round required; e.g. the performance values reported in Figure 5.14 for the *fixed-delay* case are obtained with 240 pulses per round, while when the *variable-delay* case with the scheduling is concerned, only 30 pulses per round are needed in order to obtain results that are clearly surpassing the first method's ones.

Simulations are then performed in order to compare the sensor model illustrated in Figure 5.2 with the ARS output of the RW block from Airbus DS. The jitter noise is not considered since not implemented in the RW block, additionally a slowly varying RW speed has been addressed in order to avoid great delays variations. This is because the model depicted in Figure 5.2 considers only a constant delay, it is indeed aimed to be used later for worst-case scenario analysis where the maximum delay possible is considered. Simulations demonstrate the sample-and-delay model (dark dots) compliance with the output of the in-house RW Simulink block (light dots), as it is can be graphically observed in in Figure 5.15.

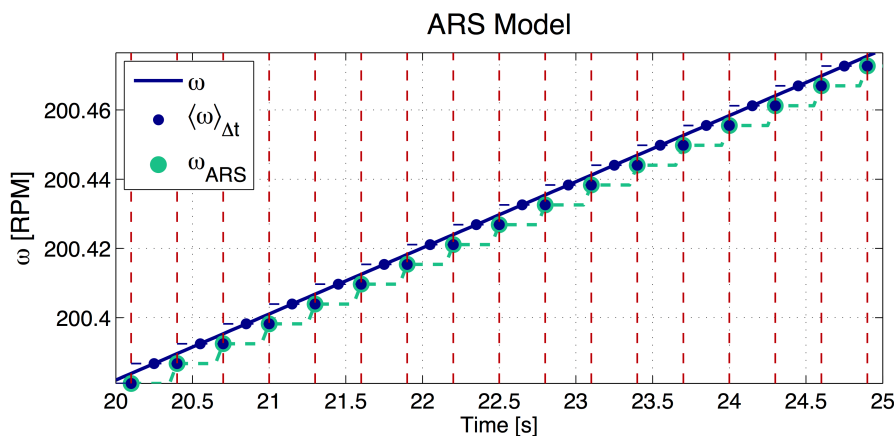


Figure 5.15: Comparison of the tachometer linear model (dark dots) and the RW Simulink model output (light dots)

5.3. Wheel Speed Loop Design

The inner loop's controller design has been performed investigating three different solutions: a P controller, a PI controller and a PD controller. Like the approach used for the tuning of the integral action in Chapter 4, also in this case the tuning of the different coefficients has been performed aiming to minimize a single pointing

error indices, specifically the RPE. As it has been done in the optimization of the integral action, also stability margins are taken into account in the synthesis process, but, in addition to those already mentioned also the delay margin (DM) is addressed. This is because, in the preliminary analysis it has been showed that the total delay is a major concern for the stability of an inner speed loop. However, analytical preliminary considerations on the impact of the inner controller on the outer loop stability margins are not provided as it has been done in the previous chapter, the stability analysis of cascade controller is complex and it is beyond the purpose of this thesis. In this approach, only the compliance with stability requirement is checked during the tuning of the controller. The parameters used for the deterministic disturbances are the same used in the previous chapter, thus they are listed in Table A.3, while the stability parameters in Table A.4. Concerning the ARS, a sampling time of 0.1 [s] and a electrical jitter noise standard deviation (3σ) of 10 [mrad/s] are considered, according to the results that can be obtained exploiting the VPC scheduling algorithm.

In order to take advantage of the PES transfer analysis to optimize the controller, the transfer functions, from the various error sources to the output pointing error, have now to be calculated given the new control problem configuration. Fusing together Figure 5.5 and Figure 2.5, the AOCS loop can be restructured as illustrated here below.

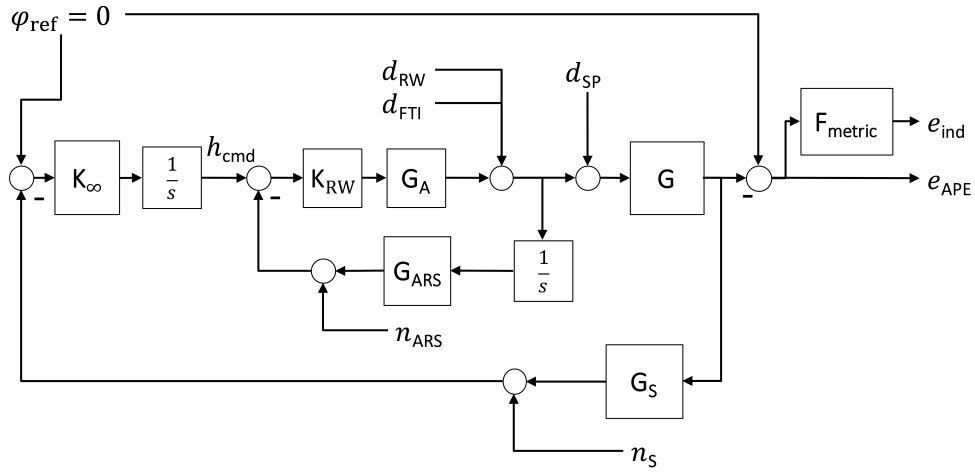


Figure 5.16: ACS block diagram with the wheel speed loop implemented (SISO)

The relevant noise and disturbance transmission transfer functions are then derived accordingly to the system in Figure 5.16. In this case, the noise introduced by the tachometer, n_{ARS} , is treated as an additional white noise source. The transfer functions from the different noises and disturbances to the absolute pointing error are thus reported in Table 5.1. Pointing error transfer analysis can be then performed to evaluate the controller performance as explained in Section 3.2.

	e_{APE}
n_S	$H_{n,AOCS}(s) = \frac{K_\infty G K_{RW} G_A}{s + G_A K_{RW} G_{ARS} + G G_A K_{RW} K_\infty G_S}$
n_{ARS}	$H_{n,RW}(s) = \frac{s G G_A K_{RW}}{s + G_A K_{RW} G_{ARS} + G G_A K_{RW} K_\infty G_S}$
d_{SP}	$H_{d,AOCS}(s) = -\frac{G(s + G_A K_{RW} G_{ARS})}{(s + G_A K_{RW} G_{ARS}) + G G_A K_{RW} K_\infty G_S}$
d_{FTI}	$H_{d,RW}(s) = -\frac{s G}{s + G_A K_{RW} G_{ARS} + G G_A K_{RW} K_\infty G_S}$
d_{RW}	$H_{d,RW}(s) = -\frac{s G}{s + G_A K_{RW} G_{ARS} + G G_A K_{RW} K_\infty G_S}$

Table 5.1: Transfer function from the different input noise/disturbances (rows) to the absolute pointing error index

The proportional controller, even though the impact of plateaus and spikes on pointing performance is decreased, does not provide safe stability margins. The GM is right close to the requirement of 6 dB, while the sensitivity peak is well beyond the requirement. As a result, in order to achieve higher stability margins PI and PD controller solutions have been considered. However the final choice is a PD controller, for several reasons.

It has already stressed that the large delay introduced by the ARS make the inner loop very sensitive to additional delays, with this respect a PI controller introduces a further delay in the loop, slowing down the system even more. A PI controller has indeed a negative impact on both the stability and the speed of the response of the system. It is mostly used in situations where the speed of the system is not an issue, which this is not the case, since a high bandwidth is aimed to decouple the inner loop from the outer loop. In second instance, adding an integral action consists in considering the wheel position as a control variable, while it is the angular acceleration to be actually controlled, therefore a PD is more suitable. Furthermore, since the objective is to achieve a fast inner loop, so that LF disturbances can be suppressed, a PD controller provides a larger bandwidth. As a result, the PD coefficients have been optimized by trial-and-error procedure as done in Section 4.3. The minimization of the RPE index has been considered as the driving objective, even though stability margins have been taken into account. In Figure 5.17 the last step of the derivative coefficient tuning is illustrated.

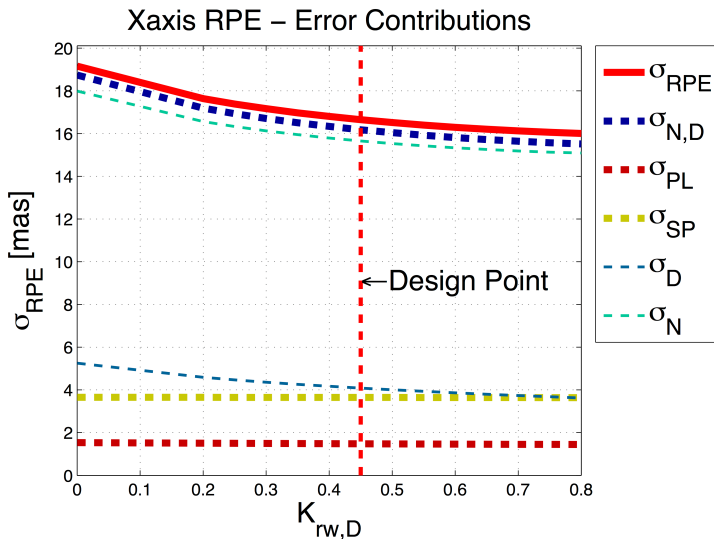


Figure 5.17: RPE budget for different values of the derivative coefficient (x axis)

As expected it provides more robustness with respect to the phase margin and as the inner loop's bandwidth is increased the random noise error rejection capability is improved, Figure 5.17. This is because the larger is the separation between the two loops' bandwidths the lower is the peak value of the sensitivity function, Figure 5.18. The impact of the derivative gain on disturbance transients is instead minimum since they are suppressed already by the proportional gain.

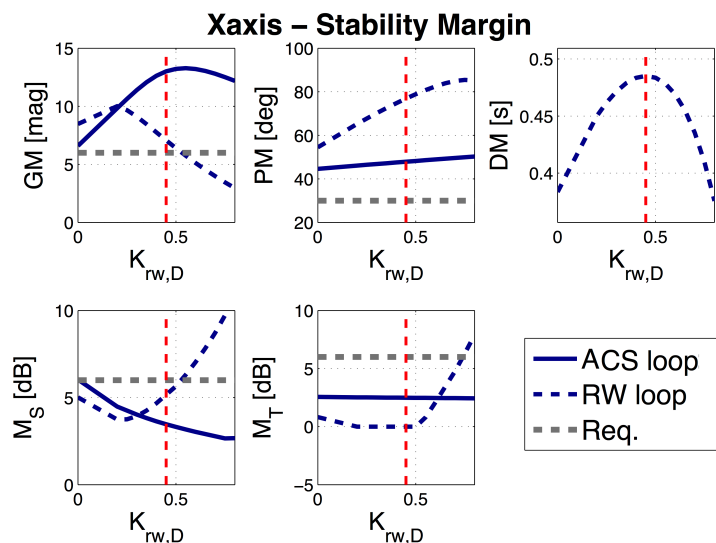


Figure 5.18: Stability margins for different values of the derivative coefficient (x axis)

Due to the high sensitivity of the inner loop to system delays, pointing performance has been slightly sacrificed in order to maximize the delay margin as illustrated in Figure 5.18. Eventually a proportional gain $K_p = 2.5$ and derivative gain $K_d = 0.45$ have been selected for the x axis. Further details about the comparison between a P, PD and PI controllers are provided in the Annex C.4. Eventually, the control system obtained is analyzed with respect to the considerations made at the beginning of the chapter. In order to do this the characteristic closed-loop transfer functions of the system with the additional speed loop are plotted in Figure 5.19 (solid lines) and compared with the reference case study (dashed lines).

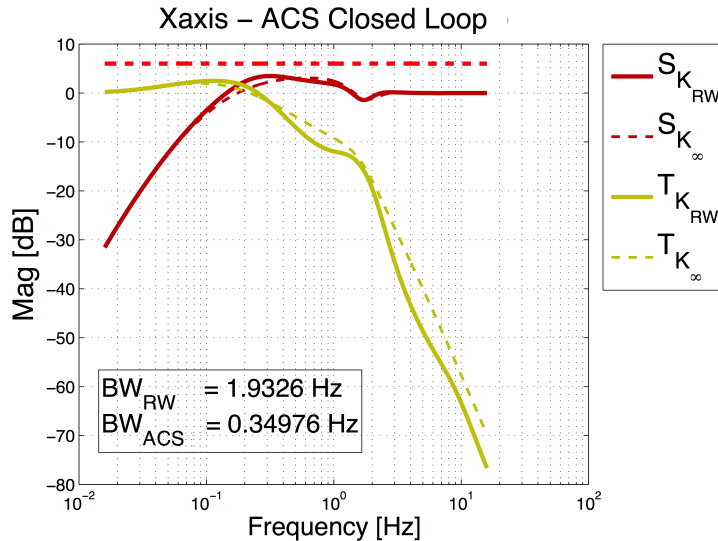


Figure 5.19: ACS closed-loop transfer function comparison without wheel speed loop (dashed lines) and with wheel speed loop (solid line)

It can be concluded that a faster inner loop has been designed (the RW loop bandwidth is indeed 5 times higher than the ACS loop's one). For this reason, the characteristic transfer functions of the ACS loop are almost unaltered if compared to the reference case. In Figure 5.20, instead, noise and disturbance transfer functions are plotted with respect to the two control loops: the inner speed loop (red line) and outer global ACS loop (yellow line). As far as the last one is considered the transfer functions of the reference case study are also illustrated (dashed yellow line). First of all, it can be observed again that noise and disturbance transmission performances are not modified at the ACS level if a wheel speed loop is implemented. Then, from the top plot of Figure 5.20 it can be noticed that the disturbance rejection capabilities are improved at a RW speed loop level in the low-frequency range. The disturbance transfer function, when the wheel speed loop is considered, provides better performance at low frequencies due to its negative slope as $\omega \rightarrow 0$.

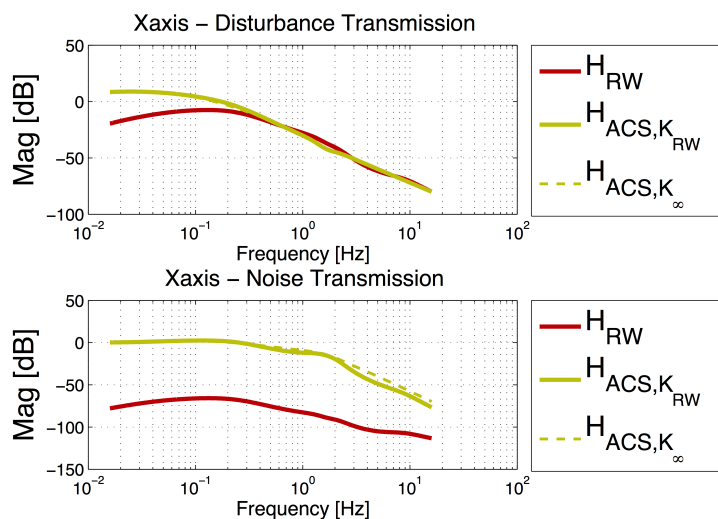


Figure 5.20: Noise and disturbance transmission comparison through the ACS loop (yellow lines) and the wheel speed loop (red lines)

A sensitivity analysis is then performed in order to assess the impact of the ARS characteristics on the stability and performance of the overall system. An increasing value of the sampling time has a direct impact on the stability of the control system: for a sampling time larger than 0.5 [s] the ACS system becomes indeed unstable. As far as the noise due to electrical jitter is concerned, the greater it is, the higher also its contribution to the pointing error indices is. Therefore, by means of the analytical tool a PES transfer analysis can be performed for an increasing level of ARS noise variance. In Figure 5.21 the rate sensor noise, n_{ARS} , contribution is plotted for different values of increasing jitter error and statistically added to the ACS measurements noise, n_S , to obtain the overall noise contribution to the RPE. If provided with a requirement for the RPE index, a pointing error budget analysis can be performed and a maximum pointing error allocation can be derived for the ARS noise (horizontal dashed red line) and then a maximum value of ARS jitter error allowed can be inferred (vertical dashed red line). An example of the process is illustrated in Figure 5.21. Given the different PEC's of external and RW disturbances and measurements noise, the RPE value is compliant with a requirement of 30 [mas] only if $\sigma_{n,ARS} < 40[\text{mrad/s}]$.

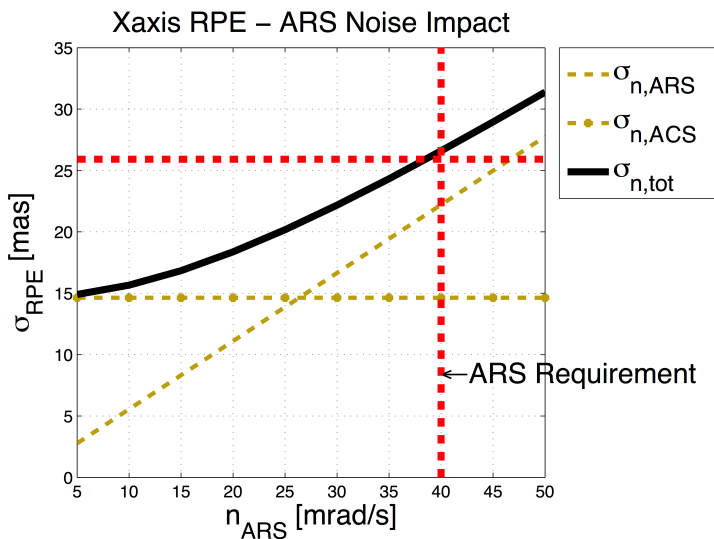


Figure 5.21: Derivation of the maximum electrical jitter noise allowed to the angular rate sensor

5.4. Pointing Performance Evaluation

Eventually, in order to verify the performance improvements brought by the wheel speed loop, a pointing error evaluation analysis has been performed. The pointing error budget is estimated both for the controller designed by the 2PCD Tool, K_∞ , and for the controller with the wheel speed loop, $K_{\infty,RW}$. Improvements can be then verified comparing the results.

The different error contributions are reported in order to investigate the impact of the control solution proposed on the transmission of the different error sources. Plateaus and spikes disturbances are addressed separately since from the lesson learned from past missions the two transient profiles have different origins and therefore occur in different situations.

5.4.1. Plateaus Disturbance Case Study

Numerical results obtained by analytical estimation of the pointing error budget when a plateau disturbance waveform is considered are displayed in the Table 5.2. The pointing error indices are reported in terms of standard deviation. The contributions of plateaus, d_{FTI} , reference measurement noise, n_S , and reference disturbances (RW friction noise, d_{RW} , and solar pressure noise, d_{SP}) to the different pointing error indices are reported. Additionally when the wheel speed loop is considered also the ARS noise, n_{ARS} , is included in the budget.

From the results obtained several considerations can be made, specifically looking at Table 5.3 where the pointing error budget resulting from the implementation of the wheel speed loop, $K_{\infty,RW}$, is expressed as percentage of the reference case study results, K_∞ . Compared to the performance obtained in the previous chapter, first of all it can be noticed that the impact of the plateaus torque is even further minimized, and in addition also

		σ_{APE} [mas]	σ_{MPE} [mas]	σ_{RPE} [mas]	σ_{PDE} [mas]
K_∞	Plateaus	26.7701	3.9499	26.4771	27.1707
	Ref. Disturbance	15.8139	0.2390	15.8121	4.6076
	Ref. Noise	14.1079	0.6456	14.0931	3.4402
Total		34.1431	4.0095	33.9069	27.7780
$K_{\infty,RW}$	Plateaus	1.4781	0.0216	1.4780	0.4170
	Ref. Disturbance	4.0868	0.0114	4.0867	0.2280
	Ref. Noise	14.6518	0.6457	14.6376	3.4432
	ARS Noise	5.5524	0.0142	5.5524	0.2834
Total		16.2601	0.6463	16.2473	3.4874

Table 5.2: Pointing error budget with respect to a plateaus disturbance, (x axis)

the contribution of random reference disturbances is reduced. The latter holds because the RW friction noise, which is dominating the solar pressure disturbance, is inside the wheel's speed loop and hence its low frequency content particularly is better rejected. In addition, the second benefit is that the measurement noise contribution is only slightly affected demonstrating that the fast bandwidth of the inner loop can allow the measurements noise transmission characteristics be almost unaltered. On the other hand, the angular rate sensor introduce a further noise source. All in all, each pointing error index is greatly improved, as far as LF disturbances are addressed better results are obtained within the LF error metrics, MPE and PDE, whereas if HF disturbance and noise sources are concerned better results are obtained within the HF error metrics, APE and RPE, compared to the previous mitigation strategy investigated.

	σ_{APE}	σ_{MPE}	σ_{RPE}	σ_{PDE}
Plateaus	-94.48%	-99.45%	-94.42%	-98.46%
Ref. Disturbance	-74.16%	-95.23%	-74.15%	-95.05%
Ref. Noise	+3.85%	+0.01%	+3.86%	+0.09%

Table 5.3: Relative increase/decrease in the different pointing error contributions after the implementation of a wheel speed loop (plateaus disturbance)

In the following figures, the pointing error contribution of a plateaus disturbance is graphically illustrated in terms of the different pointing error indices' time-series, to visualize the improvements achieved with respect to disturbance transients. They are derived by applying the respective window metrics defined in Table 2.2 to the absolute pointing error time series obtained from numerical simulations, the dashed line represents the standard deviation of the disturbance transient's PEC. Simulations are performed with the Matlab *lsim* function.

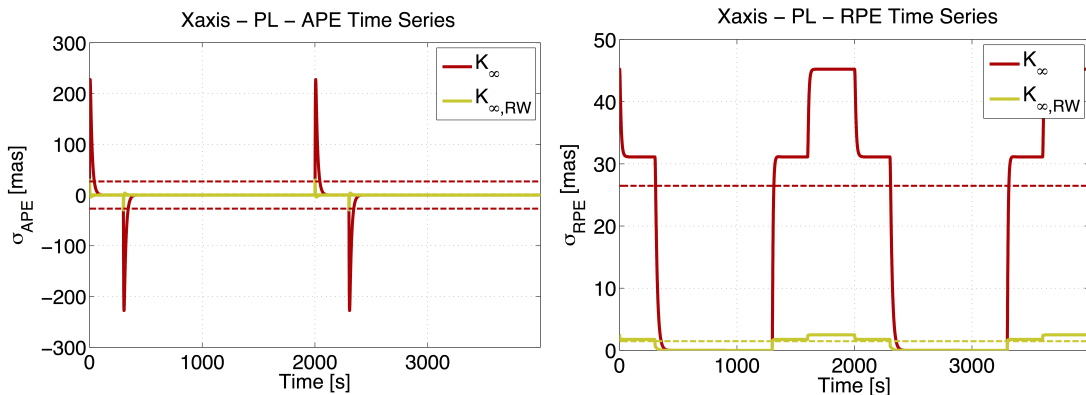


Figure 5.22: Time-series of the plateaus disturbance contribu-

Figure 5.23: Time-series of the plateaus disturbance contribu-

tion on APE

tion on RPE

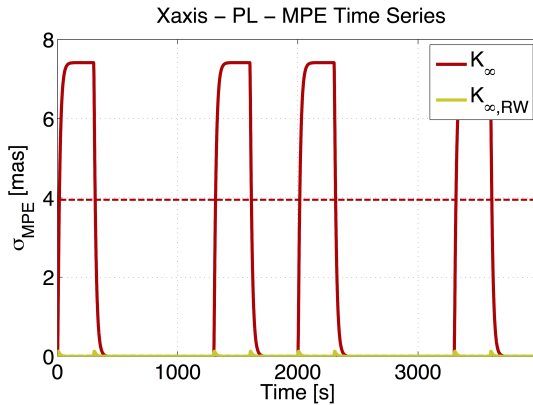


Figure 5.24: Time-series of the plateaus disturbance contribution on MPE

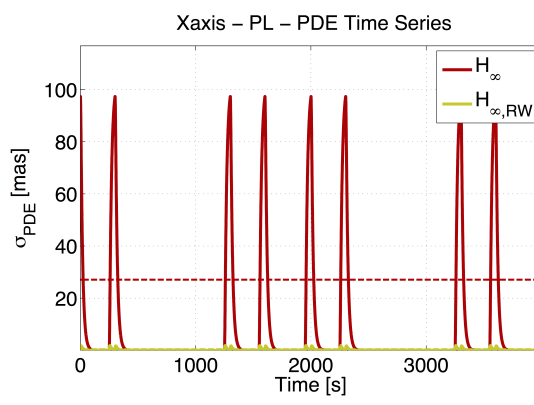


Figure 5.25: Time-series of the plateaus disturbance contribution on PDE

5.4.2. Spike Disturbance Case Study

Then, results obtained by analytical estimation of the pointing error budget when a spike disturbance waveform is considered are displayed in the Table 5.4. The pointing error indices are reported in terms of standard deviation. Also in this case the contribution of different error sources has been specifically addressed.

	σ_{APE} [mas]	σ_{MPE} [mas]	σ_{RPE} [mas]	σ_{PDE} [mas]
K_∞	Spikes	51.7512	1.3524	51.7335
	Ref. Disturbance	15.8139	0.2390	15.8121
	Ref. Noise	14.1079	0.6456	14.0931
	Total	55.9222	1.5175	55.9016
$K_{\infty,RW}$	Spikes	3.6491	0.0419	3.6489
	Ref. Disturbance	4.0868	0.0114	4.0867
	Ref. Noise	14.6518	0.6457	14.6376
	ARS Noise	5.5524	0.0142	5.5524
	Total	16.5989	0.6473	16.5862

Table 5.4: Pointing error budget with respect to a spikes disturbance, (x axis)

The same considerations made for the plateaus disturbance case apply also here. In addition it can be also observed in Table 5.5 that the spikes disturbance contributions are minimized to a slightly smaller extent compared to the plateaus disturbances. The reason is that, as illustrated in Figure 5.20, the major improvements with respect to disturbance transmission are brought in the low frequency domain and the spikes torque profile's energy is distributed over a wider spectrum compared to the plateaus disturbance.

	σ_{APE}	σ_{MPE}	σ_{RPE}	σ_{PDE}
Spikes	-92.95%	-96.90%	-92.95%	-96.78%
Ref. Disturbance	-74.16%	-95.23%	-74.15%	-95.05%
Ref. Noise	+3.85%	-0.01%	+3.86%	-0.09%

Table 5.5: Relative increase/decrease in the different pointing error contributions after the implementation of a wheel speed loop (spikes disturbance)

In the following figures, the pointing error contribution of a spikes disturbance is graphically illustrated in terms of the different pointing error indices' time-series, to further visualize the improvements achieved with respect to disturbance transients. They are derived by applying the respective window metrics defined in Table 2.2 to the absolute pointing error time series obtained from numerical simulations, the dashed line represents the standard deviation of the disturbance transient's PEC. Simulations are performed with the Matlab *lsim* function.

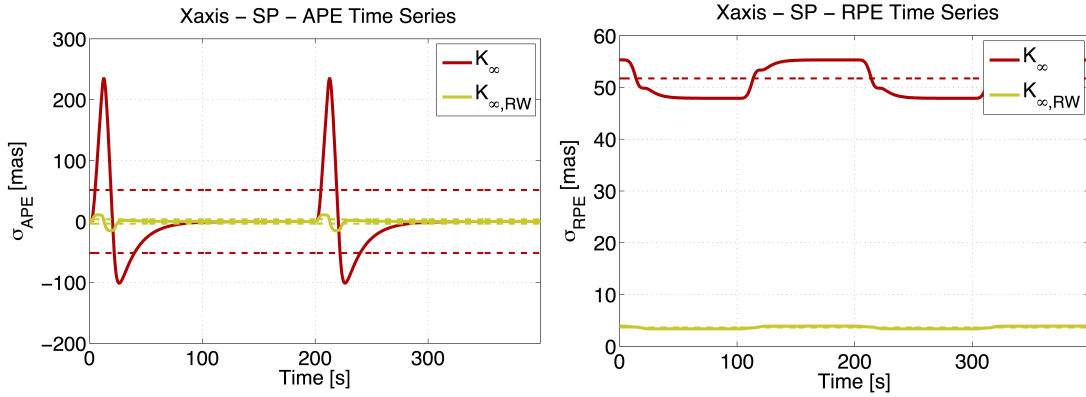


Figure 5.26: Time-series of the spikes disturbance contribution on APE

Figure 5.27: Time-series of the spikes disturbance contribution on RPE

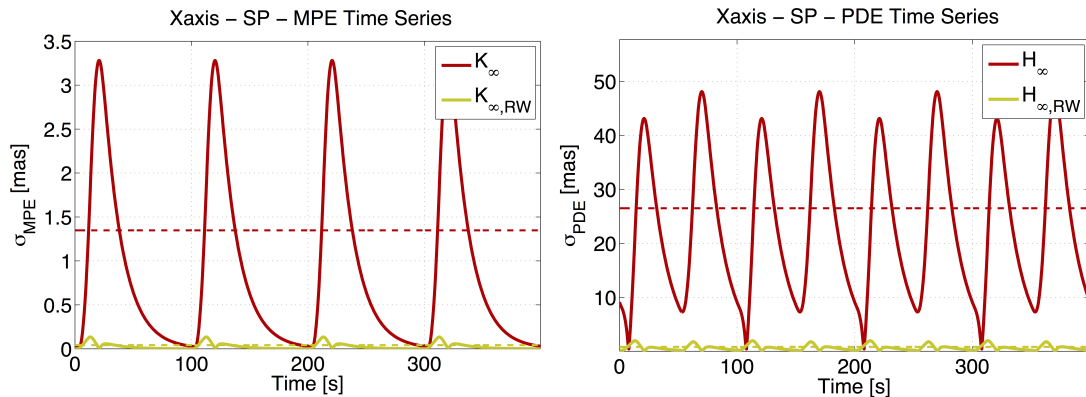


Figure 5.28: Time-series of the spikes disturbance contribution on MPE

Figure 5.29: Time-series of the spikes disturbance contribution on PDE

5.4.3. Stability Margins

Additionally, stability margins are hereby reported in Table 5.6. It can be observed that the gain margin is improved, while the rest of the margins considered are impaired with respect to the reference case study. However, compared to the first solution investigated the impact on stability margins is considerably smaller.

	GM [dB]	PM [deg]	M_S [dB]	M_T [dB]
K_∞	11.05	56.277	3.02	1.99
$K_{\infty,RW}$	13.00	47.889	3.47	2.49

Table 5.6: Comparison of the stability margins obtained with the $K_{\infty,RW}$ and K_∞ control strategies (x axis)

As already mentioned above, given the complexity of a cascade control system and especially if the design of the inner loop is performed after the synthesis of the outer loop controller, to predict and explain analytically how the different stability margins vary with respect to the speed loop controller's gains requires complex mathematical tools. This analysis is beyond the purpose of this thesis also because the focus is on the system pointing performance, despite this stability margins have been still taken into account in the inner loop controller tuning. A further step would indeed consist in a more detailed analysis about how stability is affected when considering a nested controller in the ACS loop.

5.4.4. Simulation Results

Eventually, also in this case the controller with the wheel speed loop, $K_{\infty,RW}$, has been implemented in the AOCS simulator of the 2PCD tool. The aim is to verify the performance improvements brought by the design of this inner loop also in the simulation environment. Results are both provided for the plateaus and spikes

disturbance cases in Table 5.7 and the control strategy derived in this chapter is compared with the results obtained when only the reference controller, K_∞ , is regarded.

		σ_{APE} [mas]	σ_{MPE} [mas]	σ_{RPE} [mas]	σ_{PDE} [mas]
K_∞	Plateaus	37.7	4.58	35.5	28.4
	Spikes	56.8	1.62	56.5	28.8
$K_{\infty,RW}$	Plateaus	15.9	0.645	15.9	3.42
	Spikes	16.3	0.648	16.4	3.53

Table 5.7: Results of the pointing error evaluation conducted by means of numerical simulations (x axis)

Results illustrated in Table 5.7 show that pointing performance improvements are achieved in accordance with the analytical estimations conducted in the previous sections. Numerical simulations have been performed considering the nonlinear attitude dynamics, delays and parameters uncertainties that explain the slightly different values. The aim is indeed to verify also numerically the performances improvements brought by the control strategy rather than to compare numerical results with analytical estimations.

5.5. Discussion of Results

At the end of this analysis it can be concluded that:

- According to the preliminary investigation the implementation of a wheel speed loop seems to be a valid alternative solution to handle disturbance transients generated by RW's. The design of a *faster* inner loop would allow to specifically suppress the low-frequency disturbance at issue, solving the trade-off between disturbance and noise rejection capabilities that exists if a single controller is implemented in the ACS loop. However, still some drawbacks exist: the noise and delays introduced by the angular rate sensor influence crucially the controller performances.
- For the latter reasons, some efforts have been spent in order to derive a realistic linear model of an Hall-effect based tachometer. A specific algorithm to be implemented in the wheel electronics is then suggested in order to minimize the both the noise and delay introduced by the rate sensor. A PD controller is then chosen for the wheel speed loop because it allows to further increase the bandwidth of the inner loop, to improve the system stability and to provide safety margins with respect to additional delays. However, additional analysis shall be carried out in order to further investigate the stability of a cascade control system and a more detailed model of the sensor, especially of the noise source, shall be derived. The rate sensor's noise magnitude depends on the wheels speed, as a result it could be modeled by means of a waterfall spectrum description for a more detailed analysis.
- The wheel speed loop designed within the reference case demonstrates greater improvements in the pointing performance when compared to both the baseline controller, K_∞ , and the one with optimized integral action, $K_{\infty,\text{opt}}$. It can be observed that the pointing error contributions due to plateaus and spikes are reduced. In addition also the impact of the RW friction noise is greatly lowered. As expected, given the higher bandwidth of the speed loop the measurement noise and the solar pressure disturbances' impact on pointing performance remains almost unaltered.

Therefore, in contrast with the results achieved with the integral action optimization, disturbance transmission characteristics are enhanced without impairing the noise rejection. However, benefits achieved from this point of view is limited by the fact that an additional noise source has to be considered. Angular rate sensor noise takes on a large fraction of the noise contribution to the pointing error performances, also because a conservative model of this noise has been used hereby. In the following figures the overall pointing performance's improvements are illustrated with respect to plateaus torque profiles, Figure 5.30, and spikes torque profiles, Figure 5.31.

It can be concluded that, as far as the overall pointing error indices are concerned, disturbance transients now contribute only to a small extent, whereas the pointing performance of the control system is now driven by the measurements and tachometer noise levels.

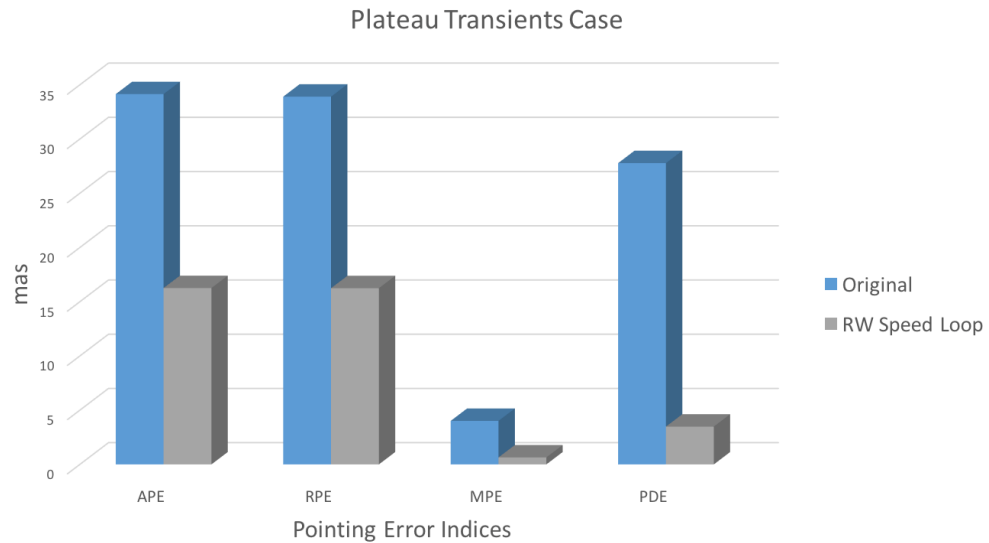


Figure 5.30: Overall pointing performance comparison between $K_{\infty,RW}$ and K_{∞} control strategies, with respect to a plateaus disturbance

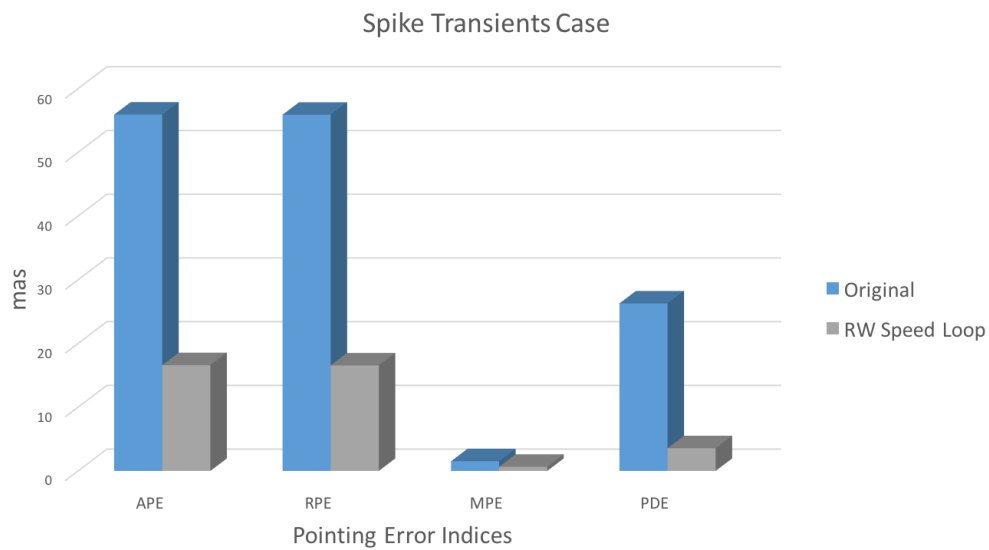


Figure 5.31: Overall pointing performance comparison between $K_{\infty,RW}$ and K_{∞} control strategies, with respect to a spikes disturbance

6

Conclusions

6.1. Summary

Disturbance transients that are generated by friction instabilities in the reaction wheels, have been proven to be a major concern for high precision pointing missions. Pointing-stability performance can be indeed greatly impaired by their occurrence. Along this thesis, these friction torque instabilities have been characterized according to the standard approach of pointing error engineering. Eventually the use of a wheel speed loop has been concluded to be a promising control strategy that can be practically implemented to improve control system performance with respect to wheels disturbance transients.

The thesis has been structured on two main research questions, general conclusions for each of them are presented here below.

Q.1 : How can the impact of wheels disturbance transients be characterized?

The pointing error engineering framework [11] provides the standards to perform pointing error transfer analysis and evaluations that are necessary in the controller synthesis phase. However, non-stationary transient error sources, as plateaus and spikes torque profiles are, were lacking of the proper analytical tool to allow them be included in a detail pointing error analysis. Therefore a pseudo-PSD formalism has been developed to describe these disturbances in the frequency domain. When applied to plateaus and spikes profiles it demonstrates that in both case the power of this signal is concentrated in the low-frequency range. Their impact on the different windowed pointing error indices can be then calculated analytically without the need of time-consuming numerical simulations, and additionally it can be expressed in a parametric form. As a result, within the scope of the thesis, the optimization of the control solutions investigated, with respect to wheels disturbance transients, can be done analytically providing better insights on the ACS limits and potential performance margins to be exploited.

Q.2 : Which control strategies can be used in order to handle wheels disturbance transients?

The 2PCD tool is a powerful mean to obtain a controller optimized with respect to stationary random noise disturbances. However when plateaus and spikes disturbances are considered pointing requirements might be violated, thus the need for a further controller optimization so that disturbance transients are handled as well. Using this control solution as a baseline two mitigation strategies have been investigated.

Given the fact that low-frequency non-stationary disturbances are addressed, better pointing performances are achieved providing the controller with a wider integral bandwidth. However, while disturbance rejection is improved, noise transmission is impaired. Along with this trade-off, a larger integral bandwidth has also a negative impact on the stability of the system. As a result, compared to the reference controller, pointing performance is improved despite the noise versus disturbance trade-off, however stability is jeopardized.

Alternatively, the friction torque instabilities can be suppressed by means of introducing an additional inner control loop at the actuator level, thus the implementation of a wheel speed loop is investigated. A fast inner loop allows to cut off the low frequency disturbances occurring in the wheels, while keeping the outer loop noise and disturbance rejection performances unaltered. On the other hand, the angular rate sensor, required to measure the speed of the wheel, is an additional source of noise that spoils the pointing performance. Results

show that pointing performance is enhanced even more and stability margins are better preserved, compared to the first solution.

As it can be observed in Figure 6.1, all relevant pointing error indices are greatly improved, specifically, given the fact that the plateaus disturbance's energy is concentrated at very low frequencies (less than 0.001 Hz according to Figure 3.4), MPE and PDE are the indices better optimized, whereas the noise still remains the major contributor for APE and RPE. Also when the spiky instabilities are considered, according to Figure 6.1, all relevant pointing error indices are improved. In this case, since the spikes profile's energy is spread to higher frequencies as well (up to 0.1 Hz according to Figure 3.4) APE and RPE are reduced to a greater relative extend, if compared to the plateaus case.

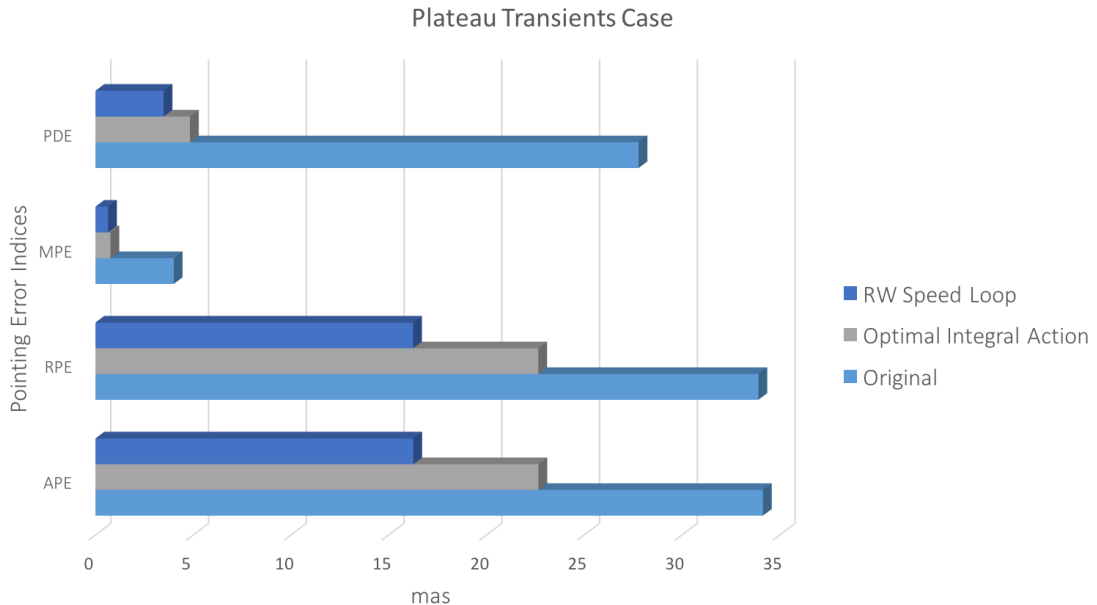


Figure 6.1: Overall pointing performances about the x axis with plateau profile disturbance transients occurring

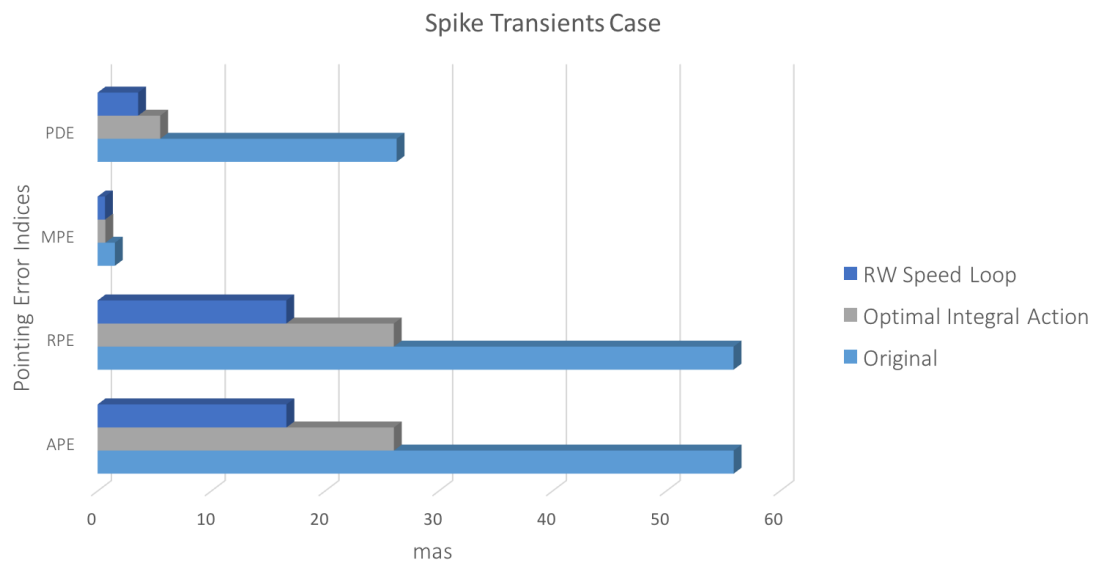


Figure 6.2: Overall pointing performances about the x axis with spike profile disturbance transients occurring

In conclusion, the implementation of a wheel speed loop turns to be an optimal solution to make the control system able to cope with disturbance transients originated in the reaction wheels. The impact of these disturbances to the pointing performance is indeed minimize to the extent that other pointing error sources are prevailing.

6.2. Outlook

The main contribution of this thesis, consisting in the demonstration of the benefits obtained through the implementation of a wheels speed control loop, comes along with some open points. Therefore further considerations should be made in order to drive the analysis that will follow this thesis. Similarly the second main contribution of the thesis, that regards the derivation of the analytical tools to describe disturbance transients, has several further applications it could be exploited for. As a result, the open points and guidelines for further future analysis are hereby briefly discussed.

- With respect to the precision pointing control design framework, that is schematically illustrated in Figure 1.3, it can be recalled that the main purpose the tool has been developed for is to perform a multi-objective controller design through a systematic single-step approach. Throughout the thesis, a secondary step has been introduced in the overall control design process to further optimize the ACS with respect to transient disturbances.

The mathematical tool developed in Chapter 3 allows to describe these transient torque profiles by means of a power spectral density formalism, in the same way the exogenous inputs considered within the H_∞ controller synthesis are characterized in the 2PCD tool. Therefore, the step forward shall be to include frequency domain description of friction torque instabilities in the H_∞ controller design framework, as disturbance inputs. The closed-loop specifications that determine the H_∞ control problem would then take into account also the error contribution generated by disturbance transients such as spikes and plateaus.

In such a way, the tool can be used to perform a control design optimized with respect to both random and deterministic PES's, as illustrated in Figure 6.3. There would be no need anymore to further optimize the controller in a secondary step as it has been done so far. The benefits from a pointing performance point of view are clear since the transfer characteristics of the ACS with respect to noise and disturbance transients are optimized simultaneously.

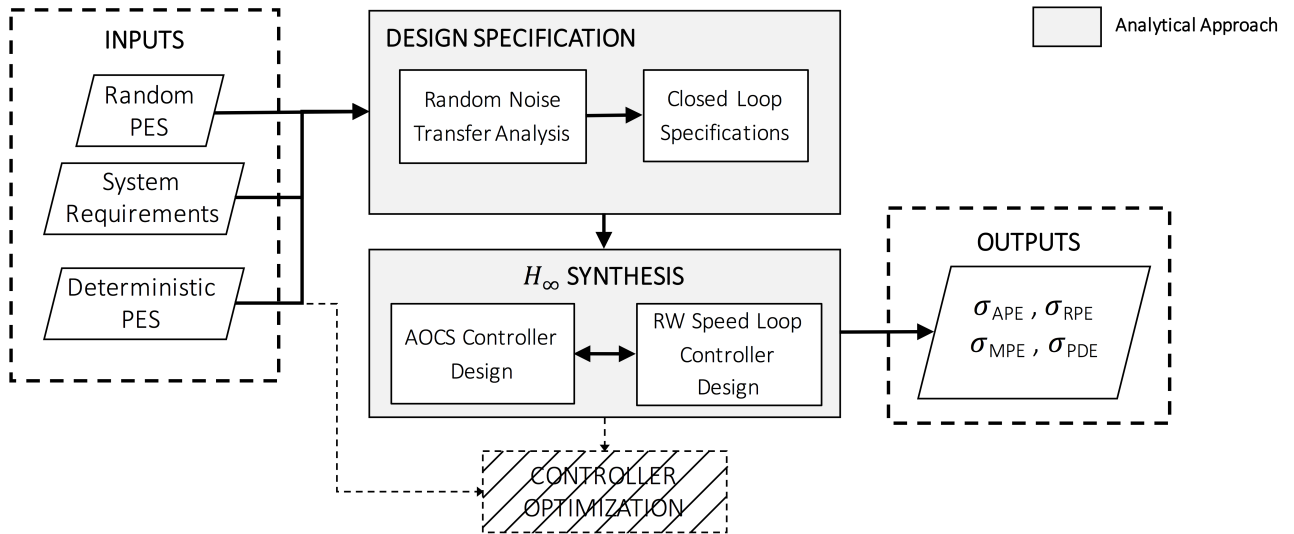


Figure 6.3: Outlook of the precision pointing control design framework extended to disturbance transients

Moreover, given the performance improvements resulting from the implementation of a wheel speed loop nested in the ACS control loop, the tuning of the inner loop controller shall be also included in the 2PCD tool's H_∞ synthesis. In other words, the in-house tool can be extended also to the synthesis of the wheel speed loop. The outer and inner loop controllers would be then designed simultaneously, hence reducing the amount of trade-offs and limits typically faced when the synthesis of a cascade controller is carried out in a sequential manner.

According to the approach used in [25], the problem formulation presented in Figure 2.4 can be further extended as illustrated in Figure 6.4. The generalized plant \tilde{P} should then include the angular rate sensor's transfer function, whereas a generalized controller \tilde{K} is additionally introduced. As a result, given

the pointing error requirements, random noise and deterministic transients exogenous inputs' characteristics, the H_∞ synthesis can be applied to design both the outer and inner controllers, respectively K_{ACS} and K_{RW} .

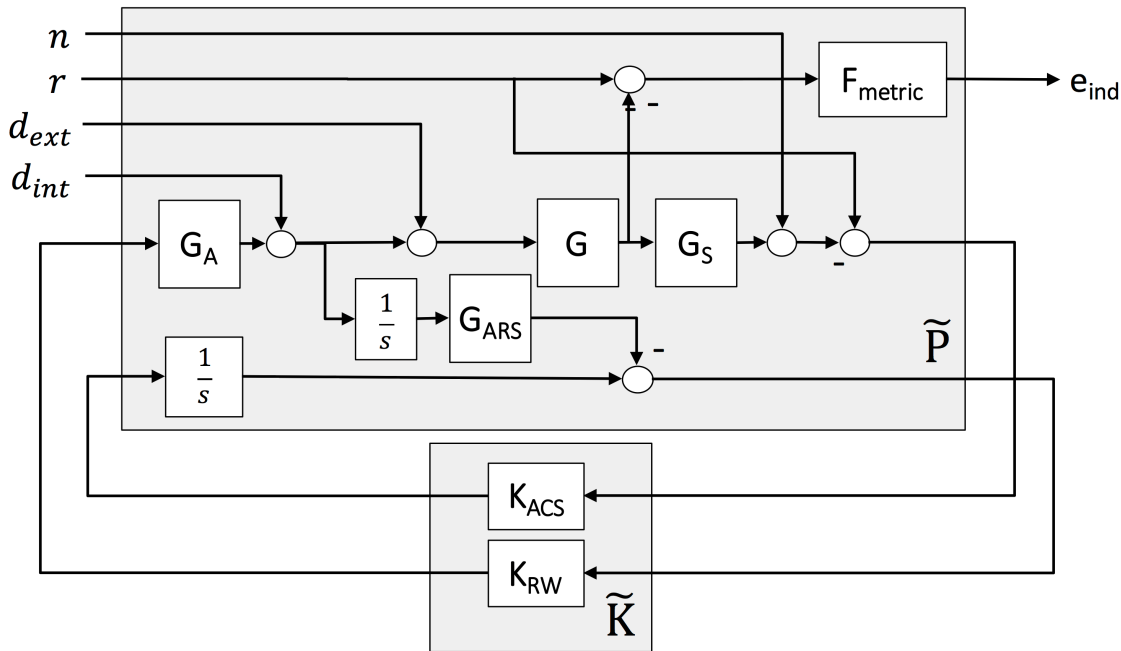
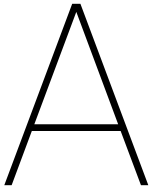


Figure 6.4: Outlook of the state-space control problem formulation including wheels speed loop

- As far as the implementation of a wheel speed loop is concerned, it has been showed that the ACS pointing performance greatly depends on the angular rate sensor characteristics. The sampling frequency, the delay and the noise due to jitter have been identified as the three sensor's parameters that considerably influence the overall performance of the attitude control system and a simplified linear model that takes them into account has been developed within this thesis. However, further investigations shall be carried out in cooperation with the wheels' manufacturer in order to gain a better understanding of the actual angular rate sensors practically installed in RWA's, so that a more detailed model can be then inferred. In particular, additional efforts shall be put in the characterization of the noise generated by Hall-effect based rate sensors. Given the fact that it depends on the speed of the wheel, more sophisticated mathematical tools, such as a waterfall plot, could be used to characterize it. Moreover, since the choices to be made within the design of the speed loop controller depend on the sensor parameters, e.g. the number of magnetic markers available around the wheels, the possibility of tailored solutions shall be considered in order to achieve high performances. For example, the implementation of the *variable pulses-counter scheduling* is an alternative strategy that can be suggested.

The linear model of the angular rate sensor developed within this thesis can be treated analytically and then included in the pointing error analysis performed during preliminary error budget evaluations or within the controller design process. Provided with specific pointing error requirements and the PEC's of the most relevant error sources of the system, the noise introduced by the ARS can be indeed included in the error budgets and, as done in Section 5.2, requirements can be gathered about the maximum ARS noise level admissible to achieve the system's specifications. Additionally, sensitivity analysis should be performed to derive requirements for the supplier also with respect to the minimum sampling frequency the sensor should be provided with.



Reference Case Study

A reference mission case study is required in order to practically apply the analytical considerations made in the course of the thesis and also to implement the control solutions addressed and then obtain numerical results that can be compared. With this respect, since the control optimization starting point is represented by the 2PCD tool, a reference case study mission is hereby exploited in line with the one used to validate the in-house tool. An attitude control subsystem equipped with four wheels in pyramid configuration is considered and the reference controller K_∞ is obtained through the 2PCD tool. The RWA's orientation and the relevant system characteristic parameters are here reported in Table A.1. The reference case study described in this section is referring to the ACS structure illustrated in Figure 2.5.

	Value	Units
Moment of Inertia	$\begin{bmatrix} 2100 & -5 & -120 \\ -5 & 2550 & 75 \\ -120 & 75 & 1200 \end{bmatrix}$	$[\text{Kgm}^2]$
RW Configuration Matrix	$\begin{bmatrix} 0 & 0 & \cos(65^\circ) & -\cos(65^\circ) \\ \sin(45^\circ) & \sin(45^\circ) & \sin(65^\circ) & \sin(65^\circ) \\ \cos(45^\circ) & -\cos(45^\circ) & 0 & 0 \end{bmatrix}$	\sim
Sensor Delay	0.1	[s]
Actuator Delay	0.15	[s]
Wheels Inertia	0.05	$[\text{Kgm}^2]$

Table A.1: Control system characteristic parameters within the reference case study

As far as the system's transfer functions are concerned, since all torque disturbances are then normalized with respect to the spacecraft moment of inertia, the system plant is then simply described by a double integrator.

$$G(s) = \frac{1}{s^2} \quad (\text{A.1})$$

In addition, also actuators and sensors dynamics are considered, respectively. Sensors and actuators both introduce errors in the system, due to e.g. digitalization of the signal, and delays in the channel, due to the sensor's electronics or the flywheel's inertia. Then, since noise and disturbance signals are already regarded as exogenous inputs, G_A and G_S are only meant to represent the delays introduced by actuators and sensors. For example, the reaction wheels transfer function, according to [25] and [36], can be then described as follows:

$$G_A(s) = e^{-s\Delta t_{RW}} = \frac{s^2 - \frac{6}{\Delta t_{RW}}s + \frac{12}{\Delta t_{RW}^2}}{s^2 + \frac{6}{\Delta t_{RW}}s + \frac{12}{\Delta t_{RW}^2}} \quad (\text{A.2})$$

The right hand-side of Equation A.2 is a second order Padé approximation of a pure delay transfer function, where Δt_{RW} is the time delay introduced by the wheel dynamics. This rational approximation is used since

the exponential often leads to numerical issues, especially when the transfer function has to be inverted. The sensor dynamics G_S can be then modeled in the same manner. Moreover, this approach is the same one used in the H_∞ design tool, hence it is applied also in this analysis for the sake of consistency.

The parameters used to evaluate the widowed pointing error indices are listed in Table A.2. The values used are inspired from a previous high-precision pointing science mission.

	Value	Units
Δt_{window}	700	s
Δt_{stab}	700	s
$\Delta t_{\text{window,stab}}$	50	s

Table A.2: Reference case study parameters of the windowed pointing error indices

According to the ACS diagram illustrated in Figure 2.5 the exogenous signals that are acting as error sources in the control system are the wheels disturbance transients, d_{FTI} , and the reference noise PES's. The reference pointing error sources are the same one considered in the 2PCD framework, measurement noise n_s , RW torque noise d_{RW} , and solar pressure torque noise d_{SP} . According to [25] these input noise sources are normalized such that their PSD attain the power of one. The power spectrum is then multiplied by a spectral shaping filters in order to augment information about disturbance and noise frequency content on the control system plant. The solar pressure weighting filters $W_d(s)$ are illustrated in the figures below.

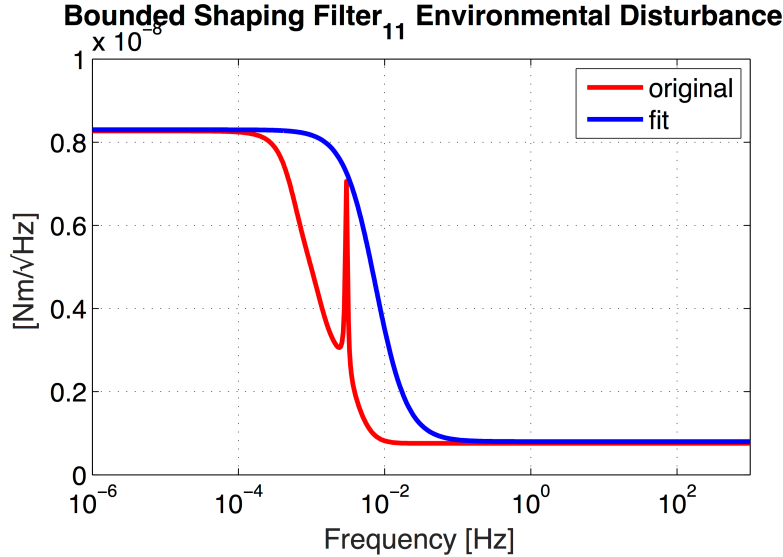


Figure A.1: Solar pressure disturbance's weighting filter with respect to the x axis

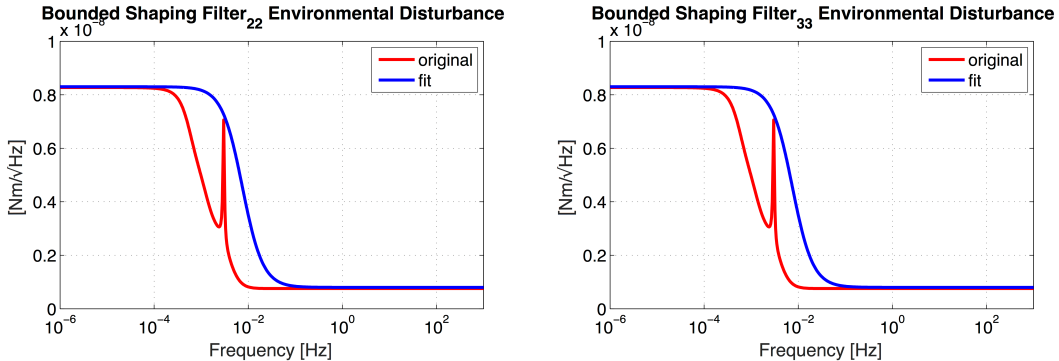


Figure A.2: Solar pressure disturbance's weighting filter with Figure A.3: Solar pressure disturbance's weighting filter with respect to the y axis
respect to the z axis

The weighting filters $W_n(s)$ of the measurements noise are instead derived from spectral data obtained from previous missions' data. The filters used in the reference case study are illustrated in the figures below.

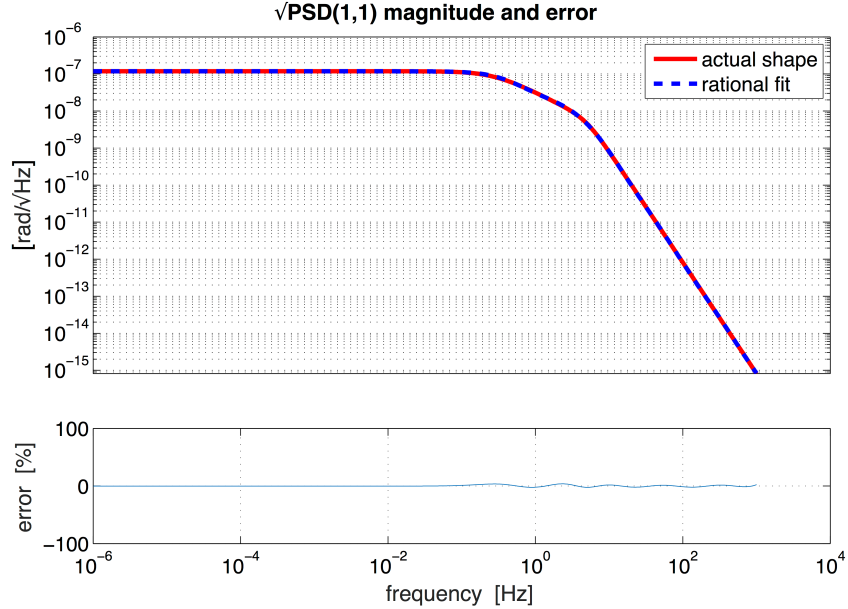


Figure A.4: Measurements noise's weighting filter with respect to the x axis

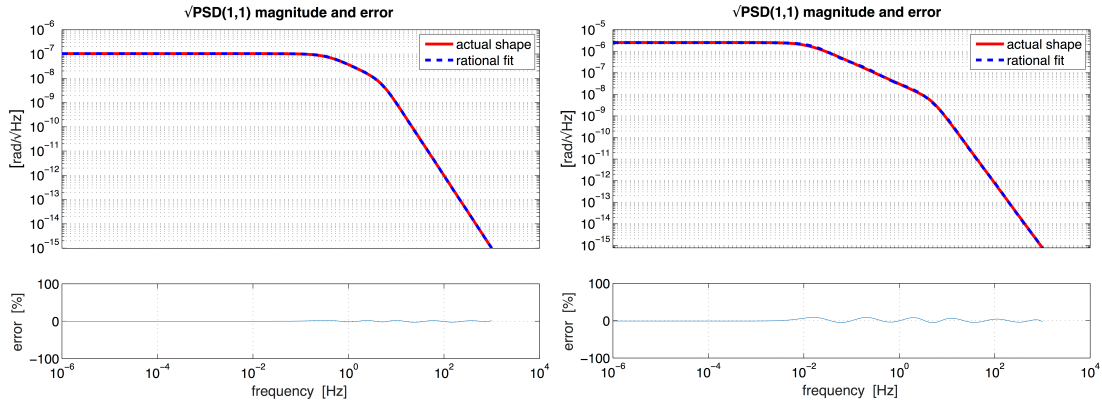


Figure A.5: Measurements noise's weighting filter with respect to the y axis

Figure A.6: Measurements noise's weighting filter with respect to the z axis

The parameters used to describe the plateaus and spikes disturbances are the transient duration, T_d , the instability period, T_p , and the torque level, τ_{\max} . The values used in the analysis are selected accordingly to the worst case scenario values used in [36]. In addition, according to the RW supplier heritage only one of the four reaction wheels is likely to show friction torque instabilities, therefore according to the choice made in [36] disturbance transients are considered only occurring on wheel 3.

	Plateaus	Spikes	Units
τ_{\max}	2.4	2.9	mNm
T_p	2000	200	s
T_d	300	20	s

Table A.3: Reference case study parameters of plateaus and spikes instability profiles

The friction noise generated by the reaction wheels is instead modeled as a band-limited white noise which attain a uniform power spectral density of $5.5 \text{ [Nm}^2/\text{Hz]}$ and that has a cut-off frequency determined by the

actuation sampling time $f_{\text{cut-off}} = 1$ [Hz].

The requirements about stability margins used within the H_∞ synthesis are the standard values also mentioned in [32]. Since they are later employed in the control design of the different solutions investigated in the following chapters, the values used are listed in Table A.4.

	Value	Units
GM	5	dB
PM	30	deg
M_S	6	dB
M_T	6	dB

Table A.4: Stability margins requirements used within the H_∞ synthesis

B

Mathematical Derivations

B.1. Pseudo-Power Spectral Density Derivations

Let assume $x_0(t)$ to be a time function defined over a single period T_p and $x(t)$ the periodic function obtained by repeating $x_0(t)$ indefinitely with the same time period T_p , the following relation holds in the time domain:

$$x(t) = \sum_{k=-\infty}^{+\infty} x_0(t - kT_p) \quad (\text{B.1})$$

The signal power can be then calculated as:

$$P_x = \lim_{T \rightarrow \infty} \frac{1}{T} \int_0^T |x(t)|^2 dt = \lim_{T \rightarrow \infty} \frac{1}{T} \int_0^T \left| \sum_{k=0}^N x_0(t - kT_p) \right|^2 dt \quad (\text{B.2})$$

In addition, since $x(t)$ consists of a sum of single period functions $x_0(t - kT_p)$ that are not overlapping and that are equal to zero everywhere except for $[kT_p < t < (k+1)T_p]$, the following equality is true.

$$\left| \sum_{k=0}^N x_0(t - kT_p) \right|^2 = \sum_{k=0}^N |x_0(t - kT_p)|^2 = (N+1) |x_0(t)|^2 \quad (\text{B.3})$$

Assuming that the time span considered in the limit contains a finite number of waveform periods, $T = (N + 1)T_p$, it then follows:

$$\begin{aligned} P_x &= \lim_{T \rightarrow \infty} \frac{1}{T} \sum_{k=0}^N \int_0^T |x_0(t - kT_p)|^2 dt = \lim_{T \rightarrow \infty} \frac{1}{T} \sum_{k=0}^N \int_{kT_p}^{(k+1)T_p} |x_0(t - kT_p)|^2 dt \\ &= \lim_{T \rightarrow \infty} \frac{1}{T} (N+1) \int_0^{T_p} |x_0(t)|^2 dt = \lim_{N \rightarrow \infty} \frac{(N+1)}{T_p(N+1)} \int_0^{T_p} |x_0(t)|^2 dt \\ &= \lim_{N \rightarrow \infty} \frac{1}{T_p} \int_0^{T_p} |x_0(t)|^2 dt = \frac{1}{T_p} \int_0^{T_p} |x_0(t)|^2 dt \end{aligned} \quad (\text{B.4})$$

Then applying the Parseval's theorem as defined in Equation 2.20 the expression of a pseudo-power spectral density is obtained.

$$\begin{aligned} P_x &= \frac{1}{T_p} \int_{-\infty}^{\infty} |x_0(t)|^2 dt = \frac{1}{T_p} \int_{-\infty}^{\infty} |X(f)|^2 df \\ &= \int_{-\infty}^{\infty} \frac{|X(f)|^2}{T_p} df \end{aligned} \quad (\text{B.5})$$

B.2. Plateaus ans Spikes Profiles Characterization

Plateau Profile As far as the rectangular function is concerned, it can be approximated in the time domain by a Fourier series. Given the analytical expression of $b(t)$ in Equation 3.1 and assuming the initial time $t_0 = 0$,

the Fourier coefficients are then computed analytically as follows:

$$\begin{aligned}
 z_b(k) &= \frac{1}{T_p} \int_{-T_d/2}^{T_d/2} \tau_{\max} e^{-jk\omega_0 t} dt = \frac{\tau_{\max}}{T_p} \left[-\frac{e^{-jk\omega_0 t}}{jk\omega_0} \right]_{-T_d/2}^{T_d/2} \\
 &= \frac{2\tau_{\max}}{k\omega_0 T_p} \left[\frac{e^{+jk\omega_0 T_d/2} - e^{-jk\omega_0 T_d/2}}{2j} \right] \\
 &= \tau_{\max} \frac{T_d}{T_p} \frac{\sin(k\omega_0 T_d/2)}{k\omega_0 T_d/2} \\
 &= \tau_{\max} \frac{T_d}{T_p} \text{sinc}(k\omega_0 T_d/2)
 \end{aligned} \tag{B.6}$$

Then, let $\epsilon = T_d/T_p$ be the duty cycle parameter and recall that the fundamental harmonic is $\omega_0 = 2\pi/T_p$.

$$z_b(k) = \tau_{\max} \epsilon \text{sinc}(k\pi\epsilon) e^{-jk\pi\epsilon} \tag{B.7}$$

Thus, the square waveform can be approximated by the following expression.

$$b(t) = \tau_{\max} \epsilon + \sum_{k=1}^{\infty} [2\tau_{\max} \epsilon \text{sinc}(k\pi\epsilon)] \tag{B.8}$$

In the frequency domain, $b(t)$ can be represented by a discrete amplitude spectrum which is described by Equation B.9.

$$B_{\text{disc}}(f_k) = \tau_{\max} \epsilon \text{sinc}(k\pi\epsilon) \tag{B.9}$$

And a discrete power spectrum:

$$|B_{\text{disc}}(f_k)|^2 = (\tau_{\max} \epsilon)^2 \text{sinc}(k\pi\epsilon)^2 \tag{B.10}$$

As far as $b_0(t)$ is concerned the Fourier Transform can be calculated:

$$B(f) = \tau_{\max} T_d \text{sinc}\left(2\pi f \frac{T_d}{2}\right) \tag{B.11}$$

Hence the pseudo-PSD can be derived applying the definition provided in Equation 3.7:

$$\tilde{S}_{bb}(f) = \frac{(\tau_{\max} T_d)^2}{T_p} \text{sinc}\left(2\pi f \frac{T_d}{2}\right)^2 \tag{B.12}$$

Spike Profile As far as the triangular function is concerned, it can be approximated in the time domain by a Fourier series. Given the analytical expression of $p(t)$ in Equation 3.3 and assuming the initial time $t_0 = 0$, the Fourier coefficients are then computed analytically as follows:

$$\begin{aligned}
 z_p(k) &= \frac{\tau_{\max}}{T_p} \left[\int_{-T_d/2}^0 \left(1 + \frac{2t}{T_d}\right) e^{-jk\omega_0 t} dt + \int_0^{T_d/2} \left(1 - \frac{2t}{T_d}\right) e^{-jk\omega_0 t} dt \right] \\
 &= \frac{\tau_{\max}}{T_p k \omega_0} \left[\left(j + \frac{1}{k\omega_0 T_d/2} - \frac{e^{jk\omega_0 T_d/2}}{k\omega_0 T_d/2}\right) + \left(-j + \frac{1}{k\omega_0 T_d/2} - \frac{e^{-jk\omega_0 T_d/2}}{k\omega_0 T_d/2}\right) \right] \\
 &= \frac{2\tau_{\max}}{T_p T_d} \frac{2 - (e^{jk\omega_0 T_d/2} + e^{-jk\omega_0 T_d/2})}{(k\omega_0)^2} = \frac{2\tau_{\max}}{T_p T_d} \frac{2 - 2 \cos(k\omega_0 T_d/2)}{(k\omega_0)^2} \\
 &= \frac{4\tau_{\max}}{T_p T_d} \frac{1 - \cos(k\omega_0 T_d/2)}{(k\omega_0)^2} = \frac{4\tau_{\max}}{T_p T_d} \frac{2 \sin(k\omega_0 T_d/4)^2}{(k\omega_0)^2} \\
 &= \frac{8\tau_{\max}}{T_p T_d} \frac{\sin(k\omega_0 T_d/4)^2}{(k\omega_0)^2} \frac{2T_d}{2T_d} = \frac{\tau_{\max} T_d}{2T_p} \frac{\sin(k\omega_0 T_d/4)^2}{(k\omega_0 T_d/4)^2} \\
 &= \frac{\tau_{\max} T_d}{2T_p} \text{sinc}(k\omega_0 T_d/4)^2
 \end{aligned} \tag{B.13}$$

Then, let $\epsilon = T_d/T_p$ be the duty cycle parameter and recall that the fundamental harmonic is $\omega_0 = 2\pi/T_p$.

$$z_p(k) = \tau_{\max} \frac{\epsilon}{2} \text{sinc}\left(k\pi \frac{\epsilon}{2}\right)^2 \tag{B.14}$$

Thus, the triangular waveform can be approximated by the following expression:

$$p(t) = \tau_{\max} \frac{\epsilon}{2} + \sum_{k=1}^{\infty} \left[\tau_{\max} \epsilon \text{sinc} \left(k\pi \frac{\epsilon}{2} \right)^2 \right] \quad (\text{B.15})$$

In the frequency domain, $p(t)$ can be represented by a discrete amplitude spectrum which is described by Equation B.16.

$$P_{\text{disc}}(f_k) = \tau_{\max} \frac{\epsilon}{2} \text{sinc} \left(k\pi \frac{\epsilon}{2} \right)^2 \quad (\text{B.16})$$

And a discrete power spectrum:

$$|P_{\text{disc}}(f_k)|^2 = \frac{(\tau_{\max} \epsilon)^2}{2} \text{sinc} \left(k\pi \frac{\epsilon}{2} \right)^4 \quad (\text{B.17})$$

As far as $p_0(t)$ is concerned the Fourier Transform can be calculated:

$$P(f) = \tau_{\max} \frac{T_d}{2} \text{sinc} \left(2\pi f \frac{T_d}{4} \right) \quad (\text{B.18})$$

Hence the pseudo-PSD can be derived applying the definition provided in Equation 3.7:

$$\tilde{S}_{\text{pp}}(f) = \frac{(\tau_{\max} T_d)^2}{4 T_p} \text{sinc} \left(2\pi f \frac{T_d}{4} \right)^4 \quad (\text{B.19})$$

C

Mitigation Methods

C.1. PID Controller Case Study

Referring to the diagram illustrated Figure 2.5, the transfer function $H_d(s)$ is the one that relates the output pointing error e to the input disturbance d and it is defined as follows:

$$H_d(s) = \frac{e}{d} = -\frac{G}{1 + KG_A GG_S} \quad (\text{C.1})$$

When a PD or PID controller, assuming no delays, i.e. $G_A = 1$ and $G_S = 1$, it can be calculated as follows:

$$H_{d,\text{PD}}(s) = \frac{1}{s^2 + k_D s + k_P} \quad (\text{C.2})$$

$$H_{d,\text{PID}}(s) = \frac{s}{s^3 + k_0 k_{PD} k_{PI} s^2 + k_0 (k_{PD} + k_{PI}) s + k_0} \quad (\text{C.3})$$

Preliminary calculations were used in order to evaluate and analyze the impact of the integral action on the system's stability and performances. The controller parameters used are listed in the table below.

	k_0	k_{PD}	k_{PI}
Value	2.75	0.75	0.5

Table C.1: PID controller parameters used for preliminary investigation on the integral action

C.2. Further Results for the Integral Action Optimization

y Axis An optimal value of $k_{\text{PI}} = 0.65$ is the result of the integral action tuning. Here after pointing performances and stability margins achieved are reported.

		σ_{APE} [mas]	σ_{MPE} [mas]	σ_{RPE} [mas]	σ_{PDE} [mas]
K_{∞}	Plateaus	21.253	2.581	21.095	18.796
	Spikes	47.471	1.017	47.460	19.954
	Noise	27.937	0.613	27.301	5.534
	Plateaus + Noise	35.102	2.653	35.001	19.954
	Spikes + Noise	55.082	1.187	55.069	20.707
$K_{\infty,\text{opt}}$	Plateaus	5.995	0.379	5.9835	2.988
	Spikes	14.070	0.199	14.068	3.950
	Noise	27.283	0.569	27.277	3.208
	Plateaus + Noise	27.934	0.684	27.926	4.384
	Spikes + Noise	30.697	0.603	30.692	5.089

Table C.2: Pointing error budget with respect to the y axis

	GM [dB]	PM [deg]	M_S [dB]	M_T [dB]
K_{∞}	9.36	50.80	3.76	2.38
$K_{\infty,\text{opt}}$	9.02	32.22	5.31	5.99

Table C.3: Comparison of the stability margins obtained with the $K_{\infty,\text{opt}}$ and K_{∞} control strategies (y axis)

z Axis An optimal value of $k_{\text{PI}} = 0.55$ is the result of the integral action tuning. Here after pointing performances and stability margins achieved are reported.

		σ_{APE} [mas]	σ_{MPE} [mas]	σ_{RPE} [mas]	σ_{PDE} [mas]
K_{∞}	Plateaus	0.187	0.026	0.186	0.181
	Spikes	0.386	0.009	0.385	0.181
	Noise	84.753	13.658	83.646	65.550
	Plateaus + Noise	84.754	13.658	83.646	65.550
	Spikes + Noise	84.754	13.658	83.647	65.550
$K_{\infty,\text{opt}}$	Plateaus	0.0487	0.0035	0.0486	0.0279
	Spikes	0.1204	0.0018	0.1203	0.0358
	Noise	82.5126	13.648	81.3760	64.758
	Plateaus + Noise	82.5126	13.648	81.3760	64.758
	Spikes + Noise	82.5127	13.648	81.3761	64.758

Table C.4: Pointing error budget with respect to the z axis

	GM [dB]	PM [deg]	M_S [dB]	M_T [dB]
K_{∞}	9.74	54.69	3.57	1.95
$K_{\infty,\text{opt}}$	9.44	37.21	4.41	4.90

Table C.5: Comparison of the stability margins obtained with the $K_{\infty,\text{opt}}$ and K_{∞} control strategies (z axis)

C.3. Angular Rate Sensor Model

Fixed Delay Mode In the first case scenario illustrated in Figure 5.7, the estimation of the wheels rate can be considered sufficiently valid, given the fact that the angular displacement measured by the sensor $\Delta\alpha_{ARS}$ is close to the actual angular displacement experienced by the wheel $\Delta\alpha_{real}$. Hence

$$\omega_{ARS} = \frac{\Delta\alpha_{ARS}}{T_S} \approx \frac{\Delta\alpha_{real}}{T_S} = \omega \quad (C.4)$$

However, in the second case, the wheel speed is greatly overestimated. Indeed it can be noticed that the angular displacement measured by the sensor is $3\Delta\alpha$ while the actual one is closer to $2\Delta\alpha$.

$$\omega_{ARS} = \frac{N_{ARS}\Delta\alpha}{T_S} = 3 \frac{\Delta\alpha}{T_S} \neq \omega \quad (C.5)$$

This computational method suffers indeed of a resolution error. Given that $\Delta\alpha = 2\pi/n_{ARS}$, the discrete values that the output angular rate can assume are:

$$\omega_{ARS} = i \frac{\Delta\alpha}{T_S} = i \frac{2\pi}{n_{ARS} T_S}, \quad i = 1, 2, \dots \quad (C.6)$$

Hence, given an ARS time window, the maximum deviation of the ARS output from the actual mean spin rate is equal to one resolution step:

$$\Delta\omega = \frac{\Delta\alpha}{T_S} = \frac{2\pi}{n_{ARS} T_S} \quad (C.7)$$

For this reason, furthermore, the ARS cannot handle constant spin rates. The ARS output of the RW Simulink block (red line) jumps periodically between the two closest quantization levels when the actual wheel's speed (blue line) is constant, as illustrated in Figure C.1.

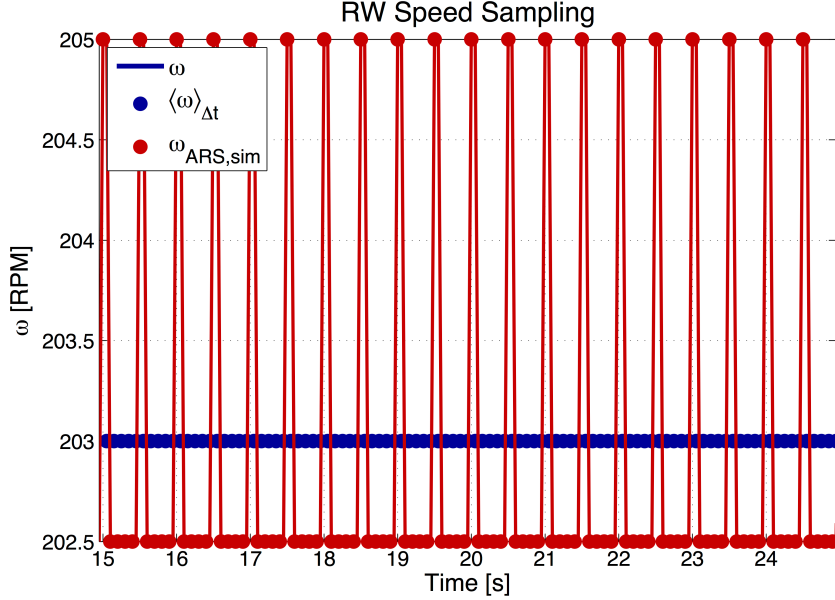


Figure C.1: Constant wheel speed scenario with *fixed delay mode* implemented in the angular rate sensor

Variable Delay Mode It can happen that the time between two pulses is shorter than the simulation time step, as illustrated in Figure C.2. Hence, due to the time discretization of the simulations, the actual value of Δt_{eff} between the two pulses at issue has to be computed.

Given the nomenclature in Figure C.2, in order to handle this, the ARS model derives $\Delta\alpha_{rem}$ from the wheel's dynamic integration and it then estimates Δt_{rem} as follows:

$$\Delta t_{rem} = \frac{\Delta\alpha_{rem}}{\omega(t_2)} \quad (C.8)$$

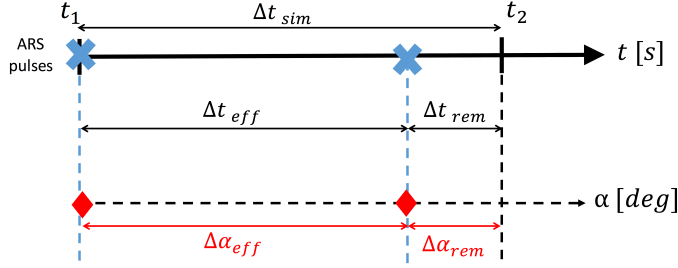


Figure C.2: Graphical illustration of the numerical issue introduced by time domain discretized simulations

Thus, it follows that the effective time passed between the two pulses is $\Delta t_{eff} = \Delta t_{sim} - \Delta t_{rem}$ and then the angular rate estimate of the ARS can be computed with Equation 5.7. However, if ω is not constant and it is instead rising or dropping within the simulation step considered, the value of Δt_{rem} is respectively under- or overestimated. In turns, according to Equation 5.7 the ARS simulator output would give a under- or overestimate of the actual measure that the sensor would give in reality.

This can be verified comparing the time histories of the expected ARS output and both Δt_{rem} and $\Delta\alpha_{rem}$, when a wheel with constantly rising speed is considered. The ARS model output is indeed always underestimated (negative error) and the numerical issue disappears only as soon as the Δt_{rem} drops to zero, i.e. when $\Delta t_{ARS} = \Delta t_{sim}$.

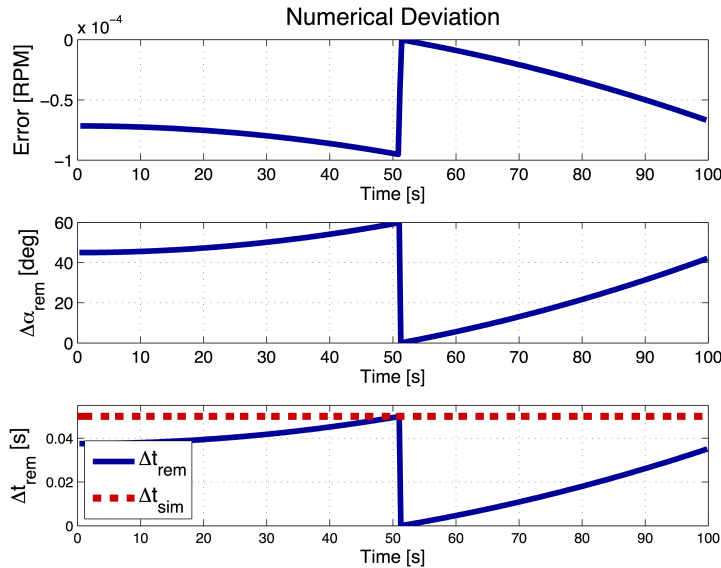


Figure C.3: Numerical deviations in ARS Simulink model output due to the time discretization

C.4. Wheel Speed Loop Controller Design

As far as the design of the speed loop controller is concerned, a solely proportional controller can improve the performances (Figure C.5), however the stability margins are impaired for large values of the proportional coefficient. As it can be observed in Figure C.4 the sensitivity function's peak value is constantly above the maximum required value.

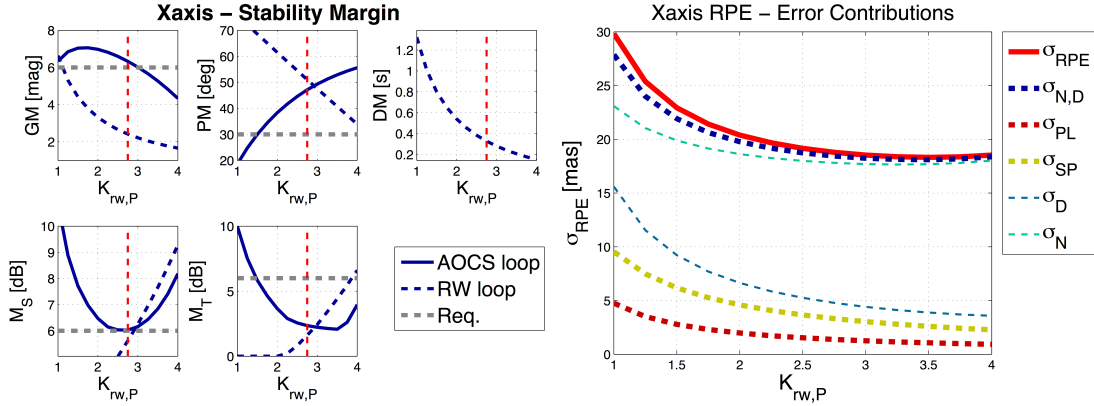


Figure C.4: Stability margins for different values of the inner loop controller's proportional gain (x axis)

Figure C.5: RPE budget for different values of the inner loop controller's proportional gain (x axis)

Despite all the preliminary considerations presented in Section 5.3 that brought to the selection of a PD controller, also a PI controller-based solution has been investigated. However, as depicted in Figure C.6, it can be noticed that the performance is greatly impaired for any value of the integral coefficient. This is because the noise introduced by the ARS gets amplified by the integral action of the wheel speed loop. A PI controller was implemented in the RW current loop by [3], however in that case its use can be explained by the fact that in a current loop noise is not present or it is somehow negligible, therefore the noise rejection is not a major concern.

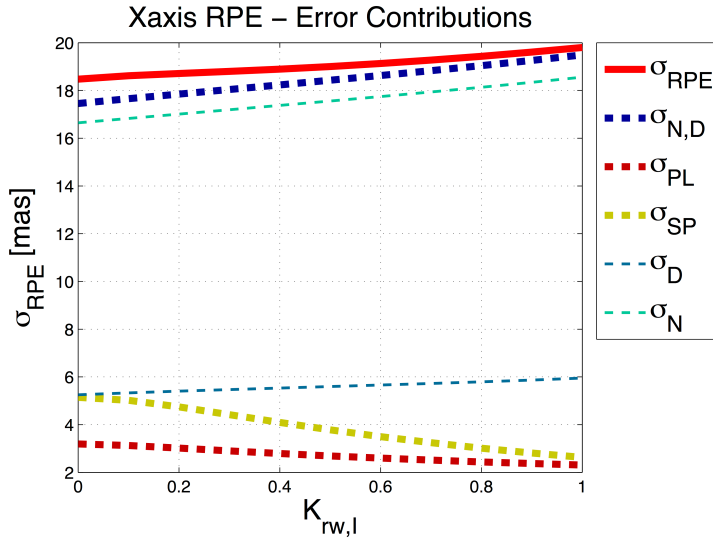


Figure C.6: RPE budget for different values of the inner loop controller's integral gain (x axis)

C.5. Further Results for the Wheel Speed Loop Implementation

y Axis An optimal value of $k_p = 2.5$ and $k_p = 0.45$ is the result of the tuning. Here after pointing performances and stability margins achieved about the y axis are reported.

		σ_{APE} [mas]	σ_{MPE} [mas]	σ_{RPE} [mas]	σ_{PDE} [mas]
K_∞	Plateaus	21.253	2.581	21.095	18.796
	Spikes	47.471	1.017	47.460	19.954
	Ref. Noise + Dist.	27.937	0.613	27.301	5.534
	Plateaus + Noise	35.102	2.653	35.001	19.954
$K_{\infty,RW}$	Spikes + Noise	55.082	1.187	55.069	20.707
	Plateaus	1.778	0.0172	1.778	0.339
	Spikes	3.735	0.0384	3.735	0.766
	Ref. Noise + Dist.	21.358	0.5668	21.350	3.045
	Plateaus + Noise	21.432	0.567	21.424	3.064
	Spikes + Noise	21.682	0.568	21.674	3.140

Table C.6: Pointing error budget with respect to the y axis

	GM [dB]	PM [deg]	M_S [dB]	M_T [dB]
K_∞	9.36	50.80	3.76	2.38
$K_{\infty,RW}$	11.35	41.23	4.32	3.40

Table C.7: Comparison of the stability margins obtained with the $K_{\infty,RW}$ and K_∞ control strategies (y axis)

z Axis An optimal value of $k_p = 2$ and $k_p = 0.45$ is the result of the tuning. Here after pointing performances and stability margins achieved about the z axis are reported.

		σ_{APE} [mas]	σ_{MPE} [mas]	σ_{RPE} [mas]	σ_{PDE} [mas]
K_∞	Plateaus	0.187	0.026	0.186	0.181
	Spikes	0.386	0.009	0.385	0.181
	Ref. Noise + Dist.	84.753	13.658	83.646	65.550
	Plateaus + Noise	84.754	13.658	83.646	65.550
$K_{\infty,RW}$	Spikes + Noise	84.754	13.658	83.647	65.550
	Plateaus	0.015	0.0001	0.015	0.0037
	Spikes	0.035	0.0004	0.035	0.0078
	Ref. Noise + Dist.	79.857	13.649	78.681	64.856
	Plateaus + Noise	79.857	13.649	78.681	64.856
	Spikes + Noise	79.857	13.649	78.681	64.856

Table C.8: Pointing error budget with respect to the z axis

	GM [dB]	PM [deg]	M_S [dB]	M_T [dB]
K_∞	9.74	54.69	3.57	1.95
$K_{\infty,RW}$	13.29	41.60	4.20	3.29

Table C.9: Comparison of the stability margins obtained with the $K_{\infty,RW}$ and K_∞ control strategies (z axis)

Bibliography

- [1] Bendat, J. S. and Piersol, A. G. *Random Data: Analysis and Measurement Procedures*. 4th edition, 2014.
- [2] W.E. Bialke. Reconfigurable Reaction Wheel For Spacecraft, 2008. URL <http://www.google.com/patents/US20080099626>. US Patent App. 11/588,801.
- [3] V. Carrara and H. K. Kuga. Torque and Speed Control Loops Of A Reaction Wheel. *11th International Conference on Vibration Problems*, (September), 2013.
- [4] V. Carrara et al. Speed and Current Control Mode Strategy Comparison in Satellite Attitude Control With Reaction Wheels. *ABCM Symposium Series in Mechatronics*, 5, 2011.
- [5] M Casasco, G Saavedra Criado, S Weikert, J Eggert, M Hirth, T Ott, and H Su. Pointing error budgeting for high pointing accuracy mission using the pointing error engineering tool. *AIAA Guidance, Navigation, and Control (GNC) Conference*, 2013.
- [6] M. Casasco et al. Pointing Error Engineering Framework for High Pointing Accuracy Missions. *24th International Symposium on Space Flight Dynamics (ISSFD)*, Laurel, Maryland, USA, 2014.
- [7] L. Chuanjiang et al. A constrained optimal PID-like controller design for spacecraft attitude stabilization. *Acta Astronautica*, 74, 2012.
- [8] Anton H. J. De Ruiter et al. *Spacecraft Dynamics and Control: An Introduction*. 1st edition, 2013.
- [9] J. C. Gamazo-Real et al. Position and Speed Control of Brushless DC Motors Using Sensorless Techniques and Application Trends. *Sensors (Basel, Switzerland)*, 10, 2010.
- [10] ECSS Working Group. Control Performance Standard. *European Cooperation for Space Standardization*, (December), 2010.
- [11] ECSS Working Group. ESA Pointing Error Engineering Handbook. *European Space Agency*, (July), 2011.
- [12] Sidi M. J. *Spacecraft Dynamics and Control: A Practical Engineering Approach*. 1st edition, 1997.
- [13] J. Jyh-Ching et al. Spacecraft robust attitude tracking design: PID control approach. *Proceedings of the 2002 American Control Conference*, 2, 2002.
- [14] R. Kelly. Global positioning of robot manipulators via PD control plus a class of nonlinear integral actions. *IEEE Transactions on Automatic Control*, 43, 1998.
- [15] T. Kia, D. S. Bayard, and F. Tolivar. A precision pointing control system for the space infrared telescope facility (SIRTF). *Advances in the Astronautical Sciences*, 1997.
- [16] M. G. F. Kirsch et al. Cage instability of XMM-Newton's reaction wheels discovered during the development of an Early Degradation Warning System. *12th International Conference on Space Operations, SpaceOps*, 2012.
- [17] M. G. F. Kirsch et al. Bearing Noise Detection, Modelling and Mitigation Measures on ESA's X-Ray Observatory XMM-NEWTON. *Advances in the Astronautical Sciences Guidance, Navigation and Control*, 15, 2014.
- [18] D. Lasnet. Improvement Solutions - AOCS and System Level. *Airbus Defence and Space*, 2014.
- [19] A. Y. Lee and G. Hanover. Cassini Spacecraft Attitude Control System Flight Performance. *AIAA Guidance, Navigation, and Control Conference and Exhibit*, 2005.
- [20] A. Y. Lee and E. K. Wang. In-Flight Performance of Cassini Reaction Wheel Bearing Drag in 1997–2013. *Journal of Spacecraft and Rockets*, 2015.

- [21] P. McMahon and R. Lavén. Results From 10 Years of Reaction/Momentum Wheel Life Testing. *11th European Space Mechanisms and Tribology Symposium, Lucerne, Switzerland*, 2005.
- [22] L. Meza et al. Line of Sight Stabilization for the James Webb Space Telescope. *27th AAS Guidance and Control Conference, Colorado*, 2005.
- [23] NASA. Space Mechanisms Lessons Learned Study. Dec 2007. URL <http://www.grc.nasa.gov/WWW/spacemech/vol1.html>.
- [24] T. Ott, S. Winkler, F. Cirillo, and W. Fichter. Robust Precision Pointing Control Design for Spacecraft with Disturbance Transients. *Presentation at ESA GNC 2014, 02.-06. June, Porto, Portugal*.
- [25] T. Ott, W. Fichter, S. Bennani, and S. Winkler. Precision Pointing H_∞ Control Design for Absolute, Window-, and Stability-time Errors. *8th International ESA Conference on Guidance, Navigation and Control Systems, Karlovy Vary, CZ*, 2011.
- [26] M. Pantaleoni et al. Curing XMM-Newton's reaction wheel cage instability: the in-flight re-lubrication experience. *13th International Conference on Space Operations, SpaceOps*, 2014.
- [27] E. B. Pilinski et al. Pointing-Stability Performance of the Cassini Spacecraft. *Journal of Spacecraft and Rockets*, 46, 2009.
- [28] B. Robertson and E. Stoneking. Satellite GN&C anomaly trends. *Advances in the Astronautical Sciences*, 113, 2003.
- [29] M. Schmidt and D. Salt. Herschel pointing accuracy improvement. *12th International Conference on Space Operations, SpaceOps*, 2012.
- [30] F. Schmidt et al. XMM-newtons operations preparation for the 4 wheel drive project. *13th International Conference on Space Operations, SpaceOps*, 2014.
- [31] G. Shengmin and C. Hao. A comparative design of satellite attitude control system with reaction wheel. *First NASA/ESA Conference on Adaptive Hardware and Systems*, 2006.
- [32] S. Skogestad and I. Postlethwaite. *Multivariable Feedback Control: Analysis and Design*. 2nd edition, 2005.
- [33] P. Tsotras. Stabilization and optimality results for the attitude control problem. *Journal of Guidance, Control, and Dynamics*, 19, 1996.
- [34] M. Vitelli et al. Comprehensive Investigation of Micro-Vibrations Impact Due To Different Disturbance Sources on Spacecraft Pointing Stability For The Bebi Colombo Mission. *9th International ESA Conference on Guidance, Navigation & Control System*, 2014.
- [35] B. Wie. *Space Vehicle Dynamics and Control*. 2nd edition, 2008.
- [36] S. Winckler. Pointing Stability Analysis Considering EUCLID Mission. *Airbus Defence and Space*, 2010.
- [37] Woyczyński, W. A. *A First Course in Statistic for Signal Analysis*. 1th edition, 2009.
- [38] XMM-Newton Community Support Team. *XMM-Newton Users Handbook*. ESA Publications Division, 2015.